UNCLASSIFIED

SECURITY CLASSIFICATION OF THIS PAGE (When Data Entered)

REPORT DOCUMENTATION PAGE

READ INSTRUCTIONS BEFORE COMPLETING FORM

1. REPORT NUMBER: AFIT/CI/NR 88-87
2. GOVT ACCESSION NO.
3. RECIPIENT'S CATALOG NUMBER

4. TITLE (and Subtitle): MODELING AND PERFORMANCE OF HF/OTH RADAR TARGET IDENTIFICATION SYSTEMS
5. TYPE OF REPORT & PERIOD COVERED: MS THESIS
6. PERFORMING ORG. REPORT NUMBER

7. AUTHOR(s): DONALD J. STRAUSBERGER
8. CONTRACT OR GRANT NUMBER(s)

9. PERFORMING ORGANIZATION NAME AND ADDRESS: AFIT STUDENT AT: OHIO STATE UNIVERSITY
10. PROGRAM ELEMENT, PROJECT, TASK AREA & WORK UNIT NUMBERS

11. CONTROLLING OFFICE NAME AND ADDRESS
12. REPORT DATE: 1988
13. NUMBER OF PAGES: 143

14. MONITORING AGENCY NAME & ADDRESS (if different from Controlling Office): AFIT/NR, Wright-Patterson AFB OH 45433-6583
15. SECURITY CLASS. (of this report): UNCLASSIFIED
15a. DECLASSIFICATION/DOWNGRADING SCHEDULE

16. DISTRIBUTION STATEMENT (of this Report): DISTRIBUTED UNLIMITED: APPROVED FOR PUBLIC RELEASE

17. DISTRIBUTION STATEMENT (of the abstract entered in Block 20, if different from Report): SAME AS REPORT

18. SUPPLEMENTARY NOTES: Approved for Public Release: IAW AFR 190-1
LYNN E. WOLAVER
Dean for Research and Professional Development
Air Force Institute of Technology
Wright-Patterson AFB OH 45433-6583
19 July 88
GO BLUE

19. KEY WORDS (Continue on reverse side if necessary and identify by block number)

20. ABSTRACT (Continue on reverse side if necessary and identify by block number): ATTACHED

88

DD FORM 1 JAN 73 1473 EDITION OF 1 NOV 65 IS OBSOLETE

UNCLASSIFIED

SECURITY CLASSIFICATION OF THIS PAGE (When Data Entered)

CHAPTER I

INTRODUCTION

Several Radar Target Identification (RTI) techniques have been developed at The Ohio State University in recent years. Using the ElectroScience Laboratory compact range a large data base of coherent RCS measurement has been constructed for several types of targets (aircraft, ships, and ground vehicles) at a variety of polarizations, aspect angles, and frequency bands. This extensive data base has been used to analyze the performance of several different classification algorithms through the use of computer simulations.

In order to optimize classification performance, Ksienski [1] concluded the radar frequency range should lie in the Rayleigh–resonance frequency range, where the wavelength is on the order of or larger than the target size. For aircraft and ships with general dimensions on the order of 10 meters to 100 meters it is apparent that the High Frequency (HF) band provides optimal classification performance. Since existing HF radars are currently being used for detection and tracking of aircraft and ships of these dimensions, it is natural to further investigate the possibility of using these existing radars as the measurement devices in a radar target classification system.

A general radar target classification system is shown in Figure 1. The external environment consists of a target which is to be classified, clutter source(s), noise source(s), and possible calibration reference(s). The environment is observed by

the multifrequency radar through the propagation media. The signal processor provides radar data which, when combined with *a priori* knowledge of the external environment and knowledge of the radar system and propagation media, allows the estimation of target features to be used for classification. These estimated features of the unknown target are compared with high accuracy features of several targets in a catalog set. The classification algorithm provides a measure of the *similarity* of the unknown target to each catalog target. The catalog target whose features most closely represent that of the unknown targets' features is chosen as the type of the unknown target.

This study investigated various propagation conditions which allow different target features to be estimated. These conditions were synthesized by various channel models. The incorporation of these channel models into a radar target identification system computer simulation provided estimates of resulting classification performance. As a result, the relationship between channel conditions and classification performance were found.

HF radars are generally catagorized by the propagation mode by which they are designed to operate, either 1) surface wave or 2) skywave. Each propagation mode incites different characteristics into the classification system, and therefore should be investigated independently.

Because of their unique propagation mechanism, surface wave radars have the ability to look beyond the horizon with detection ranges up to 300 km. Surface wave attenuation is a function of many parameters, most importantly ground conduction and frequency [6]. In order to achieve practical detection ranges for given transmitted power levels the radar wave usually must propagate over water. Furthermore only a vertically polarized wave propagates significantly, thus limiting

MODELING AND PERFORMANCE OF HF/OTH RADAR TARGET IDENTIFICATION SYSTEMS

A Thesis

Presented in Partial Fulfillment of the Requirements for

the Degree Master of Science in the

Graduate School of the Ohio State University

by

Donald J. Strausberger, B.S.E.E.

* * * * *

The Ohio State University

1987

Master's Examination Committee:

Professor Fred D. Garber

Professor Randy L. Moses

Approved by:

F.D. Garber

Adviser
Department of Electrical
Engineering

ACKNOWLEDGEMENTS

I wish to thank Professor Fred D. Garber for his assistance. In addition, I thank Dr. Eric K. Walton for his guidance throughout this project. Finally, I express my gratitude to Professor Randy L. Moses for his review of this thesis.

VITA

[redacted] ..... [redacted]

1982 ..... A.A.S., Southern Illinois University, Carbondale, Illinois

1982-1983 ..... Electronic Technician, Fyrnetics Inc., Elgin, Illinois

1986 ..... B.S.E.E., Southern Illinois University, Carbondale, Illinois

1986-1987 ..... Graduate Research Associate,
The Ohio State University
ElectroScience Laboratory,
Columbus, Ohio

FIELDS OF STUDY

Major Field: Electrical Engineering

TABLE OF CONTENTS

LIST OF FIGURES

LIST OF TABLES

CHAPTER I

INTRODUCTION

Several Radar Target Identification (RTI) techniques have been developed at The Ohio State University in recent years. Using the ElectroScience Laboratory compact range a large data base of coherent RCS measurement has been constructed for several types of targets (aircraft, ships, and ground vehicles) at a variety of polarizations, aspect angles, and frequency bands. This extensive data base has been used to analyze the performance of several different classification algorithms through the use of computer simulations.

In order to optimize classification performance, Ksienski [1] concluded the radar frequency range should lie in the Rayleigh–resonance frequency range, where the wavelength is on the order of or larger than the target size. For aircraft and ships with general dimensions on the order of 10 meters to 100 meters it is apparent that the High Frequency (HF) band provides optimal classification performance. Since existing HF radars are currently being used for detection and tracking of aircraft and ships of these dimensions, it is natural to further investigate the possibility of using these existing radars as the measurement devices in a radar target classification system.

A general radar target classification system is shown in Figure 1. The external environment consists of a target which is to be classified, clutter source(s), noise source(s), and possible calibration reference(s). The environment is observed by

the multifrequency radar through the propagation media. The signal processor provides radar data which, when combined with *a priori* knowledge of the external environment and knowledge of the radar system and propagation media, allows the estimation of target features to be used for classification. These estimated features of the unknown target are compared with high accuracy features of several targets in a catalog set. The classification algorithm provides a measure of the *similarity* of the unknown target to each catalog target. The catalog target whose features most closely represent that of the unknown targets' features is chosen as the type of the unknown target.

This study investigated various propagation conditions which allow different target features to be estimated. These conditions were synthesized by various channel models. The incorporation of these channel models into a radar target identification system computer simulation provided estimates of resulting classification performance. As a result, the relationship between channel conditions and classification performance were found.

HF radars are generally catagorized by the propagation mode by which they are designed to operate, either 1) surface wave or 2) skywave. Each propagation mode incites different characteristics into the classification system, and therefore should be investigated independently.

Because of their unique propagation mechanism, surface wave radars have the ability to look beyond the horizon with detection ranges up to 300 km. Surface wave attenuation is a function of many parameters, most importantly ground conduction and frequency [6]. In order to achieve practical detection ranges for given transmitted power levels the radar wave usually must propagate over water. Furthermore only a vertically polarized wave propagates significantly, thus limiting

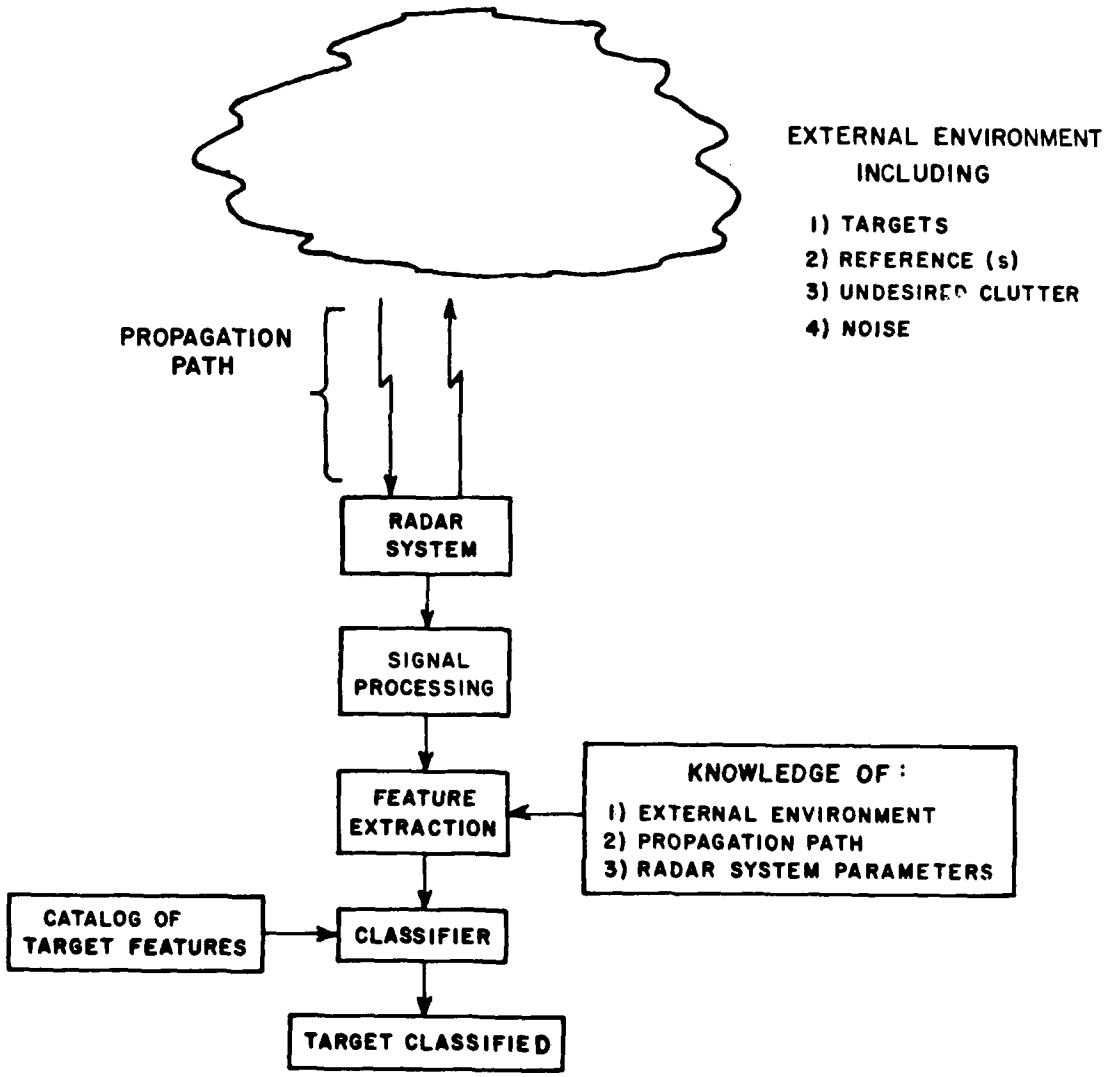

Figure 1: General classification system.

the polarization diversity of our measurement system.

HF skywave radar utilizes ionospheric reflection as the propagation mechanism. The skywave radar has an average detection range of 1000 km to 4000 km, which when coupled with an antenna steerable in azimuth up to 120°, provides coverage of over 15 million square kilometers [12]. The ionosphere supports HF radio propagation at altitudes of 100 to 500 km and consists of ionized regions referred to as layers which are commonly labeled D, E, F_1, and F_2. Ions at these altitudes are mainly produced by solar radiation which includes particle radiation, ultraviolet light, and x-rays. In general, it is the electron density distribution at a given altitude which effects the propagation of the EM wave to the greatest extent.

The actual ion distribution at any time is a function of many factors including source radiation intensity, angle between zenith and solar radiation rays, ion distributions, and various ion combination mechanisms as described in Davies [14]. Therefore the ionosphere is continually changing and must be monitored in real-time to accurately determine its present structure. It is the variation in electron density with altitude which causes variation in the refractive index and results in the bending of the ray path and its return to earth. It is important to note the ionosphere only supports propagation over a limited band of frequencies, and signals of different frequencies may travel along different ray paths.

The earth's magnetic field also affects the propagation of the radar wave. The magnetic field and ionosphere produce a magnetoionic medium which supports propagation modes with specific polarizations. These polarizations are a function of the magnetic field, parameters of the ionosphere, and the direction of propagation as given in Davies [14]. As a result, a transmitted wave of a given polarization may split into two ray paths which may or may not travel the same route to the target. Therefore, in general, the polarization of the transmitted wave is not

necessarily the polarization of the wave which illuminates the target, and the polarization of the field scattered from the target is not necessarily the polarization of the return wave at the receive antenna. Researchers such as Pilon and Headrick [24] have addressed this situation as it applies to the RCS estimation problem. This phenomena must be carefully investigated when selecting the polarization of the catalog sets.

CHAPTER II

HF RADAR SIGNAL PROCESSING

2.1 DOPPLER PROCESSING

Many operation HF radars are used for the detection and tracking of targets on or over ocean waters. A typical radar cell illuminated by a surface wave radar is shown in Figure 2. The width of the observation cell is determined by the antenna beamwidth at the radar operating frequency, while the length is determined by the time gating of the received signal. To observe a cell at a distance R_1, from the antenna with a cell length ΔR, the received signal is gated in time with values:

$$\tau_1 = \frac{2R_1}{c} \tag{2.1}$$

$$\tau_2 = \tau_1 + \frac{2\Delta R}{c} \tag{2.2}$$

where c is the speed of light, and $(\tau_2 - \tau_1)$ is the time gate used. With a multi-frequency radar, the beamwidth of the antenna may change since the radiation pattern is a function of frequency. Therefore the size of the cell varies with changes of the radar's operating frequency.

In operation, the radar transmits a continuum of modulated pulses at some given pulse repitition frequency (PRF). A total of N pulses are transmitted during the coherent integration time T_C, where:

$$N = PRF \cdot T_C \tag{2.3}$$

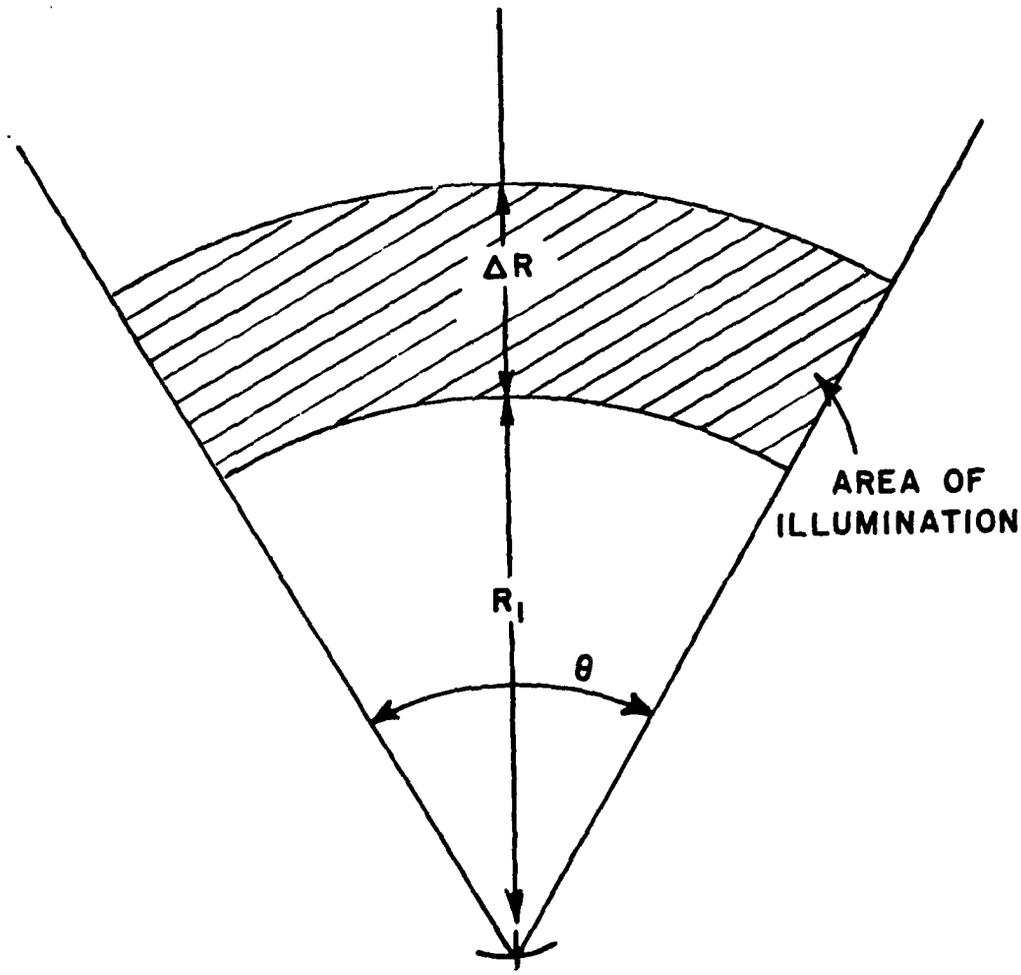

Figure 2: Surface wave radar cell illumination.

Therefore N coherent data records are produced from the energy scattered from the radar cell. These data are Doppler processed to produce a power spectral density estimate containing N data, with a frequency resolution $\frac{1}{T_C}$ and a bandwidth from $-\frac{PRF}{2}$ to $+\frac{PRF}{2}$. Theoretically, greater resolution may be obtained by increasing of the coherent integration time; however changes in the ionospheric ray path, sea state, and target place a limit on the practical integration time [22]. The resulting spectra shown in Figure 3 exhibits 1) a return from the target $\tilde{P}_T(f)$ with induced doppler shift f_T, 2) two large clutter returns $\tilde{P}_{+B}(f)$ and $\tilde{P}_{-B}(f)$ at $+f_B$ and $-f_B$ respectively, and 3) other relatively low power clutter covering the spectrum.

2.2 DOPPLER SPECTRAL ESTIMATE INFORMATION CONTENT

Information contained in the spectral estimate may be used to estimate a number of target features for classification purposes. Using f_T, the relative velocity of the target may easily be estimated, giving the RTI designer knowledge of the probable class of the target (ships, general aircraft, high speed aircraft, etc.). In addition, estimates of the power returned from the target $\tilde{P}_T(f)$ and the power returned from some reference $\tilde{P}_R(f)$ may be used to estimate RCS related target features.

The two large power densities at $+f_B$ and $-f_B$ result from electromagnetic wave scattering from ocean wave sets of a certain wavelength. The ocean waves which excite this Bragg scattering mechanism have a wavelength dependent upon the radar frequency [15]. As explained in detail by Trisna [15], Barrick [5], and others, the amplitude of the Bragg returns are largely dependent upon sea state.

Large variations in the estimates $\tilde{P}_{+B}(f)$ and $\tilde{P}_{-B}(f)$ about some means $\langle P_{+B}(f) \rangle$ and $\langle P_{-B}(f) \rangle$ may be observed over a given observation period as noted

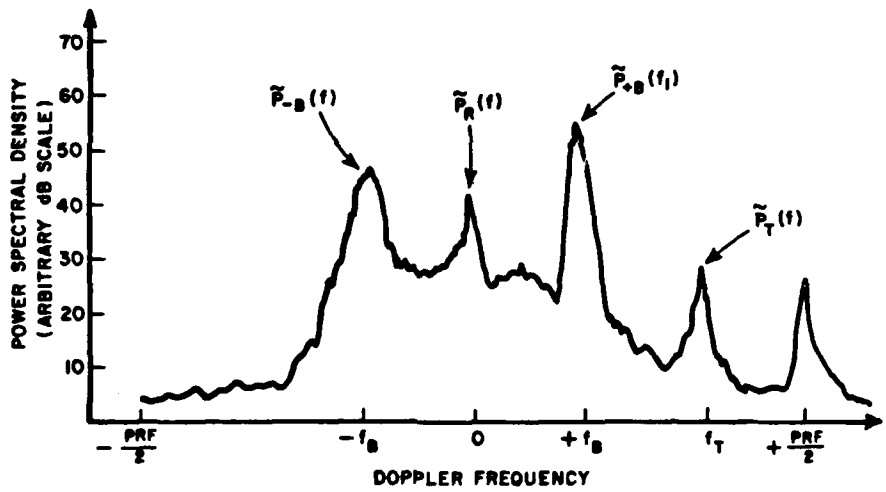

Figure 3: Doppler power spectral density estimate.

by Headrick and Pilon [24]. Therefore the Bragg returns may best be described as a random process with its mean being a function of the sea state at that time. An understanding of this process is important if the Bragg lines are to be used as a reference in the target feature estimation process.

2.3 STATISTICS OF SPECTRAL COMPONENTS

As discussed, the height of a target return or Bragg line in a given doppler spectra is only an estimate of the power returned from the respective scatter. Consider creating $(M-1)$ additional doppler PSD estimates of the same cell to give a total of M doppler PSD estimates. Furthermore, create these additional estimates by observing the cell over a continuous time span t_{OBS}, where

$$t_{OBS} = t_{EST} \times M \tag{2.4}$$

as shown in Figure 4. Examples of real data obtained in this manner may be found in Pilon and Headrick [24].

Note in Figure 4 that each spectra gives a different estimate for each Bragg peak as well as the target spectral peak. However, by averaging M samples taken over M consecutive CIT periods (k = 1,...M) one may produce an averaged doppler PSD as shown in Figure 4. The averaged estimated power returned from the target, approaching Bragg wave set, and receding Bragg wave set are given by Eq. (2.5), Eq. (2.6), and Eq. (2.7) respectively.

$$\tilde{P}_T^M(f_1) = \frac{1}{M}\sum_{k=1}^{M} {}^k\tilde{P}_T(f_1) \tag{2.5}$$

$$\tilde{P}_{+B}(f_1) = \frac{1}{M}\sum_{k=1}^{M} {}^k\tilde{P}_{+B}(f_1) \tag{2.6}$$

$$\tilde{P}_{-B}(f_1) = \frac{1}{M}\sum_{k=1}^{M} {}^k\tilde{P}_{-B}(f_1) \tag{2.7}$$

If each of the samples on the right hand side of Eq. (2.5) are independent and identically distributed, the application of the central limit theorem as discussed in Degroot [10] gives:

$$\lim_{M\to\infty}\left[\frac{1}{M}\sum_{k=1}^{M}{}^{k}\tilde{P}_T(f_1)\right] = \lim_{M\to\infty}\tilde{P}_T^M(f_1) = \langle P_T(f_1)\rangle \tag{2.8}$$

where $\langle P_T(f_1)\rangle$ is the expected value of the returned power from the target as discussed earlier. Likewise, application on the central limit theorem to Eq. (2.6) and Eq. (2.7) yields Eq. (2.9) and Eq. (2.10) respectively.

$$\lim_{M\to\infty}\left[\frac{1}{M}\sum_{k=1}^{M}{}^{k}P_{+B}(f_1)\right] = \lim_{M\to\infty}\tilde{P}_{+B}^M(f_1) = \langle P_{+B}(f_1)\rangle \tag{2.9}$$

$$\lim_{M\to\infty}\left[\frac{1}{M}\sum_{k=1}^{M}{}^{k}P_{-B}(f_1)\right] = \lim_{M\to\infty}\tilde{P}_{-B}^M(f_1) = \langle P_{-B}(f_1)\rangle \tag{2.10}$$

Although this implies an infinite observation time which is impractical, it also implies that we can continually improve the accuracy of our estimates by taking more samples.

Both the CIT and the observation time must be carefully chosen in order to satisfy the requirement of independence and identically distributed samples. The observation time must be selected to assure the identical distribution of samples. A significant change in target flight path during the observation time may cause the observed RCS to change and therefore $\langle P_T(f_1)\rangle$ changes voiding the identically distributed criteria. Likewise a change in sea state during the observation time may alter $\langle P_{+B}(f_1)\rangle$ and $\langle P_{-B}(f_1)\rangle$ with the same result. In general, however, sea states may remain unchanged for hours [15]. In addition, significant changes in the observation path (such as passage of ionospheric disturbance for skywave radars) limits the observation time. In fact, fluctuations in the ionosphere generally impose the greatest restriction on the maximum observation time.

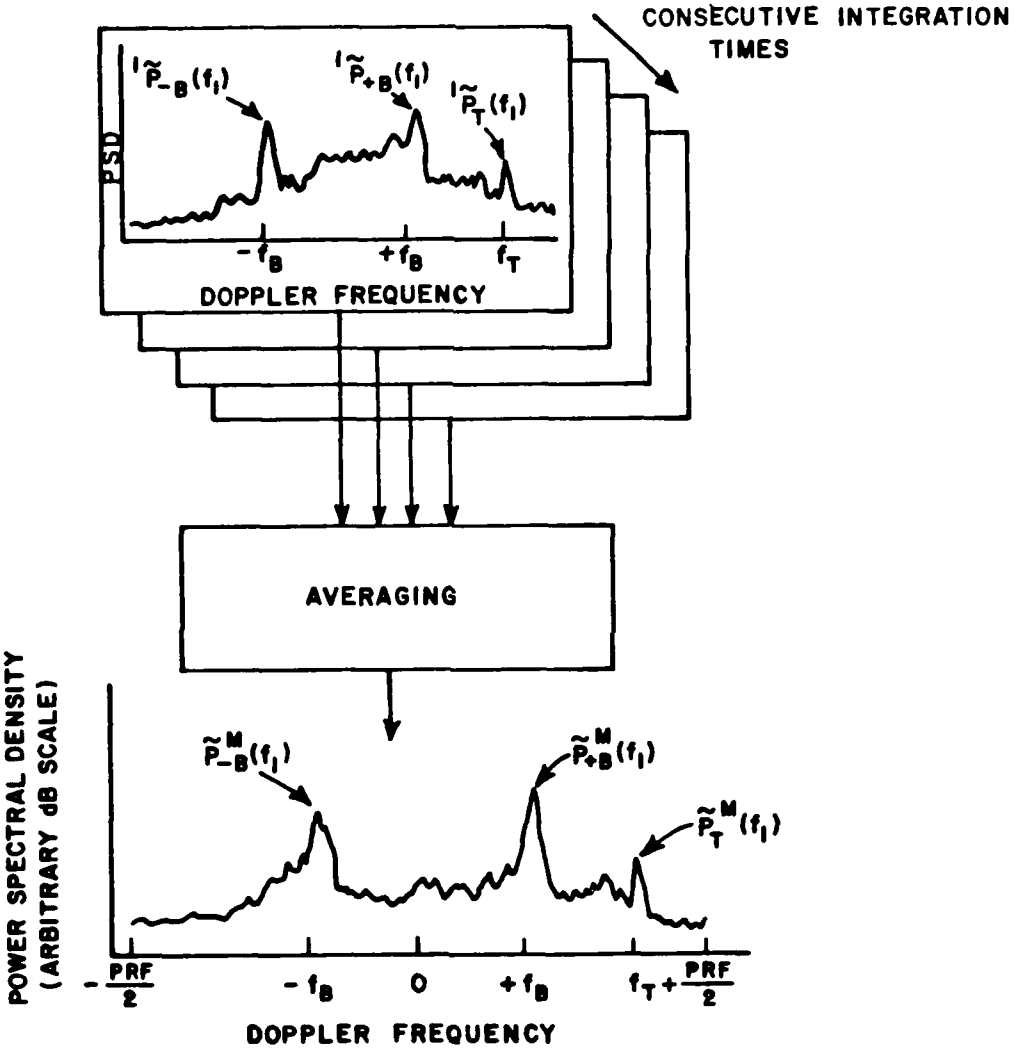

Figure 4: Averaging of independent spectral estimates.

There is a limit to the shortest possible integration time that produces independent samples of the Bragg spectral lines. An experimental study by Barrick [13] concluded that an integration time of 25 seconds or greater insures independence of spectra, irregardless of sea state and cell size, at frequencies in the HF band above 7 MHz.

The remaining question is, given a CIT of 25 seconds, what is the relationship between the standard deviation values of $\tilde{P}_T^M(f_1)$, and $\tilde{P}_{+B}^M(f_1)$, $\tilde{P}_{-B}^M(f_1)$, and M? As discussed by Barrick [13], without assuming Gaussian statistics, there is little to do other that record massive amounts of data and extract empirical results. Using a Gaussian assumptions Barrick derived:

$$\sigma_{\tilde{P}_B^M(f)} = \frac{\langle P_B^M(f) \rangle}{\sqrt{M}} \tag{2.11}$$

where $\sigma_{\tilde{P}_B^M(f)}$ s the standard deviation of the random variables given in Eq. (2.6) and Eq. (2.7). Figure 5, from Barrick [13], shows the 90% confidence interval lines derived using the same statistical assumption. These curves give the RTI designer insight into the tradeoffs between the observation time and the accuracy of the estimates $\tilde{P}_{+B}^M(f_1)$ and $\tilde{P}_{-B}^M(f_1)$. This is important if $\tilde{P}_{+B}^M(f_1)$ or $\tilde{P}_{-B}^M(f_1)$ are to be used in the estimation of target features for classification.

2.4 FREQUENCY SELECTIVE FADING

The Doppler spectral estimate resulting from data accumulated via skywave propagation is distored to varying degrees by the ionospheric path. The distortion, referred to as ionospheric contamination, is a function of parameters that may or may not be under the control of the radar operator. It is imparitive, if data from the resulting spectra are used in an estimation and classification procedure, that

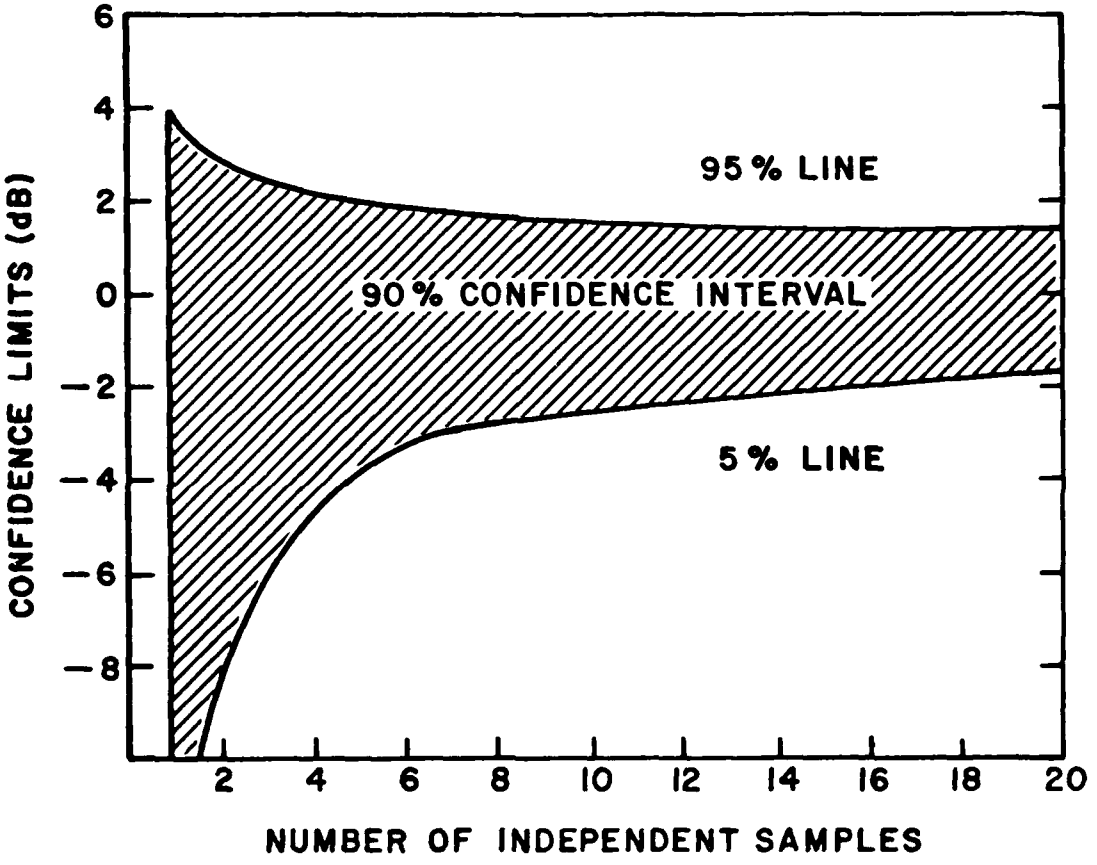

Figure 5: Relationship between deviation of average Bragg line amplitude and number of independent samples used for averaging.

the distortion be removed or at least understood so it may be compensated for in the process.

Consider a target being illuminated by a single wave which travels along a single ionospheric path. The ionosphere, which is in constant motion, induces a Doppler shift on the rate and direction of the ionospheric movement. Now consider illuminating this target N times by waves which propagate by the same layer whose relative velocity remained unchanged during the time the data was accumulated (the CIT). The resulting spectra will be offset in doppler frequency by:

$$f_{offset} = \frac{2v_I^1}{\lambda_R} + \frac{2v_I^2}{\lambda_R} \tag{2.12}$$

where v_I^i is the relative ionospheric velocity with respect to direction of radar wave propagation during the pass and λ_R is the radar wavelength. This phenomena, referred to as Doppler shifting, is easily detected in the skewing of the spectra as shown in Figure 6, and can be easily compensated for.

Next, consider the case where the CIT is relatively long such that the relative velocity of the propagating layer has undergone considerable change. Each passing wave may have a slightly different doppler component induced by the quickly changing ionosphere. The resulting contamination of the spectra, known as broadening, is shown in Figure 7.

Spectral broadening is highly undesired for several reasons. First, any reduction in the amplitude of the target return will make the return more succeptable to other noise, thus making any target feature estimated from the data less reliable. Second, the return from the target may not be significantly greater than the higher order sea return and noise surrounding it, and thus the target may be easily lost in the clutter surrounding it. Third, if the target has a Doppler frequency which is

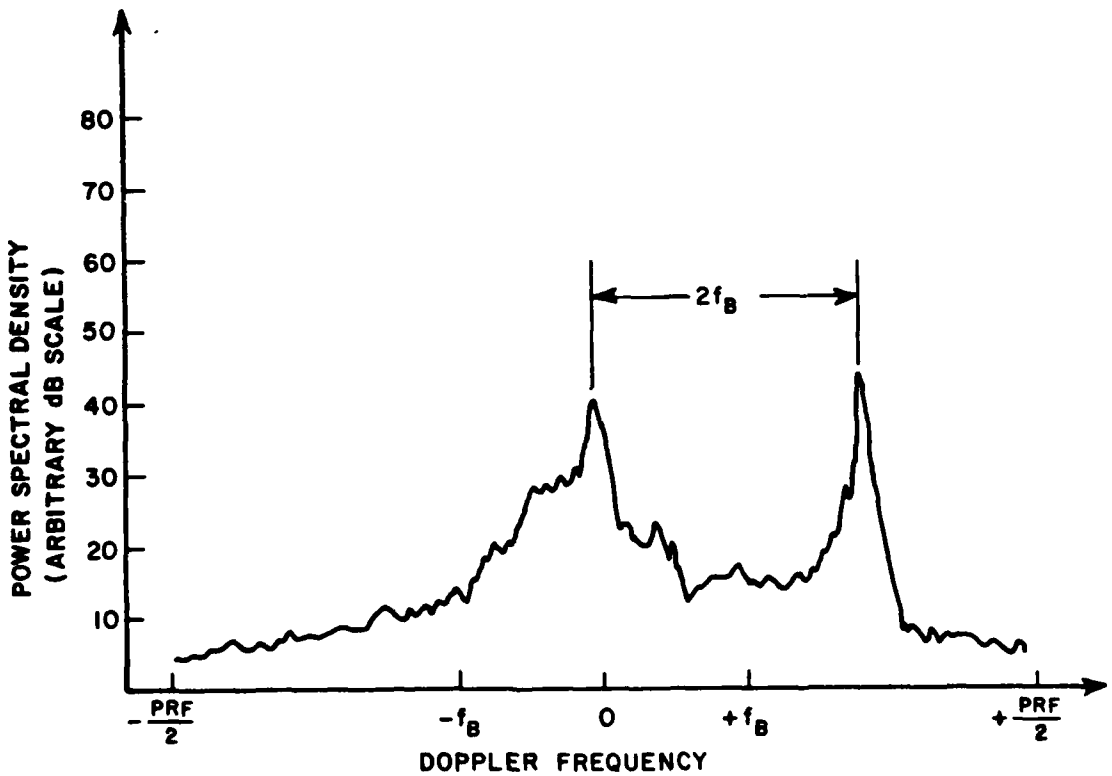

Figure 6: Shifted Doppler spectra.

near a Bragg frequency, the resultant spreading of the Bragg line may essentially *cover* the target.

An additional cause of Doppler spreading is multipath propagation [22]. The path or paths the wave takes between the transmit antenna and the target is a function of many radar parameters including frequency, launch angle, and polarization, as well as real-time ionospheric conditions. Different ionoshperic layers may support propagation of waves of the same frequency. This may result in two or more waves with different induced doppler shifts both containing information about the target being processed together, with a resulting spectra which exhibits spreading.

A third cause of ionospheric distortion results from horizontal spacial inhomogenity within a given layer [22]. A ray path utilizes an area of a given layer proportional in size to the beamwidth of the antenna. The larger the beamwidth, the larger the area used for refraction, and the greater the effect of the spreading as investigated by George and Marseca [22]. Since beamwidth scales inversely with frequency, we recognize that the effect of spacial inhomogenity will decrease at higher frequencies for propagation via a given layer. The RTI system designer is interested in an antenna with a minimal beamwidth; however physical size poses a design restriction. For example, a beamwidth of 1° may require antenna dimensions on the order of 2 km [12].

In order to use doppler spectral data in an estimation process, one first desires a measure of the degree of the spectral contamination. In general, the width of the Bragg lines gives a reasonable measure of ionospheric contamination [22]. A great deal of research has gone into this area as well as the development of processes designed to *clean up* the distorted spectra [22].

An alternate approach is to minimize distortion by judicious selection of radar

parameters. The selection of an observation time will result in a trade-off between resolution and broadening. Since spectral peaks are largely uncorrelated after 25 seconds (see Section 2.3) we desire the shortest CIT above 25 seconds that meets the minimum spectral resolution demands of the system. This allows the greatest number of independent spectra to be amassed in the least total observation time. Coherent integration times ranging from 25 seconds to 100 seconds are common. The amount of disturbance a given ionospheric region is undergoing determines the degree of spreading for a given CIT. Typically, the E and E_S regions are considered most stable but do not always exist. During sunrise and sunset, the ionospheric regions undergo rapid change and the degree of broadening significantly increases.

The judicious choice of radar operating frequencies can also greatly reduce the effect of ionospheric contamination. There are however, important trade-offs between the number of frequencies over which one may obtain data and the quality of that data. The RTI system designer desires estimates of features at a number of frequencies. Through the use of vertical incidence ionograms and sweep of frequency backscatter echoes one can determine the frequency bands least likely to result in multipath distortion [25].

One possible method the RTI system designer may choose is to use an existing measure of spectral contamination with a limit, throwing away all spectra contaminated beyond that limit, and making his estimates and classification decision based only on the remaining data. This method is introduced by Georges in [22]. A second approach is to create feature estimates using all possible spectra and then weight the features in the classificaton process according to the degree of distortion of the data from which the features were taken. A third approach is to estimate features from the doppler spectra whose values are not effected by

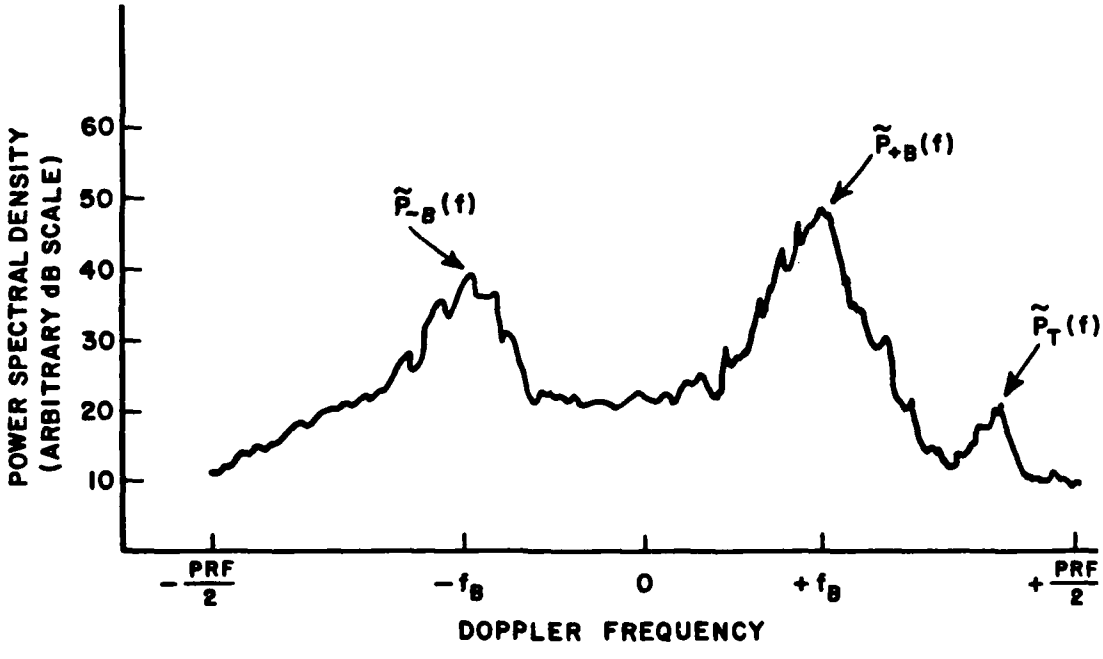

Figure 7: Example of Doppler spreading.

the spreading. All major peaks in the spectra are equally effected by spreading such that the ratios $\frac{\langle P_T(f)\rangle}{\langle P_{+B}(f)\rangle}$, $\frac{\langle P_T(f)\rangle}{\langle P_{-B}(f)\rangle}$, and $\frac{\langle P_{+B}(f)\rangle}{\langle P_{-B}(f)\rangle}$ all remain unchanged [23] Therefore use of these ratio in feature estimation may provide estimates which are relatively unaffected by Doppler spreading.

CHAPTER III

MULTI-FREQUENCY PARAMETER ESTIMATION

3.1 GENERAL CONSIDERATIONS

All RTI algorithms utilize estimates of various features of the unknown target to classify the target. Features such as radar cross section, intrinsic target phase, and target speed may be considered good target descriptors. However, there is a trade–off between the number of features used in a system, the cost of the system (processing time, etc.), and the resulting classification performance. As a result, research has been directed at finding the optimal types and numbers of features which result in optimal performance at minimal cost given little or no constraints in our ability to obtain estimates of these features [2], [4] and [8]. In an operational HF radar classification system the numbers and types of estimated features may be severely limited due to the constraints imposed by the HF channel.

The purpose of this section is to study the constraints the HF radar system imposes on the classification system. Given these constraints, we can then investigate which and how many of the features available should be used to obtain optimal performance. Previous research has led to the development of RTI algorithms which incorporate multi-frequency measurements of RCS and intrinsic phase in various forms as classification features. The number and selection of frequencies to be used has been studied with regard to resulting classification performance [2]. Different classification algorithms may place additional restrictions on frequency

selection. However, in an operational HF RTI system, the bandwidth is likely to be constrained by propagation parameters, thereby constraining the number and type of features estimated. The different propagation modes of surface wave and sky wave radars result in different types of bandwidth restraints on the two systems, therefore they are investigated independently.

3.2 FREQUENCY BAND CONSIDERATIONS

The frequency range of a surface wave radar is not limited by the ability of the system to propagate a wave over a large range, but rather by the propagation loss which increases with frequency [6]. A target which exists at some range from the radar site may be illuminated over a frequency range of 5 MHz to 30 MHz; however the propagation loss at the upper frequencies may result in the backscatter energy from the target being on the order of the higher-order sea clutter return or galactic noise level therefore making detection and any estimation of target features impossible. In fact, the lower signal to noise ratio at higher frequencies may result in poorer quality estimates of features even though detection is still possible.

Interference with other users in the HF band may also preclude the use of some frequencies. During testing of an experimental system in Florida, interference in the 8–13 MHz band was a significant factor in system operation [7]. In addition, backscatter resulting from undesired E – region sky wave propagation periodically effected sytem performance at lower frequencies [7]. Therefore there are definite limits to the frequency band over which estimates of features may be obtained.

Thus once system specifications have been set (type of targets, minimum range, etc.) the frequency range for a surface wave radar may be determined. Bands of 6 Mhz to 8 Mhz may expected to be used [7]. From here the RTI

system designer must determine which features to estimate, at which frequencies to make the estimates, and how many total estimates are needed in order to achieve maximum classification performance.

The frequency band over which an HF sky wave radar can illuminate a target is dependent on the current ionospheric conditions. Therefore real-time assessment of the ionosphere is important in order to determine the band. Assessment of the frequency band may be made through the use of backscatter sounding. A backscatter sounding consists of radiating a frequency–modulated continous–wave signal which is swept in frequency, then receiving the backscatter from the earth after it has made two passes through the ionosphere [25]. An oblique backscatter sounding is then produced by plotting the return power level as intensity versus time and frequency. An example is given in Figure 8.

A target appears as a near horizontal line on the resulting plot, as shown in Figure 8. A direct measurement of the frequency band over which the target is illuminated may then be made. Typical values range on the order of 1 MHz to 8 MHz.

It must be noted that real-time monitoring of the ionospheric path in order to determine the largest frequency band(s) over which a target may be observed are not commonplace. Other uses of sky wave radars such as ocean waveheight and wind direction maps do incorporate real-time ionospheric measurements to aid in selection of frequency bands which are most immune to multipath distortion [21], [23], and [25].

Considerable research has been and is being conducted in the area of real-time ionospheric monitoring. It is apparent that these monitoring systems can be of great aid to an RTI system utilizing the HF sky wave radar as its measurement device.

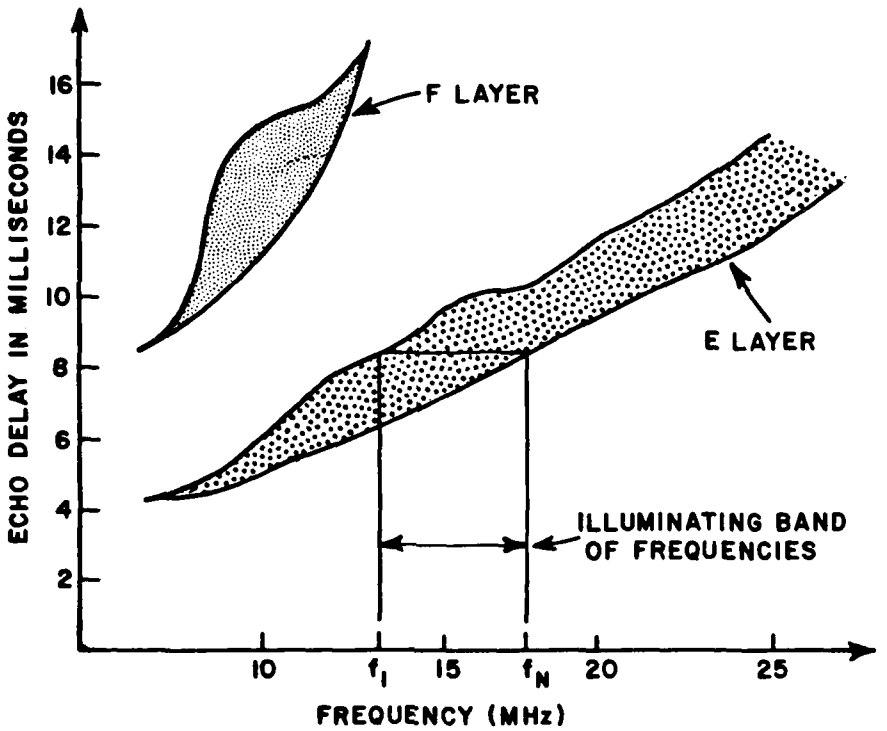

Figure 8: Oblique backscatter sounding.

3.3 ABSOLUTE RCS ESTIMATION

The absolute radar cross-section of a target at frequency f may be estimated by:

$$\tilde{\sigma}(f) = P_T(f) \left[\frac{P_{AV} G_{TX} G_{RX} \lambda^2 F_P^2 t_{CIT}}{(4\pi)^3 R^4 L_S} \right]^{-1} \tag{3.1}$$

where R is the one way path length the wave travels to the target, P_{AV} is the average transmitted power, G_{TX} is the transmitting antenna gain, G_{RX} is the receiving antenna gain, λ is the wavelength, F_P is the one way propagation loss factor, t_{CIT} is the coherent processing time, $P_T(f)$ is the received power from target, and L_S is a factor accounting for system losses. Therefore, to directly estimate the absolute RCS of a target at N frequencies, the above parameters must be estimated at each frequency used. System parameters such as P_{AV}, G_{TX}, G_{RX}, t_{CIT}, f and L_S are generally known or may be accurately estimated at each frequency. The power returned from the target $P_T(f)$ at each frequency may be estimated from the appropriate Doppler spectra as discussed earlier. However, the range (R) and propagation loss (F_P) may be much more difficult to estimate depending on the propagation mode involved.

For a surface wave radar, the range to the target may easily be estimated through time gating or other signal processing strategies. The propagation loss, however, is a function of the sea state over the path as well as frequency and thus becomes more difficult to accurately estimate; see Norton [6]. A sky wave radar poses a problem when attempting to estimate the path length R. The first difficulty results from path length being a function of the ionospheric structure which is constantly changing with time. In addition, waves of different frequencies

may travel differenct paths to illuminate the same target thus making R not only a function of time but also of frequency [14].

To circumvent the difficulties of estimating F_P in a surface wave radar and R in a skywave radar, a reference may be employed. Possible references include land masses, ocean markers, or Bragg lines. Knowledge of the radar cross section of the reference then allows estimation of the target RCS at each frequency. A method of calibrating Bragg lines for use as an absolute reference is given in Trisna [15].

3.4 RELATIVE RCS ESTIMATION

Bragg lines may also be employed as a relative reference. Figure 9 shows two spectra obtained at two frequencies f_1 and f_2. Knowing the expected change in the mean of the Bragg line amplitude with frequency (which is assumed to be zero in this example) the relative RCS estimates of the target can be constructed as shown in Eq. (3.2) and Eq. (3.3).

$$\sigma_T^*(f_1) = (20 - 30)dB = -10dB \tag{3.2}$$

$$\sigma_T^*(f_2) = (15 - 30)dB = -20dB \tag{3.3}$$

Therefore, the RCS of the target at f_1 is 1/10th the RCS of the reference, and the RCS of the target at f_2 is 1/100th the RCS of the reference. Thus the relative change of the target RCS has been estimated without absolute calibration of the Bragg line. Therefore, the use of the relative RCS of the target as a possible feature for classification purposes should be evaluated.

3.5 RELATIVE PHASE ESTIMATION

Previous RTI studies have shown that intrinsic target phase often proves to be a powerful feature when used for classification [2], [8]. However, difficulties in

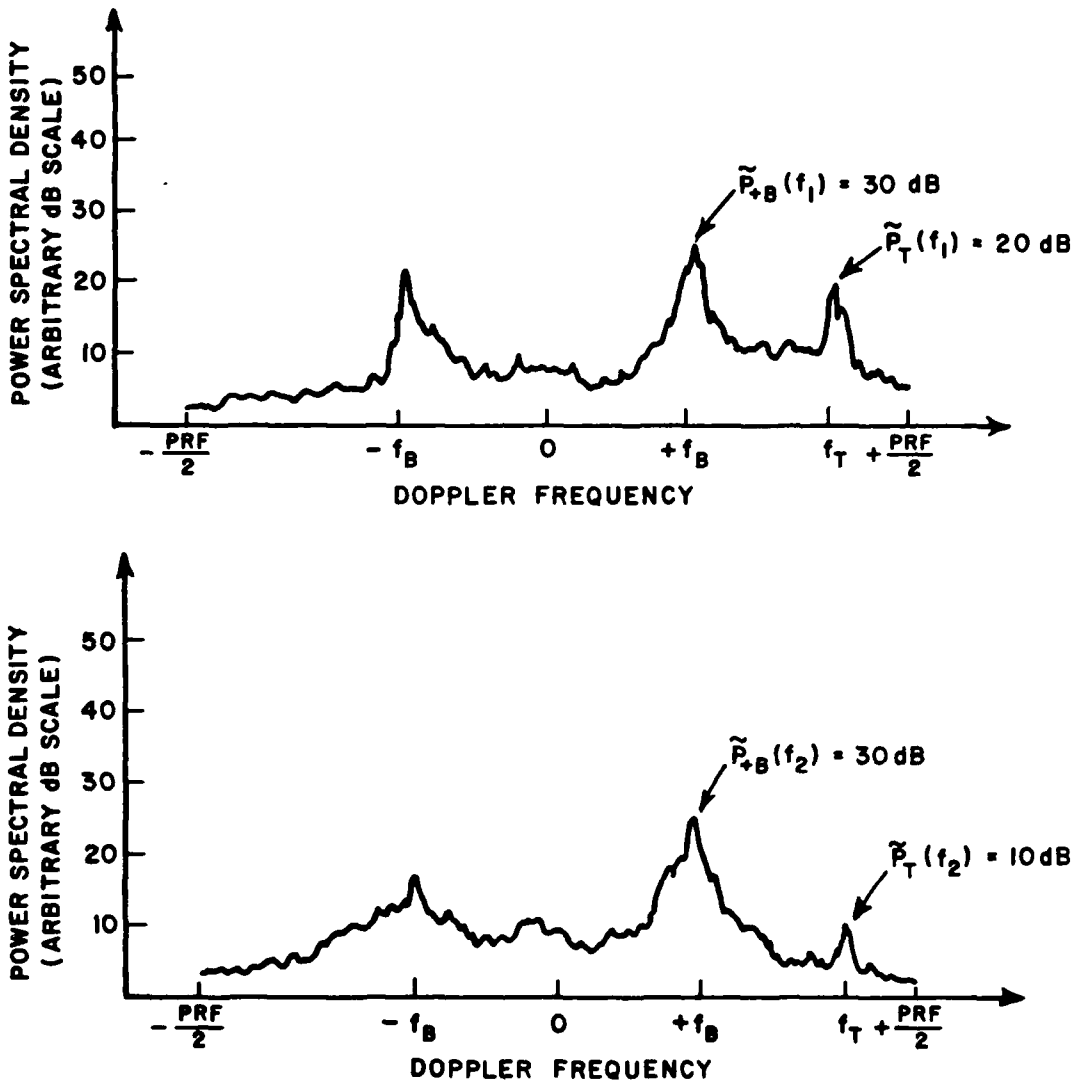

Figure 9: Spectra for relative RCS estimation.

accurately estimating the path length to the target as in the case of the sky wave propagation may preclude the accurate estimation of intrinsic target phase. Therefore an alternate method of utilizing target phase information has been studied.

Consider the phases of two radar signals at frequency f_1 and f_2, which are returned from the same target as given by Eq. (3.4) and Eq. (3.5).

$$\oslash_{f_1} = \frac{2\pi(R_{f_1})}{\lambda_1} + \theta_{f_1} \tag{3.4}$$

$$\oslash_{f_2} = \frac{2\pi(R_{f_2})}{\lambda_2} + \theta_{f_2} \tag{3.5}$$

where R_{f_1} is the round trip path length of wave at frequency f_1, R_{f_2} is the round trip path length of wave at frequency f_2, $\lambda_1 = \frac{c}{f_1}$, $\lambda_2 = \frac{c}{f_2}$, and θ_{f_1} and θ_{f_2} are the intrinsic target phases at f_1 and f_2 respectively.

By multiplying Eq. (3.4) and Eq. (3.5) by λ_1 and λ_2 respectively and then subtracting Eq. (3.4) from Eq. (3.5), we are left with:

$$\lambda_{f_2} \oslash_{f_2} - \lambda_{f_1} \oslash_{f_1} = 2\pi(R_{f_2} - R_{f_1}) + \lambda_{f_2}\theta_{f_2} - \lambda_{f_1}\theta_{f_1} \tag{3.6}$$

where $(R_{f_2} - R_{f_1})$ is the difference between round trip path lengths at f_2 and f_1 respectively. Through careful selecton of $\Delta f = f_2 - f_1$ and using ionograms to estimate the present structure of the ionosphere, it may be possible to accurately estimate $(R_{f_2} - R_{f_1})$. By multiplying this estimate by 2π radians, and then subtracting this result from Eq. (3.6), we are left with Eq. (3.7).

$$\Pi = \lambda_{f_2}\theta_{f_2} - \lambda_{f_1}\theta_{f_1} \tag{3.7}$$

Further division by λ_{f_2} gives Eq. (3.8), which for $f_2 \cong f_1$ (Δf small) may be approximated by Eq. (3.9).

$$W = \theta_{f_2} - \left(\frac{\lambda_{f_1}}{\lambda_{f_2}}\right)\theta_{f_1} \tag{3.8}$$

$$W \cong \theta_{f_2} - \theta_{f_1} \tag{3.9}$$

Therefore W is a feature dependent on the change of the characteristic phase of the target associated with f_2 and f_1.

Figure 10 demonstrates a physical interpretation of the W function for a simple scattering case. Consider two targets, each with single distinct scattering points at f_1 and f_2 as shown. Each target has an intrinsic phase at each frequency related to the distance from some reference to the scattering point on the target as given in Eq. (3.10), Eq. (3.11), Eq. (3.12) and Eq. (3.13).

$$\theta_{f_1}^{T_1} = \frac{2\pi\left(2D_{f_1}^{T_1}\right)}{\lambda_{f_1}} \tag{3.10}$$

$$\theta_{f_2}^{T_1} = \frac{2\pi\left(2D_{f_2}^{T_1}\right)}{\lambda_{f_2}} \tag{3.11}$$

$$\theta_{f_1}^{T_2} = \frac{2\pi\left(2D_{f_1}^{T_2}\right)}{\lambda_{f_1}} \tag{3.12}$$

$$\theta_{f_2}^{T_2} = \frac{2\pi\left(2D_{f_2}^{T_2}\right)}{\lambda_{f_2}} \tag{3.13}$$

The resulting W function for each target is given by Eq. (3.14) and Eq. (3.15).

$$W_{f_2-f_1}^{T_1} = \frac{2}{\lambda_{f_2}}\left[2\pi\left(D_{f_2}^{T_1} - D_{f_1}^{T_1}\right)\right] \tag{3.14}$$

$$W_{f_2-f_1}^{T_2} = \frac{2}{\lambda_{f_1}}\left[2\pi\left(D_{f_2}^{T_2} - D_{f_1}^{T_2}\right)\right] \tag{3.15}$$

Note the W function is a measure of the distance between the scattering for the two frequencies, and not the absolute position of the scattering point at any one frequency.

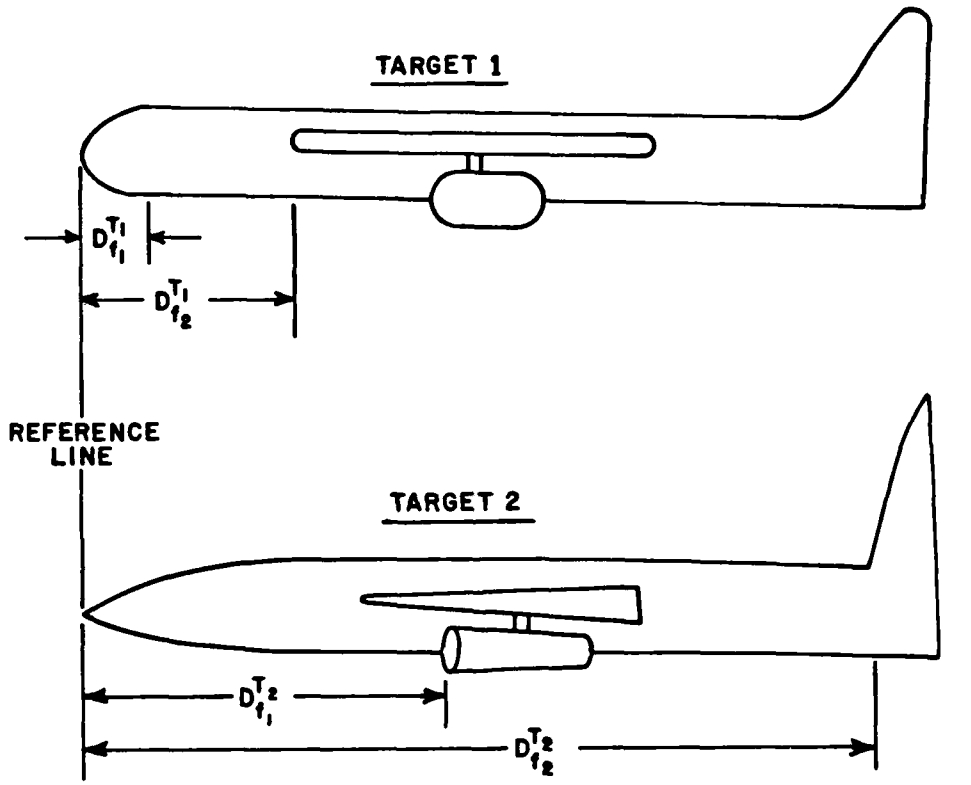

Figure 10: Targets with two simple scattering points.

A multi-frequency radar system illuminating a target with M total adjacent frequencies could generate $(M-1)$ W function estimates. These estimates could then be employed as additional features to help identify the target. In general, the larger the Δf, the more the paths taken by the two waves differ, and the harder it is to accurately estimate $(R_{f_2} - R_{f_1})$. However, large Δf values would tend to excite scattering points on the aircraft which are more separated in distance, possibly leading to W functions which contain more information about the individual targets. Therefore, our ability to accurately estimate the change in path lengths with frequency for a given ionospheric condition may determine our maximum Δf.

CHAPTER IV

RADAR SYSTEM SIMULATION AND EVALUATION STUDY

4.1 INTRODUCTION

In order to study the performance of possible radar target classification systems which utilize HF radars as a measurement device, a simulated system has been developed. Over the past several years the ElectroScience Laboratory has developed a large multi–frequency data base consisting of aircraft, ship, and ground vehicle radar signitures. This data base has been used to investigate several RTI methods for the various classes of targets. A data base consisting of calibrated monostatic radar returns of 5 aircraft was chosen for the experimental portion of this study. Although classification of the ships and ground vehicles is of considerable interest, the large amount of previous work with the aircraft data base [2] provides a strong foundation of previous work for comparing results.

The ElectroScience Laboratory compact radar range facility was used to create the data base. A basic block diagram of the measurement system and a picture of the actual facility is given in Figures 11 and 12 respectively. A more detailed explanation of system may be found in [3]. In general, the measurement facility simulates the illumination of a target by a radar wave which is approximately plane in the region of the target (locally plane). This would be true of any HF radar system. The complex backscattered fields from the target and other undesired

scatters are then measured over a frequency band of 1–12 GHz. To obtain the high-accuracy range-independent complex signiture of the target, a calibration sequence described in detail in Kimball [17] was employed. Further detailes concerning data scaling, windowing, and other signal processing details are given in Harris [26], and Kimball [17]. Five metallic scale models of the Concorde, DC10, 707, 727, and 747 were used as targets. Silhouettes and dimensions of the real aircraft are given in Figures 13 through 17. Specifications of the 5 aircraft data base are given in Table 1.

4.2 RADAR SYSTEM SIMULATION

A flowchart of the Radar System Simulation and Evaluation (RSSE) program is shown in Figure 18. The program begins with selection of N complex radar signatures of the 5 targets at frequencies $f_1, f_2, \ldots, f_N$, where the frequencies are chosen by the operator to represent those which may be encountered in a typical HF radar system. In addition, one azimuth angle and one polarization is selected, thus assuming these parameters have been accurately estimated. The target data base is then accessed, the data are appropriately scaled [8], and two sets of data denoted the test and catalog set are created. Each element of the two sets may be represented by:

$$A_k(f_i)e^{j\theta_k(f_i)} = R_k(f_i) + jX_k(f_i) \tag{4.1}$$

where

$$R_k(f_i) = A_k(f_i)\cos(\theta_k(f_i)), \tag{4.2}$$

$$X_k(f_i) = A_k(f_i)\sin(\theta_k(f_i)). \tag{4.3}$$

and

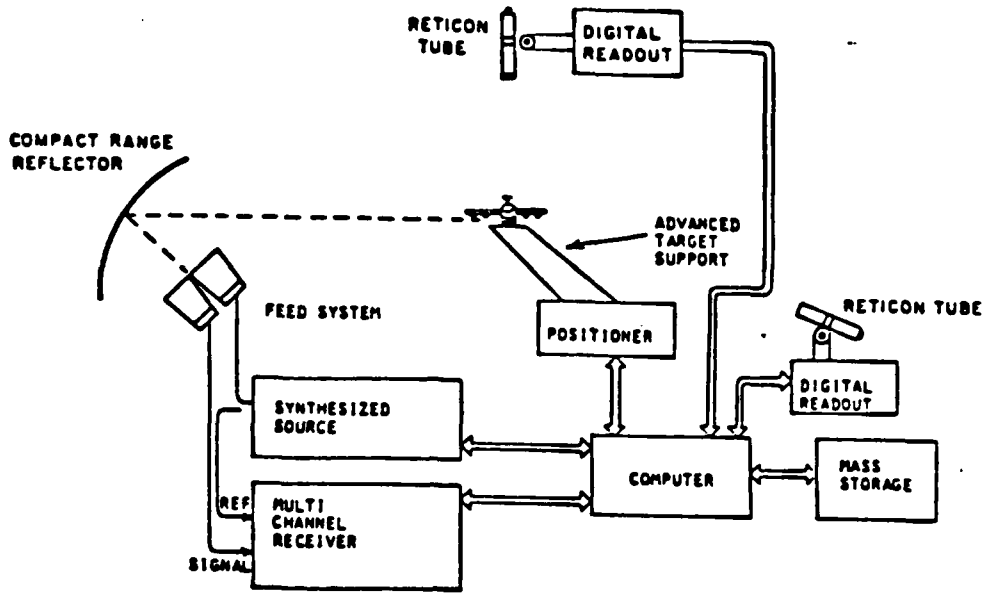

Figure 11: Compact range block diagram, (from Kamis [2]).

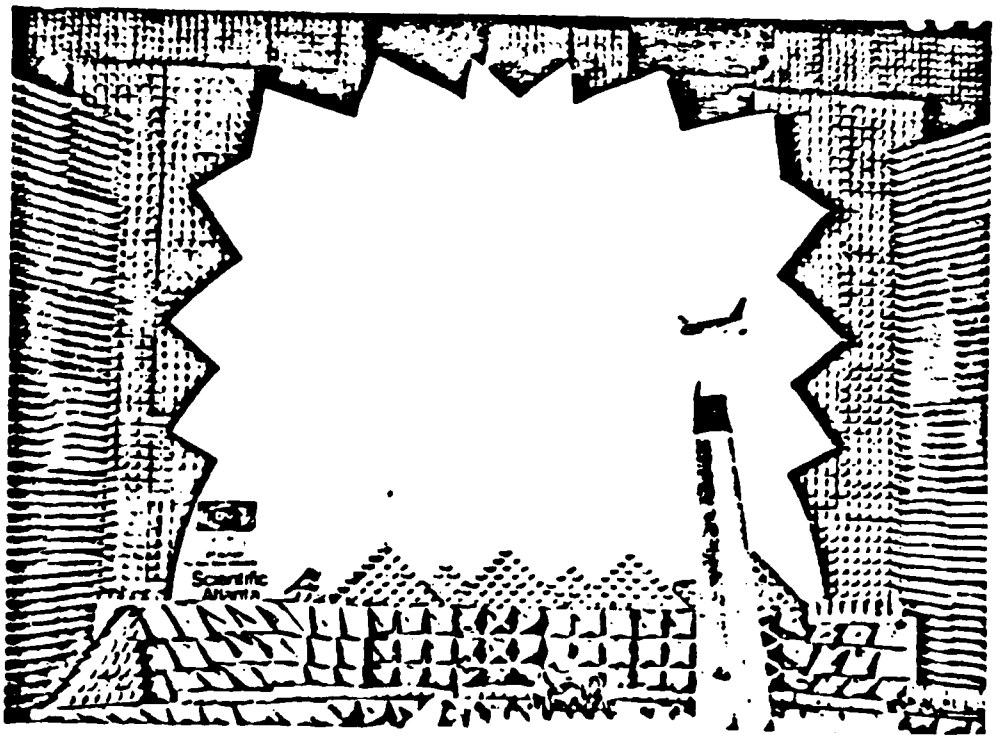

Figure 12: OSU ESL compact range, (from Kamis [2]).

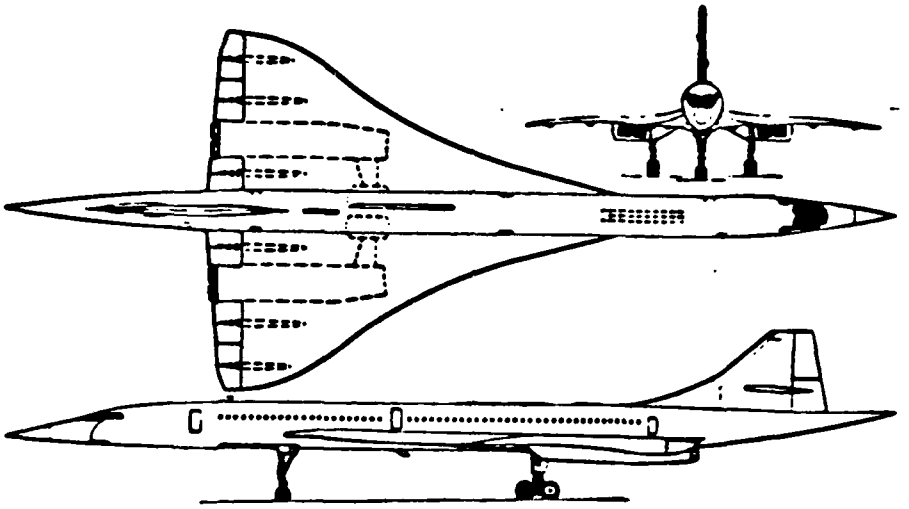

External Dimensions:

Length overall	202 ft	3.6 in	(61.66m)
Height overall	40 ft	0.0 in	(12.19m)
Wing span	83 ft	10.0 in	(25.56m)

Figure 13: Concorde silhouette (from Kamis [2]).

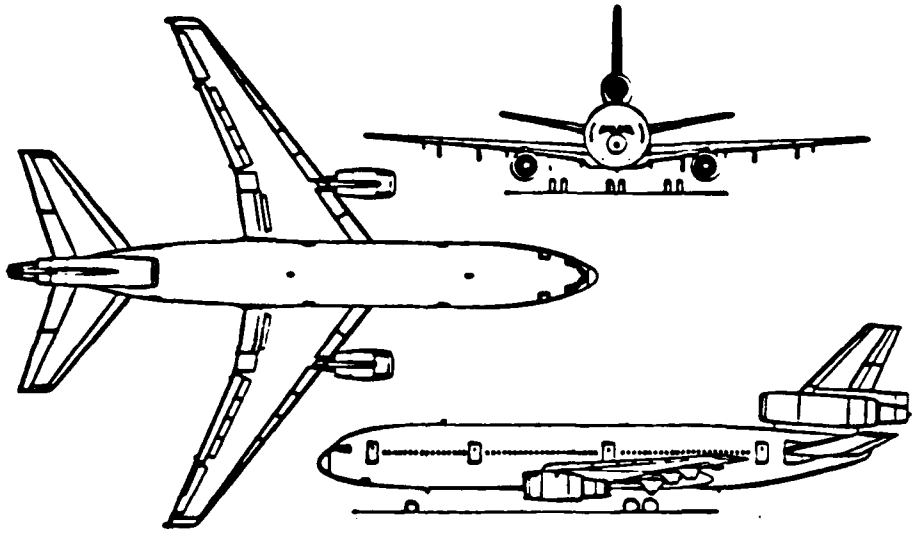

External Dimensions:

Length overall	181 ft	7.2 in	(55.35m)
Height overall	57 ft	7.0 in	(17.55m)
Wing span	165 ft	4.0 in	(50.39m)

Figure 14: DC10 silhouette (from Kamis [2]).

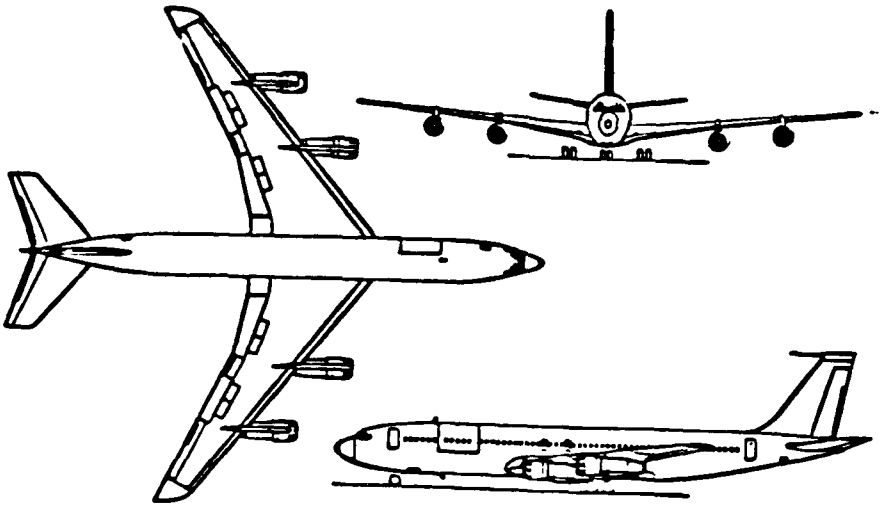

External Dimensions:

Length overall	152 ft 11.0 in (46.61m)
Height overall	42 ft 5.0 in (12.93m)
Wing span	145 ft 9.0 in (44.42m)

Figure 15: 707 silhouette (from Kamis [2]).

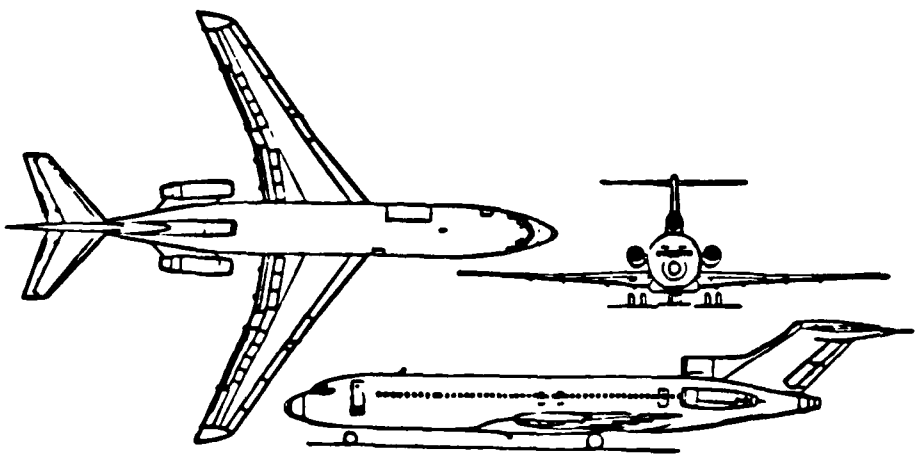

External Dimensions:

Length overall	153 ft 2.0 in (46.69m)
Height overall	34 ft 0.0 in (10.36m)
Wing span	108 ft 0.0 in (32.92m)

Figure 16: 727 silhouette (from Kamis [2]).

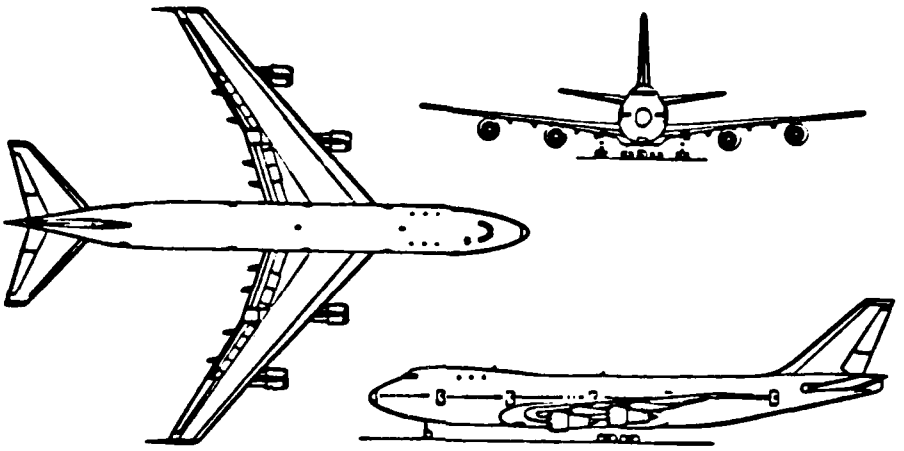

External Dimensions:

Length overall	231 ft	4.0 in (70.51m)
Height overall	63 ft	5.0 in (19.33m)
Wing span	195 ft	8.0 in (59.64m)

Figure 17: 747 silhouette (from Kamis [2]).

Table 1: Data base specifications (from Kamis [2]).

Low-Frequency Data Base

Frequency formatted data strings from 1 to 12 GHz

Availible polarizations:

Transmit Horizontal, Receive Horizontal (HH)

Transmit Vertical, Receive Vertical (VV)

Transmit Horizontal, Receive Vertical (VH)

Availible Azimuth angles @ Elevation = 0°:

0° to 180° by 10° and 15° increments

Common aircraft bandwidth:

7.6 - 60 MHz "Scaled"

Maximum number of usable frequencies: 209

$A_k(f_i)$ = square root of the radar cross section of target at frequency f_i,

A corrupted feature vector representing an unknown target was constructed by first generating $2N$ total noise samples taken from an independent Gaussian zero-mean random process with noise power P_N given by :

$$P_N = 10\log_{10}(\frac{\sigma^2}{2})dBsm \tag{4.4}$$

where σ is the standard deviation of the process in meters [3]. The noise samples were then added to the N high accuracy complex radar signitures of a known target in the test set to create N corrupted complex data of the form:

$$\tilde{R}_u(f_i) = R_T(f_i) + N(f_i) \tag{4.5}$$

$$\tilde{X}_u(f_i) = X_T(f_i) + N'(f_i) \tag{4.6}$$

where $R_T(f_i)$ is defined in Eq. (4.2) for target T in the test set, $X_T(f_i)$ is defined in Eq. (4.3) for target T in the test set, and $N(f_i)$, $N'(f_i)$ are samples from the independent zero-mean gaussian noise process.

The resulting N complex corrupted data which may be represented by :

$$\tilde{R}_u(f_i) + j\tilde{X}_u(f_i) = \tilde{A}(f_i)e^{j\tilde{\theta}_u(f_i)}, \qquad i = 1, ..., N \tag{4.7}$$

constitute the unknown target feature vector. This corrupted feature vector is then tested against the feature vectors of the targets in the catalog set by means of a classifier function as shown. A Euclidian distance metric algorithm commonly refferred to as a Nearest Neighbor (NN) algorithm was employed as the classifier function. The NN algorithm computes a distance ($d_{u,k}$) as a measure of the distance between the unknown target u and the catalog target k, as shown in Eq. (4.8).

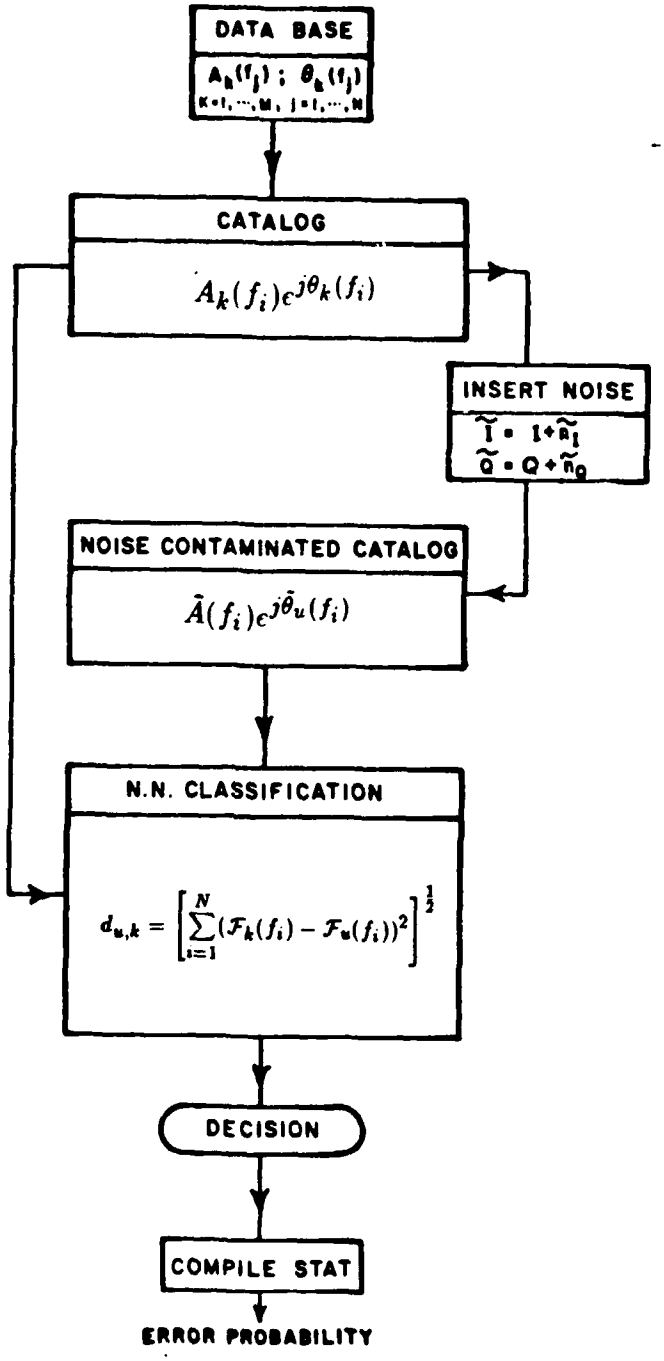

Figure 18: RSSE program flowchart (from Kamis [2]).

$$d_{u,k} = \left[\sum_{i=1}^{N} (\mathcal{F}_k(f_i) - \mathcal{F}_u(f_i))^2 \right]^{\frac{1}{2}} \tag{4.8}$$

where $\mathcal{F}_k(f_i)$ is the feature of target k at frequency f_i; extracted from the catalog set, and $\mathcal{F}_u(f_i)$ is the feature of unknown target u at frequency f_i extracted from the corrupted feature vector.

After testing against the appropriate features of all 5 possible catalog targets ($k = 1$ to 5) the unknown target is classified as the catalog target which produced the smallest distance measure. Whether the classification attempt was succesful or not is known since the identity of the unknown target is known a–priori. This simulation process is repeated 100 times for each test target, with independent noise being added each time to create the simulated feature vector. Results of a run for a given noise power are plotted as a confusion matrix as shown in Figure 19.

The average misclassification percentage has a margin of error since it is the *result of a finite, and not an infinite, number of independent experiments.* Details of the error margin may be found in Degroot [10]. In general, the error margin is on the order of 2 to 3 percent for 5 targets and 100 experiments [2].

4.3 CHANNEL SELECTION AND SIMULATION

In general, the ability to accurately estimate target features such as absolute RCS and intrinsic phase may be described by defining channels with various characteristics which affect the complex backscattered coefficients of the targets. This section describes four channels with different characteristics which allow different target features to be estimated. By appropriately processing the complex backscattered components from the test set for each channel model, and altering the complex backscatter components of the catalog set if appropriate, the

Nearest Neighbor Algorithm - Vector "NON-COHERENT" distance metric

Classification Table for Noise power = 10.00 DBSM

TT#\CT#	1	2	3	4	5	% MIS-CLASS
1	84	1	5	10	0	16.00
2	4	86	3	7	0	14.00
3	0	0	100	0	0	0.00
4	13	9	5	73	0	27.00
5	0	0	0	0	100	0.00

Average mis-classification percentage : 11.40 %

Mis-classification percentage is based on the test targets name.

Figure 19: Confusion matrix (from Kamis [2]).

resulting classification performance given the constraints of each channel may be synthesized.

4.3.1 Coherent Gaussian Channel Model Simulation

A channel which adds coherent independent zero mean Gaussian noise to the complex backscatter coefficients of target T is shown in Figure 20. Note that both the amplitude and phase of the high-accuracy backscatter terms have been corrupted. The resulting estimates $\tilde{R}_u(f_i)$ and $\tilde{X}_u(f_i)$ represent the corrupted real imaginary parts of the complex backscatter coefficients of an unknown target to be classified.

The implementation of the *Channel 1* model into the RSSE program has previously been described in Section 4.2. An algorithm denoted the Coherent Nearest Neighbor Algorithm given by:

$$d_{u,k} = \left[\sum_{i=1}^{N}(R_k(f_i) - \tilde{R}_u(f_i))^2 + (X_k(f_i) - \tilde{X}_u(f_i))^2\right]^{\frac{1}{2}} \tag{4.9}$$

where $R_k(f_i)$, $X_k(f_i)$ are the complex backscatter coefficient of catalog target k, and $\tilde{R}_u(f_i)$, $\tilde{X}_u(f_i)$ are the simulated real and imaginary parts of complex backscatter coefficient of unknown target u, is then used to classify the unknown target U as being the catalog target K^* such that d_{u,k^*} is minimized. It is important to note that intrinsic target phase, although not directly estimated at the output of Channel 1, is utilized in the estimation process.

4.3.2 Non-Coherent Gaussian Channel Model Simulation

A channel which corrupts the amplitudes of the complex backscatter coefficients through coherent addition of independent zero-mean Gaussian noise, while removing all intrinsic phase information is shown in Figure 21. This channel models

a radar system where accurate estimation of intrinsic target phase is not feasible. As a result, only estimates of backscatter amplitudes are available for classification.

The implementation of the *Channel 2* model into the RSSE program has previously been described in Section 4.2. An algorithm denoted the Non-Coherent Nearest Neighbor Algorithm given by:

$$d_{u,k} = \left[\sum_{i=1}^{N}(A_k(f_i) - \tilde{A}_u(f_i))^2\right]^{\frac{1}{2}} \tag{4.10}$$

where $A_k(f_i)$ is the high accuracy amplitude of complex backscatter coefficient of catalog target k, and $\tilde{R}_u(f_i)$ is the simulated amplitude of complex backscatter coefficient of unknown target u, is then used to classify the unknown target u as being the catalog target k^* such that d_{u,k^*} is minimized.

4.3.3 Multiplicitive Component Channel Model Simulation

A channel which multiplies the amplitudes of an unknown target's backscatter coefficients by an unknown constant M in addition to adding noise and removing phase information is shown in Figure 22. This channel models a radar system where accurate estimation of absolute RCS is not practical due to the lack of a calibrated reference, but estimation of relative RCS as described in Section 3.4 is feasible.

One possible method of using $\tilde{A}_u^M(f_i)$ data out of *Channel 3* involves the removal of the unknown factor M. To achieve this, the average power of the corrupt vector out of *Channel 3* is calculated by:

$$\bar{P}^M = \frac{1}{N}\sum_{i=1}^{N}\left(\tilde{A}_u^M(f_i)\right)^2 \tag{4.11}$$

$$\bar{P}^M = M^2\frac{1}{N}\sum_{i=1}^{N}(R_T(f_i) + N'(f_i))^2 + (X_T(f_i) + N(f_i))^2 \tag{4.12}$$

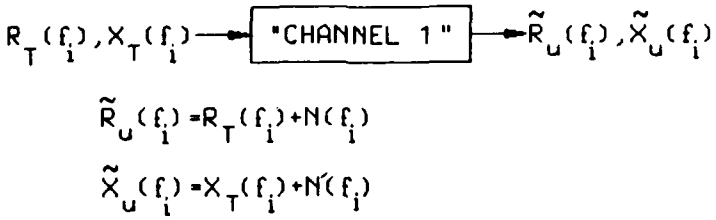

Figure 20: Coherent AWGN channel model.

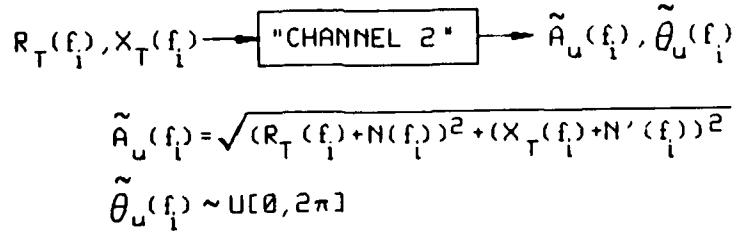

Figure 21: Non-Coherent AWGN channel model.

$$\bar{P}^M = M^2 \bar{P} \tag{4.13}$$

where $\bar{P}$ is the average power of the noise vector if $M = 1$. A new corrupt vector with values given by:

$$\tilde{A}_u^R(f_i) = \frac{\tilde{A}_u^M(f_i)}{\sqrt{\bar{P}^M}} \tag{4.14}$$

$$\tilde{A}_u^R(f_i) = \frac{\sqrt{(R_T(f_i) + N(f_i))^2 + (X_T(f_i) + N'(f_i))^2}}{\sqrt{\bar{P}}} \tag{4.15}$$

may then be constructed. This resulting vector now has values independent of M while maintaining the ratio's of amplitude estimates at different frequencies, i.e.:

$$\frac{\tilde{A}^M(f_i)}{\tilde{A}_u^M(f_j)} = \frac{\tilde{A}_u^R(f_i)}{\tilde{A}_u^R(f_j)} \qquad \text{for } 1 \leq i \leq N, \qquad 1 \leq j \leq N. \tag{4.16}$$

The $\tilde{A}_u^R(f_i)$ features may now be used for target classification with a properly chosen catalog set.

The simulation of utilizing features passed through a channel with an unknown multiplicitive component first required normalization of the catalog set. The power (or average RCS) of catalog target k is given by Eq. (4.17).

$$\bar{P}_k = \frac{1}{N} \sum_{i=1}^{N} (A_k(f_i))^2 \tag{4.17}$$

Dividing each data of catalog target k by the square root of $\bar{P}_k$ gives a new set of data, where the magnitude of each point in the vector is given by Eq. (4.18).

$$A_k^R(f_i) = \frac{A_k(f_i)}{\sqrt{\bar{P}_k}} \qquad i = 1, N \tag{4.18}$$

The new data $A_k^R(f_i)$ represent the relative radar cross section features of catalog target k which will be used in the classification routine. Note that the ratio of radar cross section of any two frequencies f_i and f_j for catalog target k is preserved as shown in Eq. (4.19).

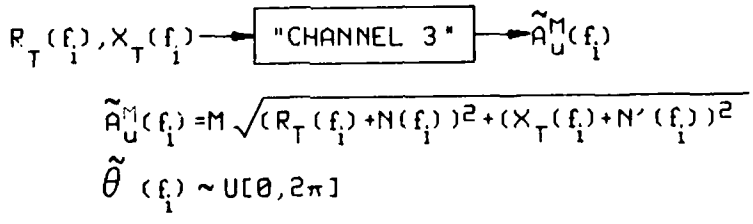

Figure 22: Multiplicitive AWGN channel model.

$$\frac{(A_k(f_i))^2}{(A_k(f_j))^2} = \frac{(A_k^R(f_i))^2}{(A_k^R(f_j))^2} \qquad 1 \leq i \leq N \ , 1 \leq j \leq N \tag{4.19}$$

The normalization described in Eq. (4.17) and Eq. (4.18) is carried out on all catalog targets ($k = 1$ to 5). As a result, each catalog target has an average power (or average RCS) given by:

$$\bar{P}_k^R = \frac{1}{N} \sum_{i=1}^{N} (A_k^R(f_i))^2 \tag{4.20}$$

$$\bar{P}_k^R = \frac{1}{N} \sum_{i=1}^{N} \left(\frac{A_k(f_i)}{\sqrt{\bar{P}_k}} \right)^2 \tag{4.21}$$

$$\bar{P}_k^R = \frac{1}{\bar{P}_k} \frac{1}{N} \sum_{i=1}^{N} (A_k(f_i))^2 \tag{4.22}$$

$$P_k^R = \frac{1}{\bar{P}_k} P_k = 1 \tag{4.23}$$

Therefore, the overall average size of each target in the catalog has been removed.

The normalization is graphically depicted in Figure 23. The complex backscattered amplitudes at frequencies f_1 and f_2 for two catalog targets are depicted by vectors $\bar{V}_1$ and $\bar{V}_2$. Vector $\bar{V}_2$ represents a relatively large target with an average RCS on the order of 1000 sm, and $\bar{V}_1$ represents a smaller target with an average RCS on the order of 400 sm. Note the distance between the two points in space representing the targets is on the order of 10 to 15 meters. After normalization, the two targets are represented by vectors $\hat{V}_1$ and $\hat{V}_2$. Note the distance between the points in space representing the two targets has significantly decreased.

The addition of coherent i.i.d. noise to the complex backscattered components of a test target to form a corrupt test vector was carried out as described earlier. After the noise was added the power of the test vector was calculated by:

$$\bar{\tilde{P}} = \frac{1}{N} \sum_{i=1}^{N} (R_T(f_i) + N(f_i))^2 + \left(X_T(f_i) + N'(f_i) \right)^2 \tag{4.24}$$

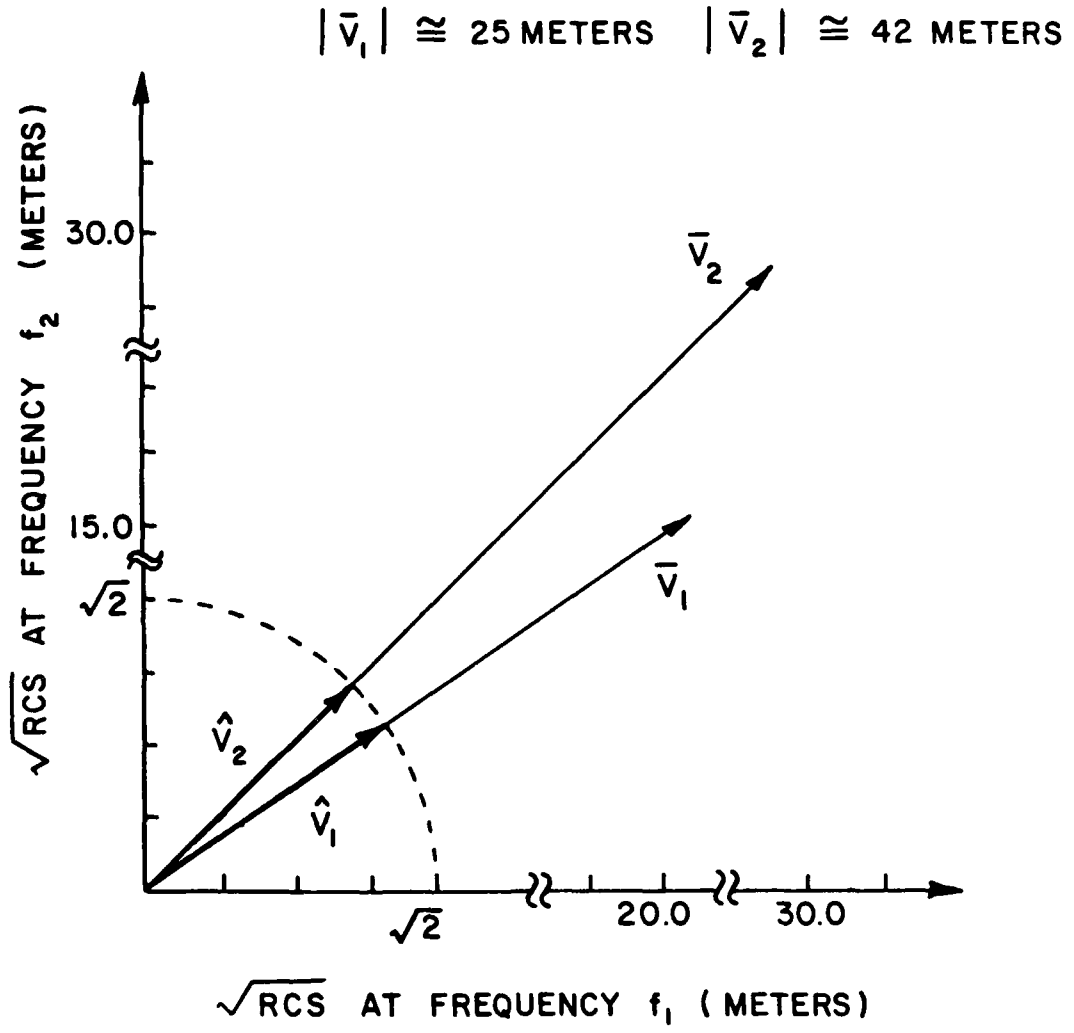

Figure 23: Normalization of data vector.

The amplitudes of the simulated backscatter components were then normalized by:

$$\tilde{A}_u^R(f_i) = \frac{\left[(R_T(f_i) + N(f_i))^2 + (X_T(f_i) + N'(f_i))^2\right]^{\frac{1}{2}}}{\sqrt{\bar{P}}}, \qquad i = 1, ..., N \quad (4.25)$$

producing the normalized amplitudes of the backscatter estimates of the unknown target. This process would remove any unknown multiplicitive component from the test vector as shown earlier. It is critical that the noise be added before the normalization process is completed in order to directly compare the relative RCS to the absolute RCS as possible classification features. If normalization is done before noise is added, the signal to noise ratio will be much lower resulting in significantly poorer classification performance. The unknown target may then be tested against each of the catalog targets by use of a Nearest Neighbor Algorithm of the form:

$$d_{u,k} = \left[\sum_{i=1}^{N} \left(A_k^R - \tilde{A}_u^R(f_i)\right)^2\right]^{\frac{1}{2}} \quad (4.26)$$

where $A_k^R(f_i)$ and $\tilde{A}_u^R(f_i)$ are given in Eq. (4.18) and Eq. (4.25) respectively, and the identity of the unknown target is chosen as the catalog target k^* for which $d_{u,k}$ is minimized.

4.3.4 Additive Component Channel Model Simulation

Since the case of using a channel model with an unknown multiplicitive factor M is of interest, it is natural to extend the problem to the case of an unknown additive component C as shown in Figure 24. The addition of the unknown component C^2 under the radical sign as shown represents the estimation of RCS of a target at 2 or more frequencies, where only the difference in RCS is known. For example, the difference in RCS of a target at f_1 and f_2 may be known to be 500 sm

but whether the RCS at f_1 and f_2 is 10 sm and 510 sm respectively, or 1000 sm and 1500 sm is not known. Although this problem may or may not arise, it is of considerable interest to the RTI designer to determine the achievable classification performance given a channel with this constraint.

To remove the unknown additive component C'^2, the average power of the corrupt vector at the output of *Channel 4* is calculated by:

$$\bar{P}^C = \frac{1}{N}\sum(\tilde{A}_u^C(f_i))^2 \tag{4.27}$$

$$\bar{P}^C = C'^2 + \bar{P} \tag{4.28}$$

where $\bar{P}$ is the average power if $C'^2 = 0$. The vector is then normalized by:

$$\tilde{A}_u^D(f_i) = \sqrt{(\tilde{A}_u^C(f_i))^2 - [P_{norm} + \bar{P}^C]} \tag{4.29}$$

$$\begin{aligned}\tilde{A}_u^D(f_i) &= \Big[(R_T(f_i) + N(f_i))^2 + (X_T(f_i) + N'(f_i))^2 \\ &+ C'^2 - [P_{norm} + (C'^2 - \bar{P})]\Big]^{\frac{1}{2}}\end{aligned} \tag{4.30}$$

$$\tilde{A}_u^D(f_i) = \Big[(R_T(f_i) + N(f_i))^2 + (X_T(f_i) + N'(f_i))^2 + [\bar{P} - P_{norm}]\Big]^{\frac{1}{2}} \tag{4.31}$$

giving a new vector independent of C, while maintaining the difference in power (RCS) between data at any two frequencies.

Features constructed from a channel with an unknown constant additive component are referred to as relative difference RCS (RDRCS) features. The features were implemented into the RSSE program by reconstructing each target in the catalog set so its new average power $\bar{P}_k^{AV}$ is the same for all targets while the difference between RCS at a given frequency and the average RCS is maintained. The same reconstruction of the corrupted test vector removes any unknown additive component from the estimates. As a result, each target in the catalog set is given

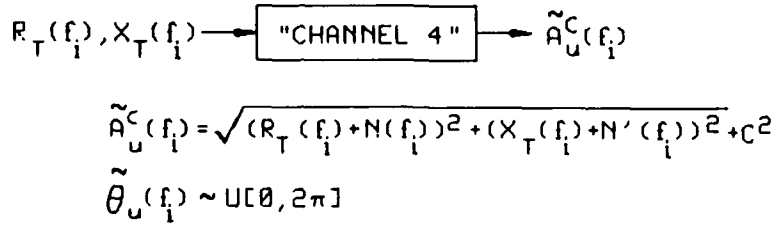

Figure 24: Additive AWGN channel model.

the same average RCS, with the difference between the RCS at each frequency and the average RCS being maintained.

The normalization of the catalog set in the RSSE program was accomplished as described above. Since the amplitude of the complex backscatter coefficients in the catalog set is actually the square root of the radar cross section at each frequency, the amplitudes were reconstructed using:

$$A_k^D(f_i) = \left[(A_k(f_i))^2 + (P_{norm} - \bar{P}_k)\right]^{\frac{1}{2}} \tag{4.32}$$

where

$$\bar{P}_k = \frac{1}{N}\sum_{i=1}^{N}(A_k(f_i))^2. \tag{4.33}$$

An example of the normalization effect on two catalog targets is given in Figure 25. Consider target 1 in the catalog set with RCS values 500sm, 400sm, and 300sm, and target 2 with RCS values of 600sm, 1000sm, and 1400sm at frequencies f_1, f_2 and f_3 as shown. The average RCS over the three frequencies is 400sm and 1000sm for targets 1 and 2 respectively. After the normalization, the average RCS of both targets is 1600sm (P_{norm} = 1600sm) as shown. As a result, absolute target size is lost; however, the difference between the RCS at any frequency and the average RCS is maintained.

Coherent noise was added as always to the complex backscatter coefficients of target T of the test set to create the noisy feature vector. The average power of the noisy feature vector was then calculated as:

$$\bar{P}^u = \frac{1}{N}\sum_{i=1}^{N}(\tilde{A}_u(f_i))^2. \tag{4.34}$$

The amplitudes of the noisy feature vector were then reconstructed as:

$$\tilde{A}_u^D(f_i) = \left[(\tilde{A}_u(f_i))^2 + (P_{norm} - \bar{P}^u)\right]^{\frac{1}{2}} \tag{4.35}$$

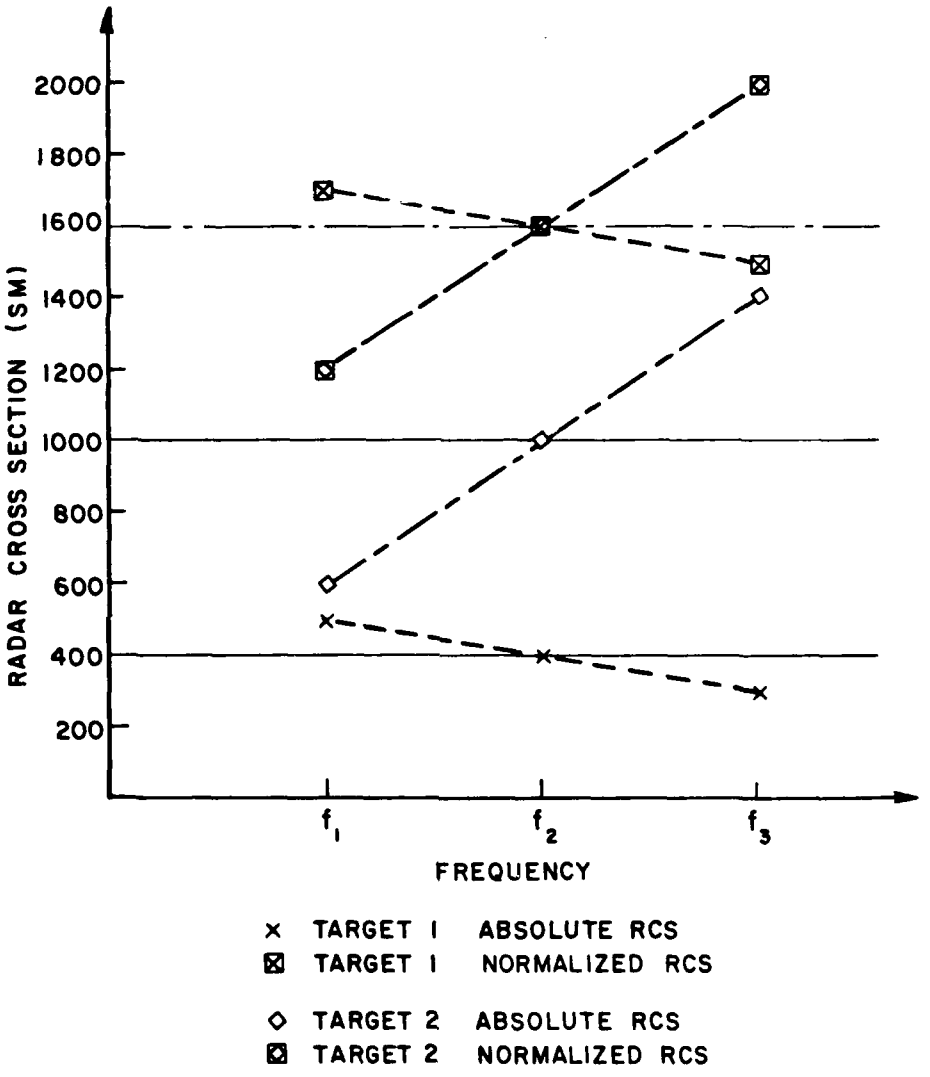

Figure 25: Normalization of two targets.

These data represent the estimates of the amplitudes of the complex coefficients passed through channel 4 after the additive unknown component has been removed.

As a result, the Nearest Neighbor Algorithm given by:

$$d_{u,k} = \left[\sum_{i=1}^{N} (A_k^D(f_i) - \tilde{A}_u^D(f_i))^2 \right]^{\frac{1}{2}} \tag{4.36}$$

where $A_k^D(f_i)$ and $\tilde{A}_u^D(f_i)$ are given by Eq. (4.32) and Eq. (4.35) respectively, was used to classify the unknown target u as the catalog target k^* for the k^* such that d_{u,k^*} is minimized.

It is important to note that although the power of the catalog vectors and corrupted vector is altered, the signal-to-noise ratio of the initial corrupted vector is not changed, and thus classification performance will not be function of the power level chosen for normalization. Simulations were repeated using normalization power levels of 4000 sm, 6000 sm, and 8000 sm to insure this result.

4.4 ASSESSMENT OF MISCLASSIFICATION CURVES

A typical set of misclassification curves is shown in Figure 26. Performance of a given curve with respect to another may be related by the relative noise power immunity. The noise power immunity of a curve is determined by the difference between the noise power of the curve and the reference curve evaluated at a constant misclassification level (generally between 5 and 40 percent). The noise power immunity is an approximate measure of the additional noise power which must corrupt the according data to produce a curve equivalent to the reference. A positive noise power immunity indicates better classification performance with respect to the reference, while negative noise power immunity indicates the opposite.

CHAPTER V

RSSE RESULTS FOR AWGN CHANNELS

5.1 Frequency Band Study

The frequency band over which a target at a given range may be illuminated is limited. As a result, only estimated features from the limited band are available for classification. Thus a study has been conducted to find the effect of frequency band size on classification performance for the four channels described in Sections 4.3.1 through 4.3.4.

Figure 26 shows the change in performance as the frequency band of channel 1 is decreased. Note the overall performance is not significantly effected. Figure 27 demonstrates the greater loss of performance with decreasing frequency band when channel 2 used. A significant loss of noise power immunity of approximatel 8 dB-sm is encountered when the frequency band decreased from 4 MHz to 2 MHz.

Similarly, Figure 28 demonstrates the even greater decrease in classification performance encountered by decreasing the frequency band when channel 3 introduces an unknown multiplicitive component. Losses on the order of 5 and 12 dB-sm noise power for a given misclassification percentage appear as the frequency band is decreased from 8 MHz to 4 MHz, and then 4 MHz to 2 MHz. Figure 29, which was generated utilizing the unknown additive component channel, expresses the most significant decrease in performance as the band is decreased from 8 MHz to 4 MHz.

Figures 26 through 29 demonstrate some qualities unique to each of the four channels. Channel 1 demonstrated a very small change in performance compared with the three other channels as the frequency band was significantly decreased. Both channel 2 and channel 3 showed a much larger degredation in performance when the band was reduced to 2 MHz as compared to the reduction to 4 MHz. This implies a frequency band of not less than 4 MHz would be highly desirable given a channel which does not allow the estimation of phase information. This also implies that a doubling of the frequency band from 4 MHz to 8 MHz does not provide the same degree of improvement in classification performance. Therefore the cost of having the ability to obtain features over an 8 MHz frequency band, such as a second radar site, may not be warranted. Conversely, channel 4 demonstrated significant performance degredation in both cases of band reduction. Therefore, given a channel with an unknown additive component, a significant increase in performance may be obtained by extending the frequency band beyond 4 MHz.

Parameter Under Observation: Frequency Band Size
Channel Model: Coherent AWGN Channel
Azimuth angle: 45
Start Frequency: 8.0 MHz
Stop Frequency: Varies
Number of Frequencies: 10

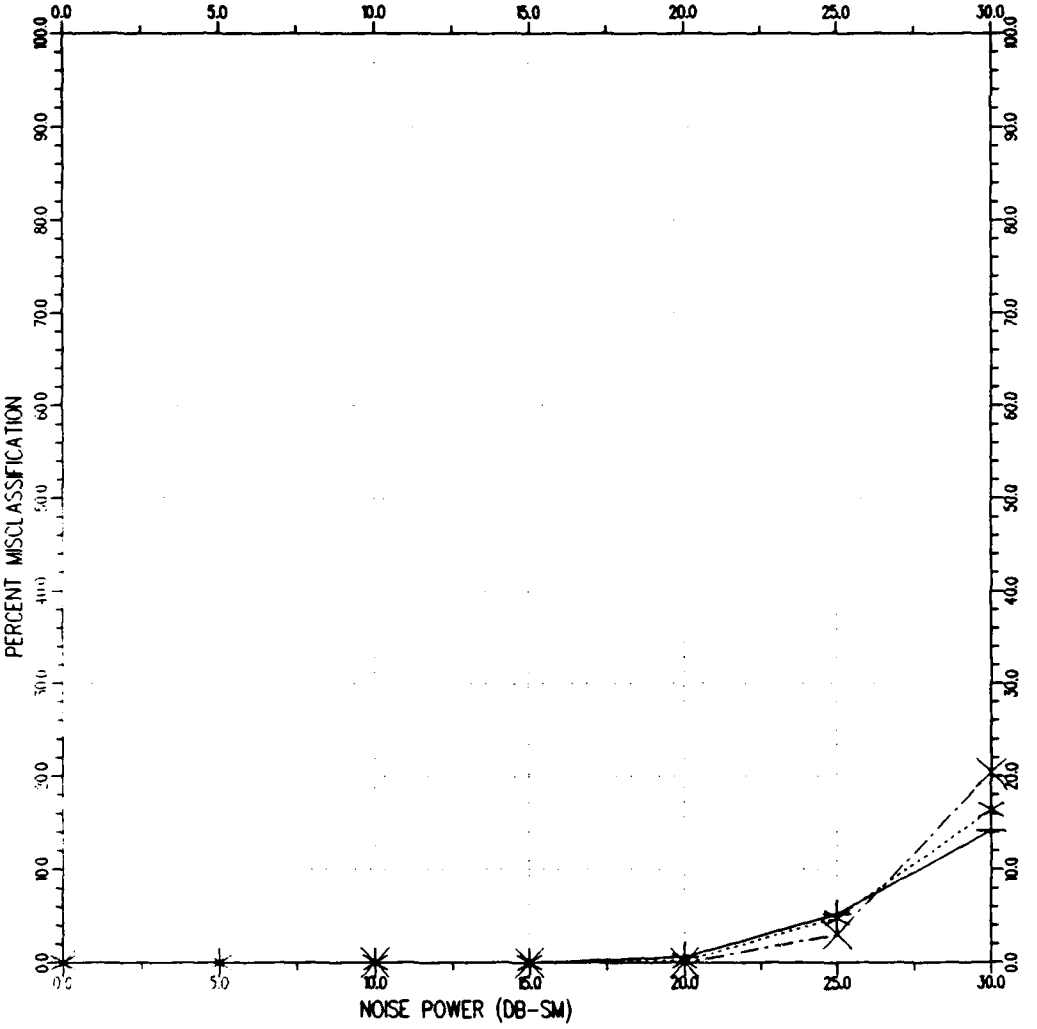

Figure 26: Coherent channel band size study.

Parameter Under Observation: Frequency Band Size
Channel Model: Non-Coherent AWGN Channel
Azimuth angle: 45
Start Frequency: 8.0 MHz
Stop Frequency: Varies
Number of Frequencies: 10

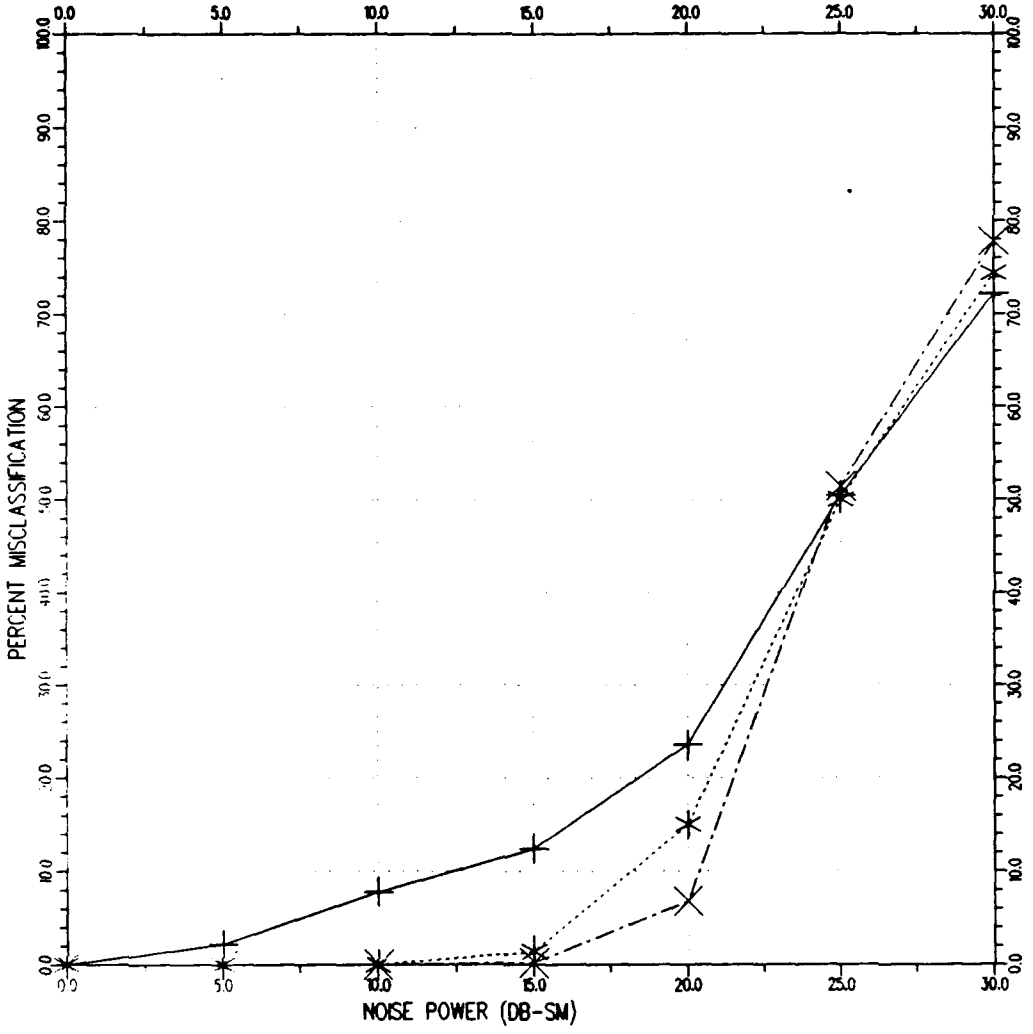

Figure 27: Non-Coherent channel band size study.

Parameter Under Observation: Frequency Band Size
Channel Model: Multiplicitive Component AWGN Channel
Azimuth angle: 45
Start Frequency: 8.0 MHz
Stop Frequency: Varies
Number of Frequencies: 10

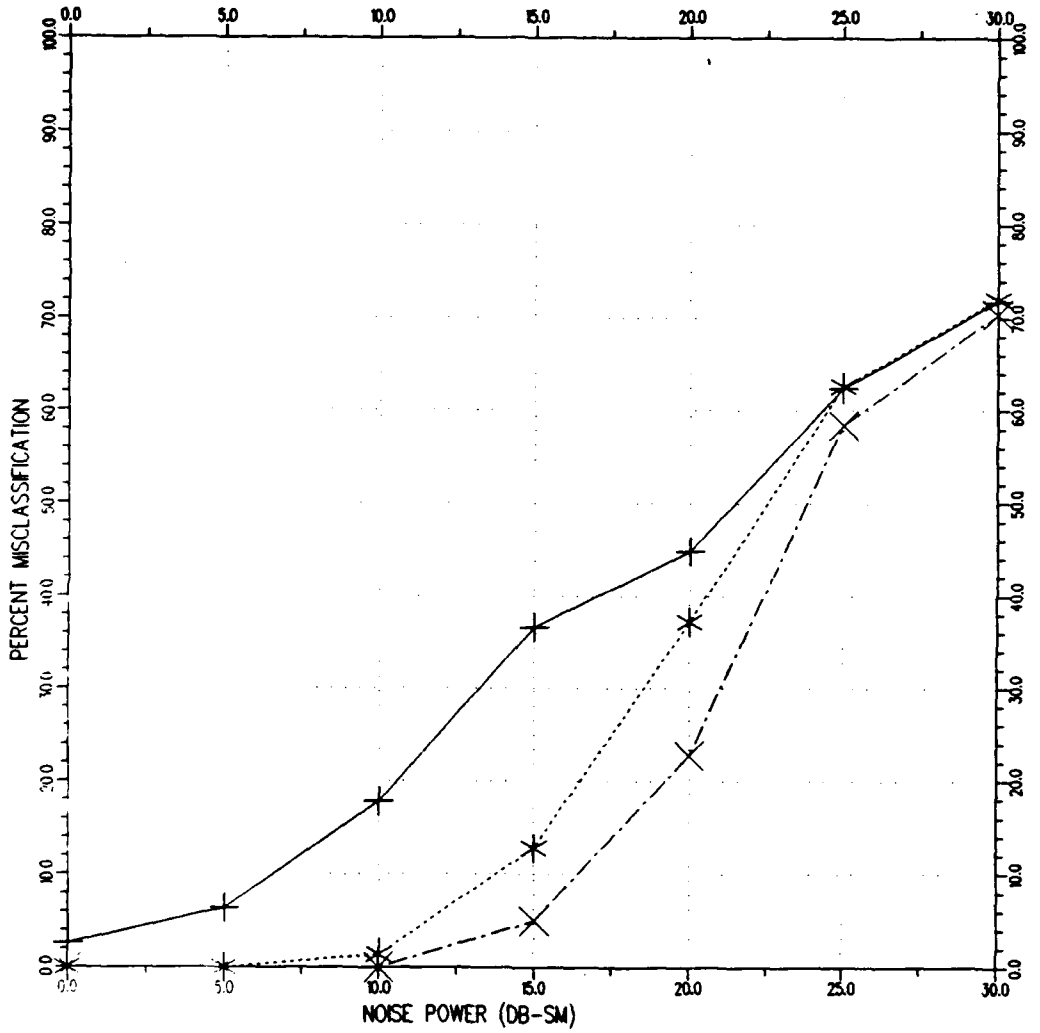

Figure 28: Multiplicitive component channel band size study.

Parameter Under Observation: Frequency Band Size
Channel Model: Additive Component AWGN Channel
Azimuth angle: 45
Start Frequency: 8.0 MHz
Stop Frequency: Varies
Number of Frequencies: 10

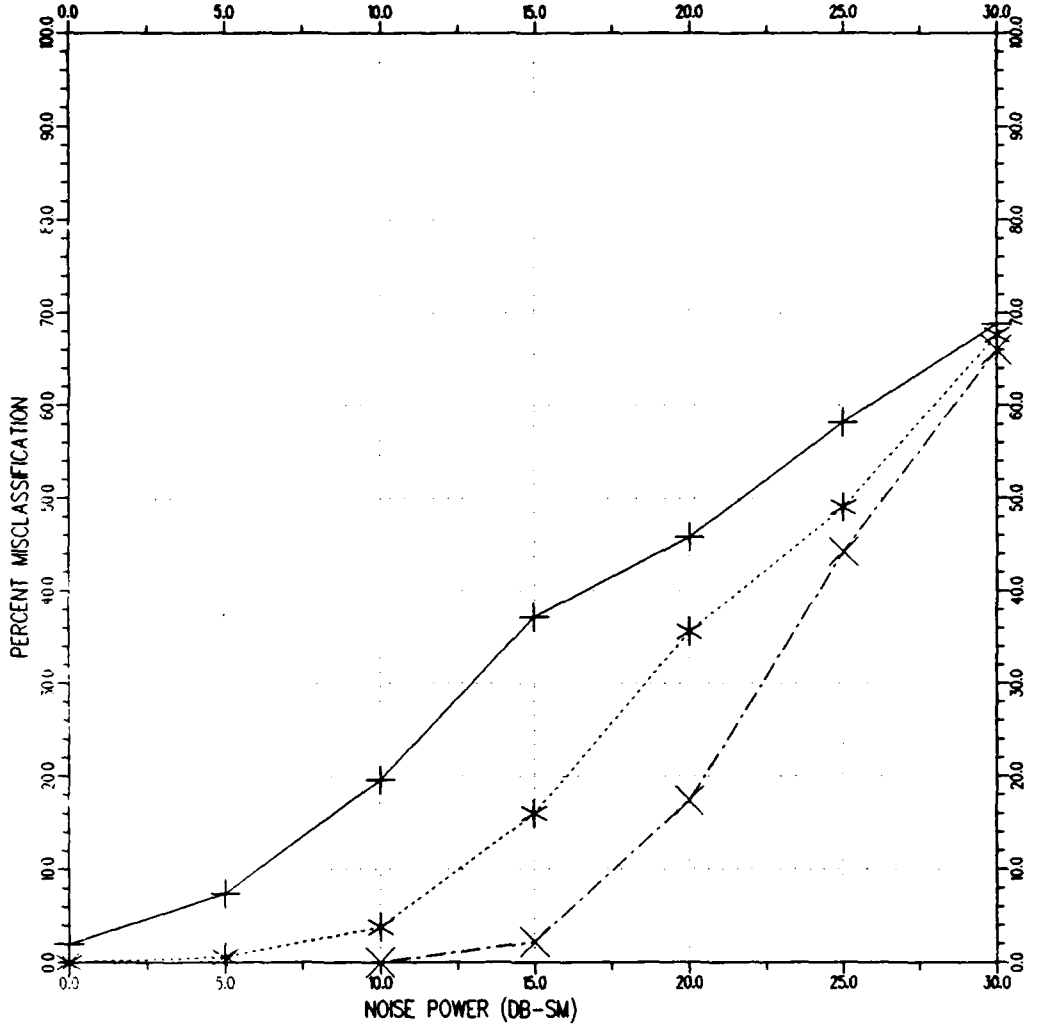

Figure 29: Additive component channel band size study.

5.2 Number of Features Study

A study was conducted to determine the relationship between the number of features used and the classification performance for the four channels. Previous research [2] concluded that the minimum frequency sampling interval which will satisfy Shannon's sampling criteria is given by:

$$\Delta f \leq \frac{c}{3.5L} \tag{5.1}$$

where c is the speed of light and L is the length of the target. Therefore given an average target length of 50 meters, one finds approximately 2, 3, and 5 frequency samples are required to meet the above criteria for band widths of 2 MHz, 4 MHz, and 8 MHz respectively. These values were used as minimum guidelines to be met for each corresponding frequency band. Since Kamis [2] examined the effect of the number of features at large frequency bands ($F_{band} \geq 8$ MHz) for channels 1 and 2, these bands for these channels were not included in the study.

Figure 30 shows a significant increase in noise immunity of approximately 5 dB-sm as the number of features through channel 1 are increased from 3 to 5 to 10 over the 2 MHz band. The increase in noise immunity of approximentally 5 dB-sm demonstrates that classification performance can be significantly improved. Figure 31 exhibits the smaller noise immunity of approximately 3dB-sm associated with channel 2 as the number of features is increased from 3 to 10. Figure 32 demontrates an almost constant increase of noise immunity of 3 dB-sm to 5 dB-sm as the number of features is increased from 3 to 5 to 10 to 20 in the channel with an unknown multipicitive component (channel 3). Figure 33 demonstrates a similar increase in performance for the unknown additive component channel.

Figures 30 through 33 illustrate that classification performance may be improved by increasing the number of features when limited to a 2 MHz frequency

band, irregardless of the channel. Channel 2 demonstrated the smallest increase in performance of the three, however, the increase is much greater than that observed by Kamis [2] when increasing the number of features over larger frequency bands of 8 MHz and 22 MHz.

Figures 34 and 35 show the relationship between the number of features and classification performance over 4 MHz and 8 MHz frequency bands for channel 3. Both figures indicate an additional noise immunity of approximated 3 to 5 dB as the number of features is increased from 5 to 10. A smaller increase in performance is obtained by increasing the number of features from 10 to 20 and 10 to 15 as shown in Figures 34 and 35 respectively. Therefore, as frequency band is increased, channel 3 demontrates a decrease in the amount of improvement in classification performance obtained by using an increased amount of features. Note that channel 2 displays this same property.Figure 36 demonstrates that the additive component channel exhibits the same properties as channel 2 and channel 3 concerning frequency band, number of samples, and classification performance.

Therfore, Figures 30 through 36 indicate that if one is limited to a small frequency band, it may be worth the cost of the additional processing time to obtain estimates at 10 or 20 frequencies regardless of the channel. However, if a larger frequency band is available, the additional processing cost may outweigh the slight increase in classification performance obtained through the additional features.

Parameter Under Observation: Number of Features
Channel Model: Coherent AWGN Channel
Azimuth angle: 0
Start Frequency: 8.0 MHz
Stop Frequency: 10.0 MHz
Number of Frequencies: Varies

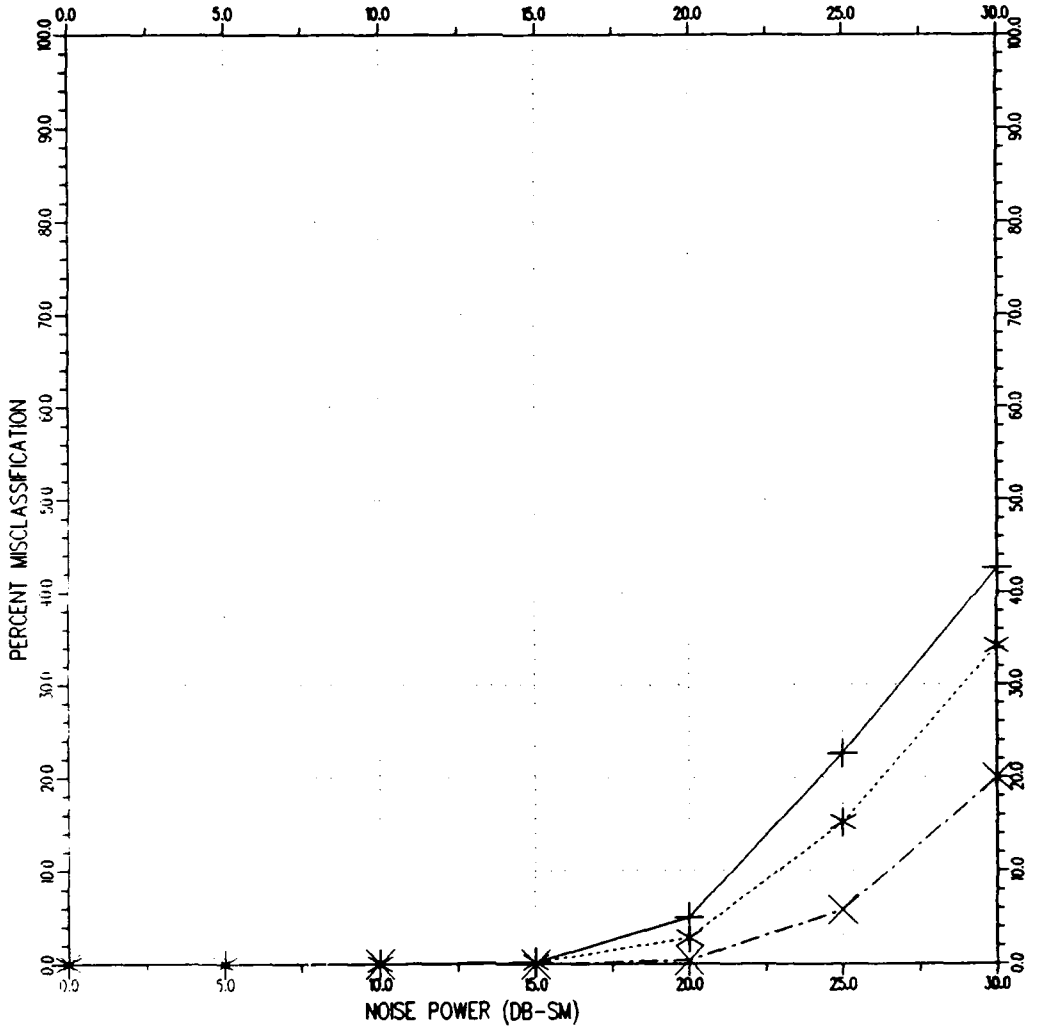

Figure 30: Coherent channel number of features study (8.0-10.0 MHz).

Parameter Under Observation: Number of features
Channel Model: Non-Coherent AWGN Channel
Azimuth angle: 0
Start Frequency: 8.0 MHz
Stop Frequency: 10.0 MHz
Number of Frequencies: Varies

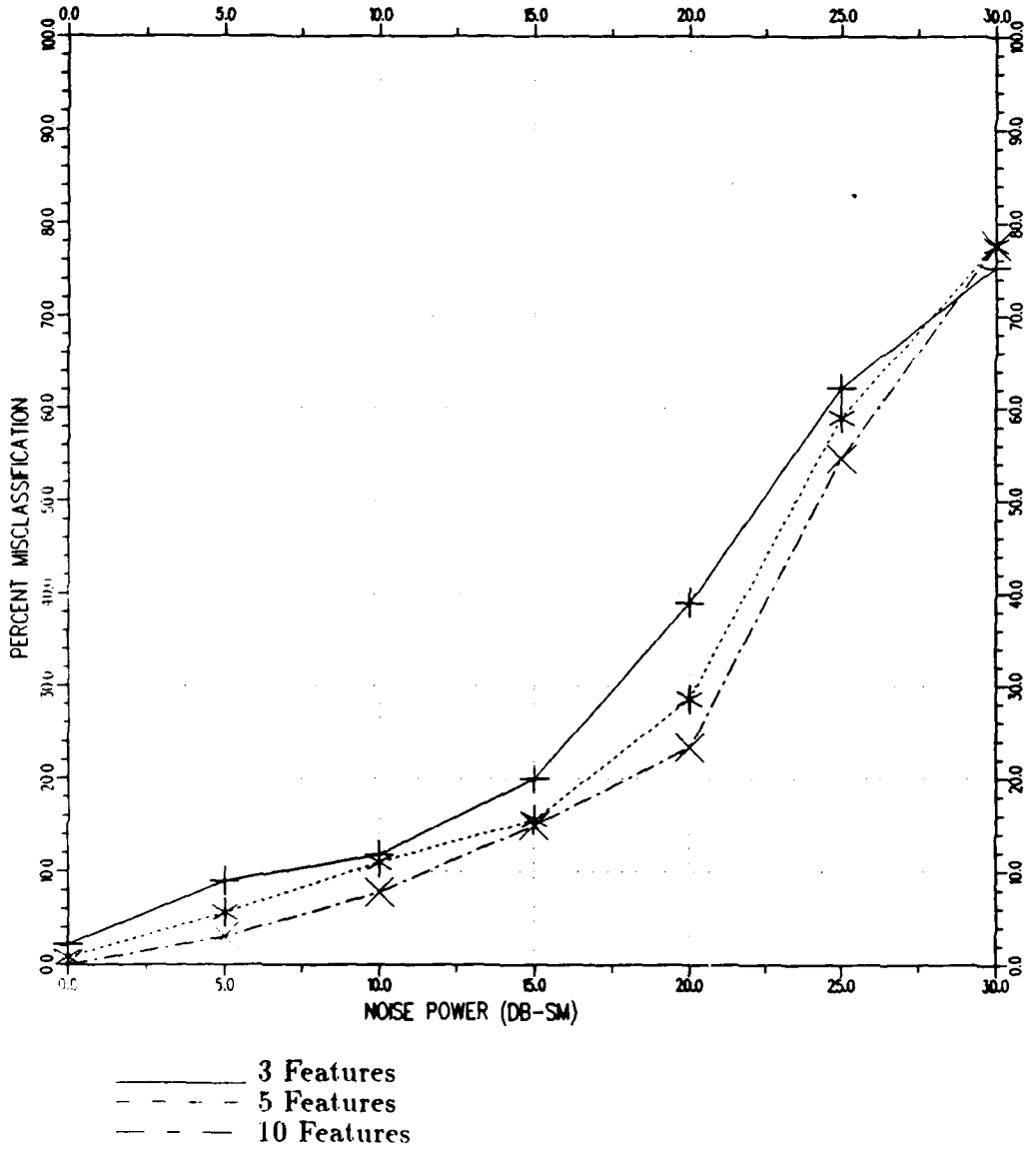

Figure 31: Non-Coherent channel number of features study (8.0-10.0 MHz).

Parameter Under Observation: Number of Features
Channel Model: Multiplicitive Component AWGN Channel
Azimuth angle: 0
Start Frequency: 8.0 MHz
Stop Frequency: 10.0 MHz
Number of Frequencies: Varies

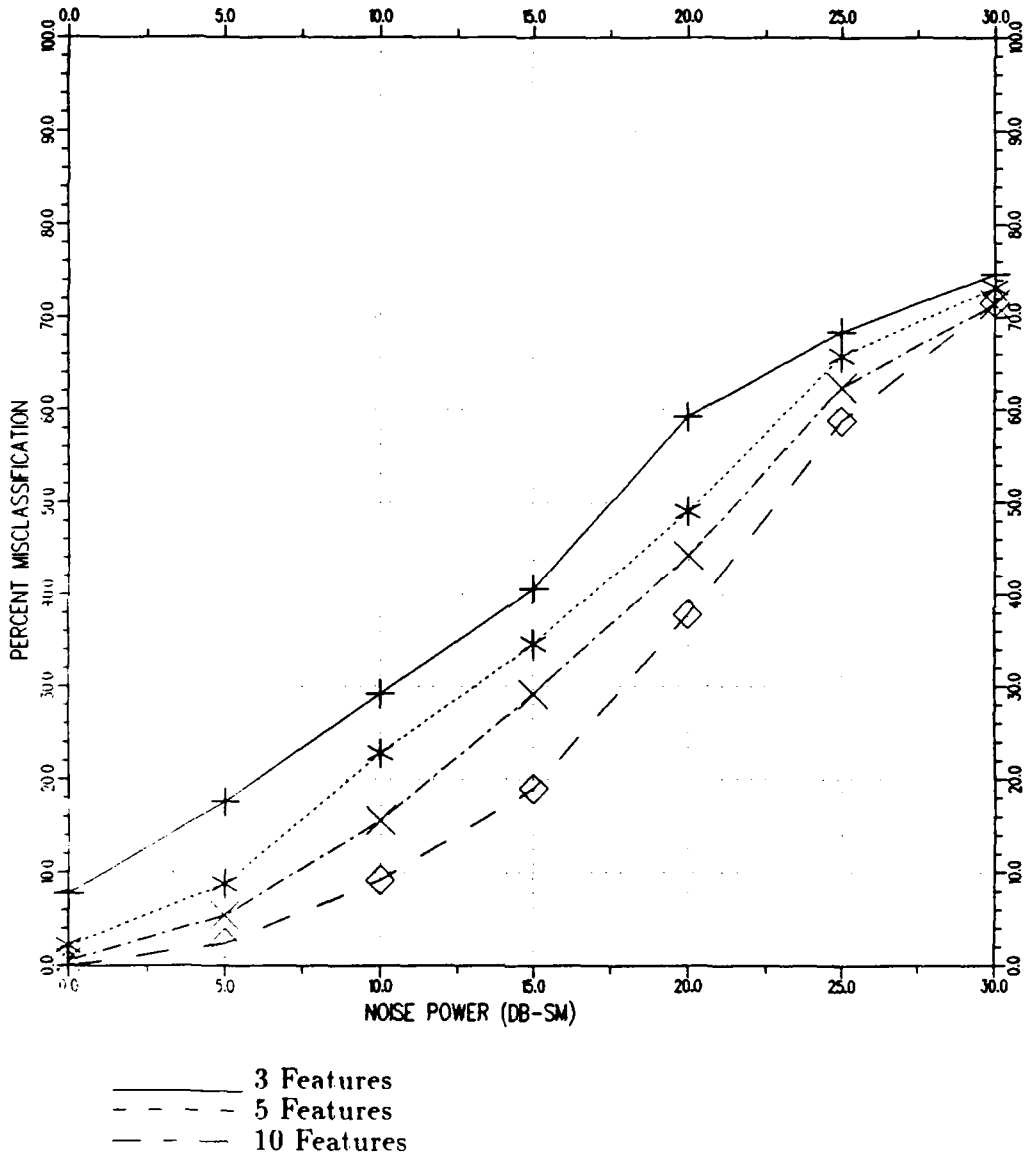

Figure 32: Multiplicitive component channel number of features study (8.0-10.0 MHz).

Parameter Under Observation: Number of Features
Channel Model: Additive Component AWGN Channel
Azimuth angle: 0
Start Frequency: 8.0 MHz
Stop Frequency: 10.0 MHz
Number of Frequencies: Varies

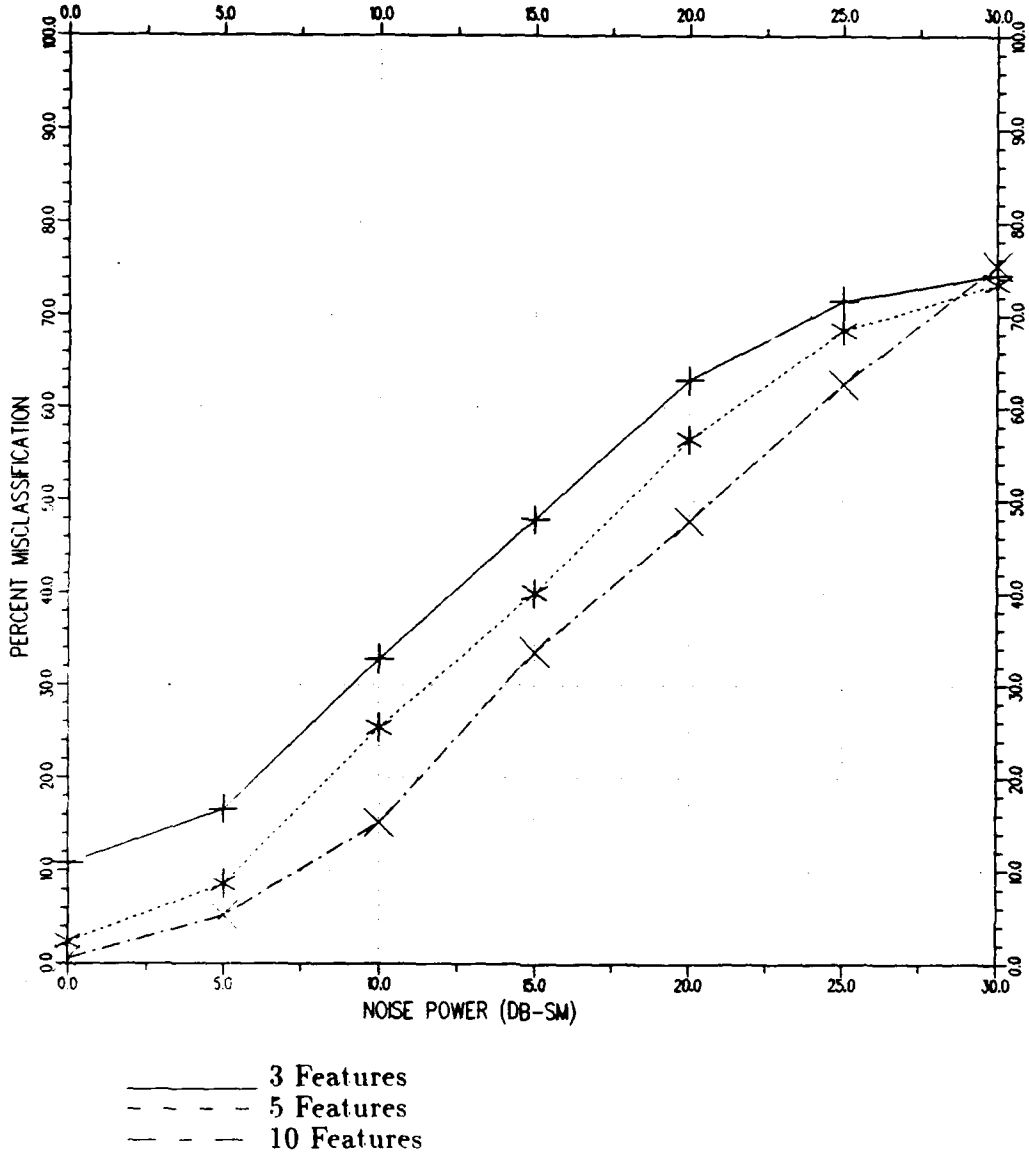

Figure 33: Additive component channel number of features study (8.0-10.0 MHz).

Parameter Under Observation: Number of Features
Channel Model: Multiplicitive Component AWGN Channel
Azimuth angle: 0
Start Frequency: 8.0 MHz
Stop Frequency: 12.0 MHz
Number of Frequencies: Varies

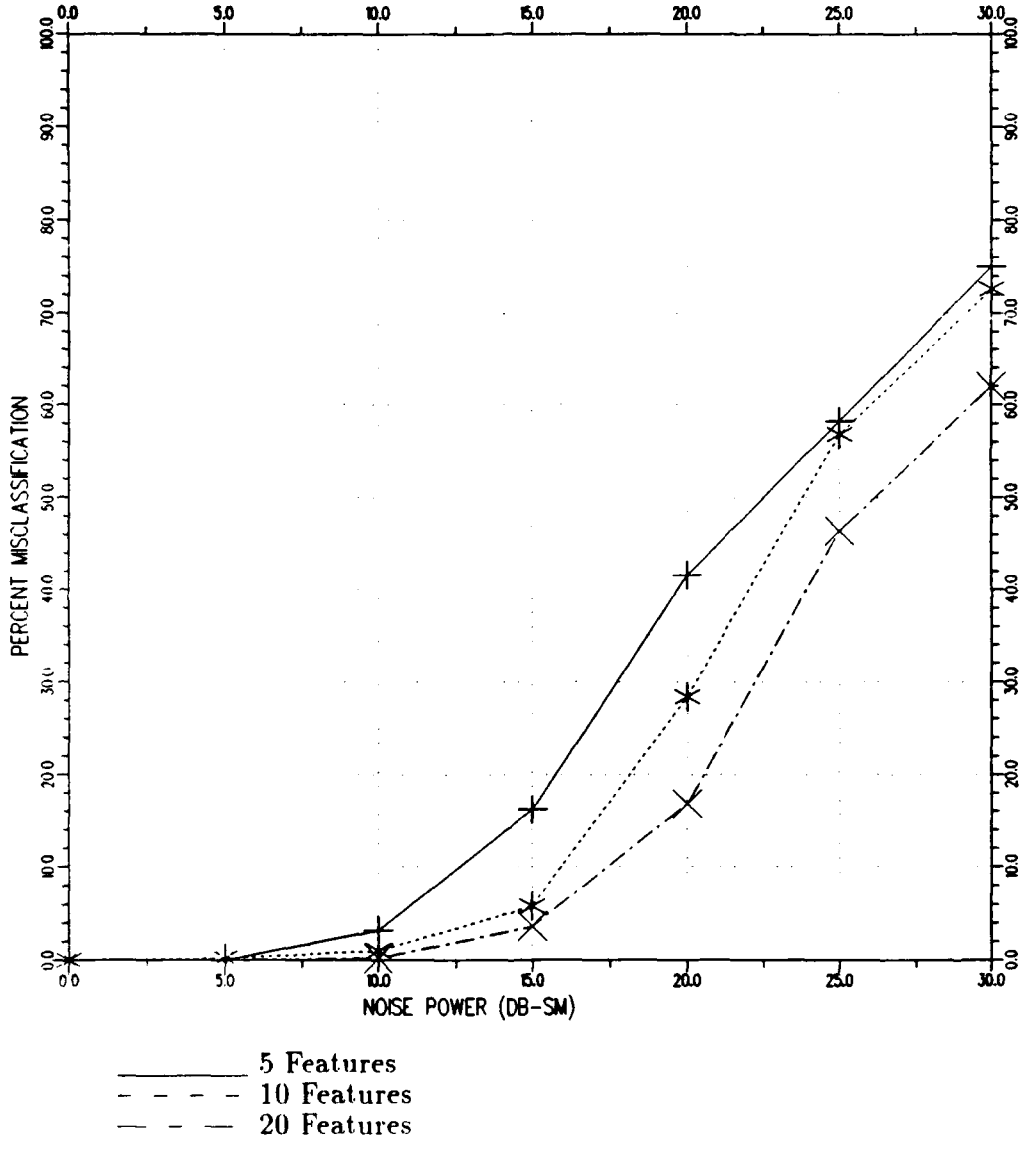

Figure 34: Multiplicitive component channel number of features study (8.0-12.0 MHz).

Parameter Under Observation: Number of Features
Channel Model: Multiplicitive Component AWGN Channel
Azimuth angle: 0
Start Frequency: 8.0 MHz
Stop Frequency: 16.0 MHz
Number of Frequencies: Varies

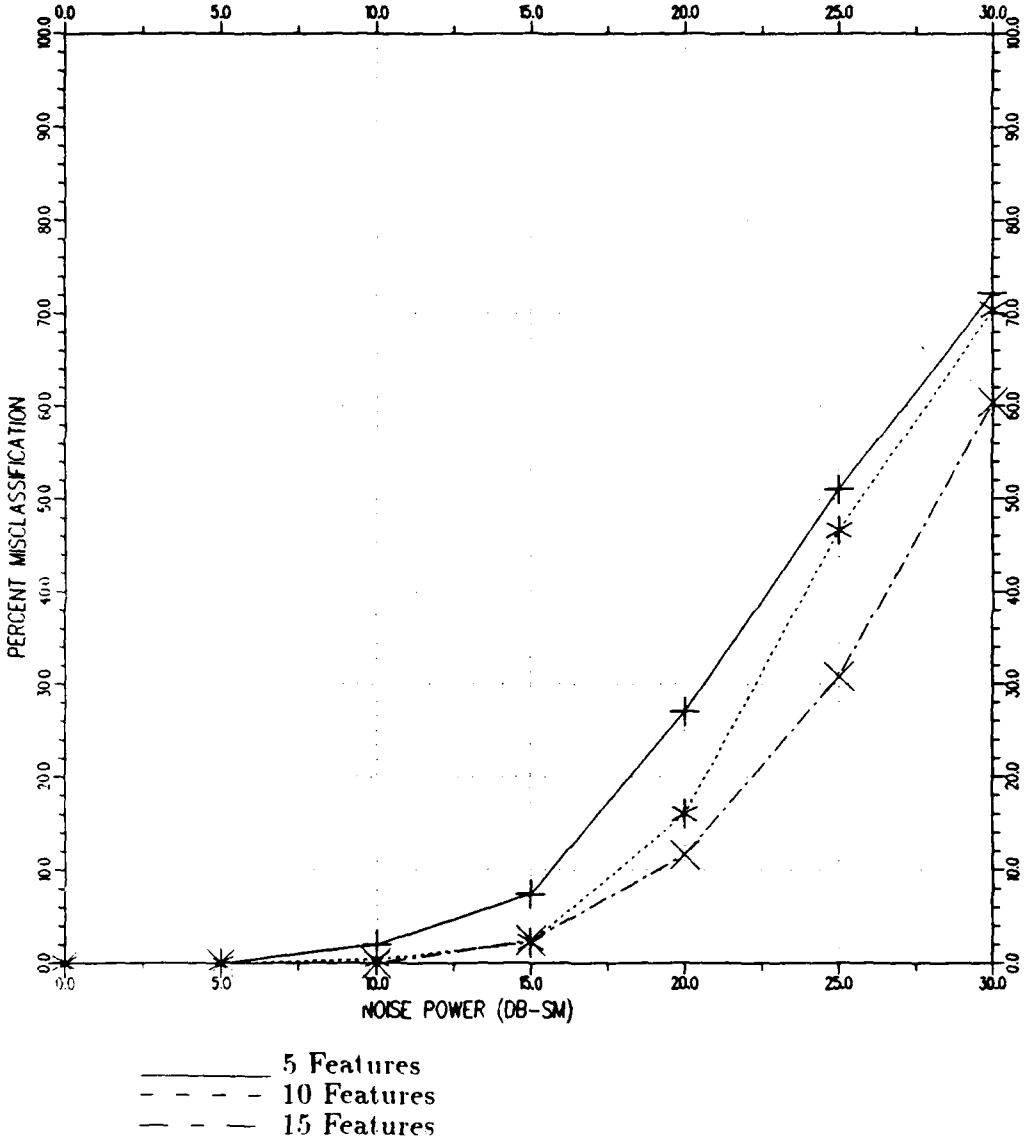

Figure 35: Multiplicitive component channel number of features study (8.0-16.0 MHz).

Parameter Under Observation: Number of Features
Channel Model: Additive Component AWGN Channel
Azimuth angle: 0
Start Frequency: 8.0 MHz
Stop Frequency: 16.0 MHz
Number of Frequencies: Varies

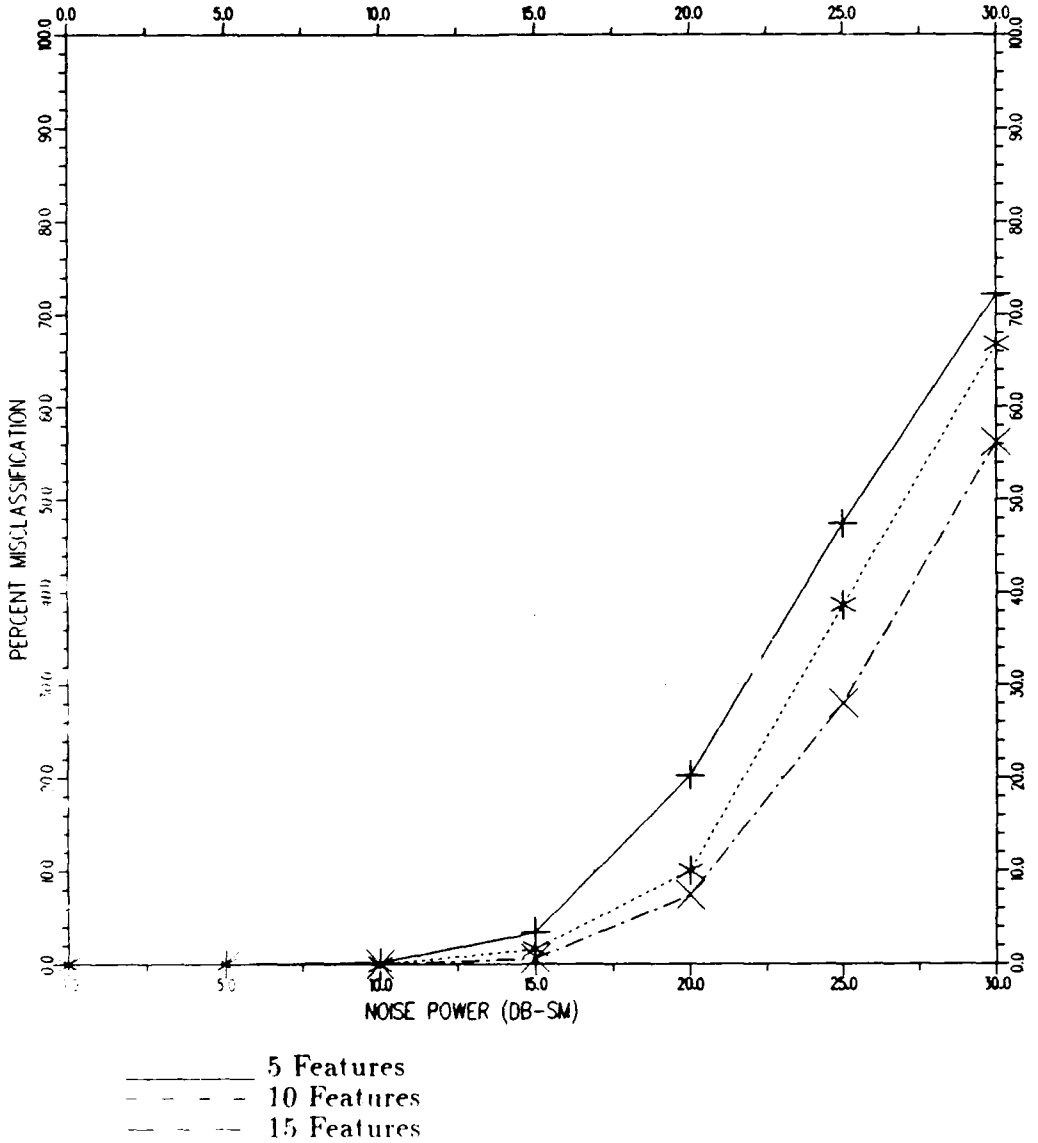

Figure 36: Additive component channel number of features study (8.0-16 MHz).

5.3 Comparison of AWGN Channels Performance

A direct comparison of the four channels has been made in terms of classification performance. Figure 37 demonstrates the dependence of classification performance on the channel given a 2 MHz frequency band. A significant performance degredation of at least 15 dBsm is experienced for channel 2 with respect to channel 1. The classification performance of channels 3 and 4 is further degraded as a result of target information lost in the normalization processes used to remove the unknown (multiplicitive or additive) components.

Figure 38 shows the resulting performance of the same channels over a wider 4 MHz frequency band. The performance of channels 2, 3, and 4 improves significantly with respect to the performance of channel 1. At lower noise powers, channel 3 is found to outperform channel 4 by a surprisingly wide margin of approximately 2 dBsm.Figure 39 compares the performance of the 4 channels over an 8 MHz bandwidth. The additive component channel now outperforms the multiplicitive channel. Note that the performance of channels 2, 3, and 4 all fall within 5 dBsm of each other.

Figures 37, 38, and 39 together indicate that channels with unknown multiplicitive or additive components which must be removed will always degrade performance. This is understandable, since information concerning target size is lost in the normalization process used to remove the unknown (multiplicitive or additive) component.More importantly, these figures indicate that the performance of a channel with an unknown additive component (channel 4) degrades at a faster rate with a narrowing frequency band than a channel with an unknown multiplicitive component (channel 3). Figures 37 and 38 clearly indicate that knowing the difference in absolute RCS between frequencies (channel 4) will not provide

any better performance over knowing only the relative change in RCS (channel 3). Finally, the three figures indicate that without phase information classification performance decreases dramatically with a decrease in frequency band.

Figures 40 and 41 show the classification performance of the four channels using 5 and 15 features respectively in the 8 MHz frequency band. Again, channel 1, which utilizes phase information, performs significantly better. Note that the relative performance of each channel with respect to the other three remains almost constant in both figures. Therefore all three channels tend to suffer the same loss of performance with the lowering of the number of frequencies in this large 8 MHz frequency band.

Figures 42 displays the resulting poor performance of channels 3 and 4 when the number of features is limited to three and the frequency band (2 MHz) is limited. The 9 dB-sm increase in noise power immunity of channel 2 with respect to channel 3 at the 20% misclassification level is one of the largest changes in performance found between the two channels.

Figure 43 demonstrates the relatively large improvement in classification performance of channel 3 with respect to channel 2, especially at noise power levels of less than 5 dB-sm. This increase in relative classification performance demostrates that the performance of channel 3 degrades faster than the performance of channel 2 when the number of features is decreased. This same property was noted in the number of features study. Finally, Figure 44 demonstrates an even smaller decrease in classification performance for channel 3, further backing the performance loss — number of frequency relationship for channel 3 at small bandwidths.

Figures 45 and 46 compare the channels over a different band from 20 MHz to 24 MHz and 20 MHz to 28 MHz. The channels demonstrate the same characteristics over these bands as over the 8 MHz to 12 MHz and 8 MHz to 16 MHz bands.

Therefore the channel characteristics which have been noted do not appear to be dependent on the exact band in the HF spectrum used, but only depend on the size of the band.

Parameter Under Observation: Channel
Channel Model: Varies
Azimuth angle: 45
Start Frequency: 8.0 MHz
Stop Frequency: 10.0 MHz
Number of Frequencies: 10

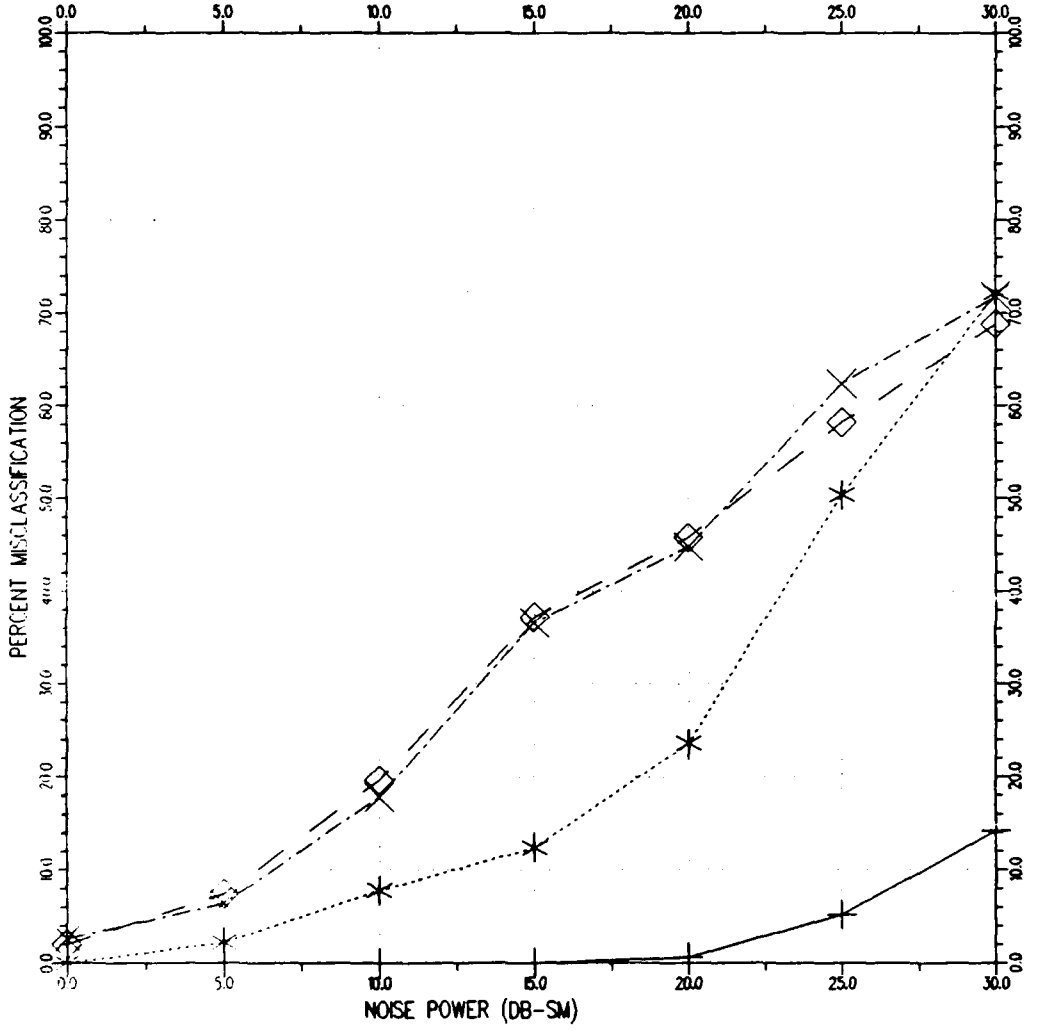

Coherent Channel
Non-Coherent Channel
Multiplicitive Component Channel
Additive Component Channel

Figure 37: Channel study over 2 MHz band.

Parameter Under Observation: Channel
Channel Model: Varies
Azimuth angle: 45
Start Frequency: 8.0 MHz
Stop Frequency: 12.0 MHz
Number of Frequencies: 10

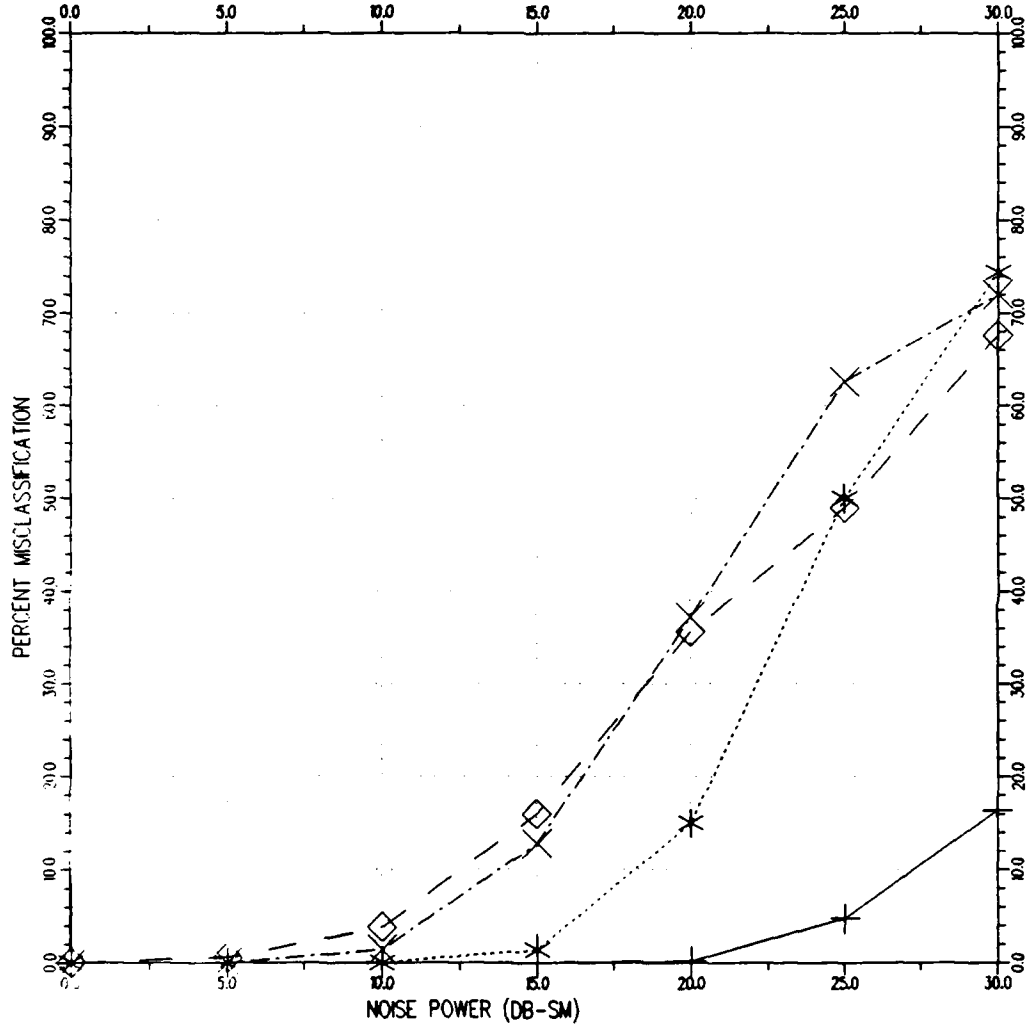

Figure 38: Channel study over 4 MHz band.

Parameter Under Observation: Channel
Channel Model: Varies
Azimuth angle: 45
Start Frequency: 8.0 MHz
Stop Frequency: 16.0 MHz
Number of Frequencies: 10

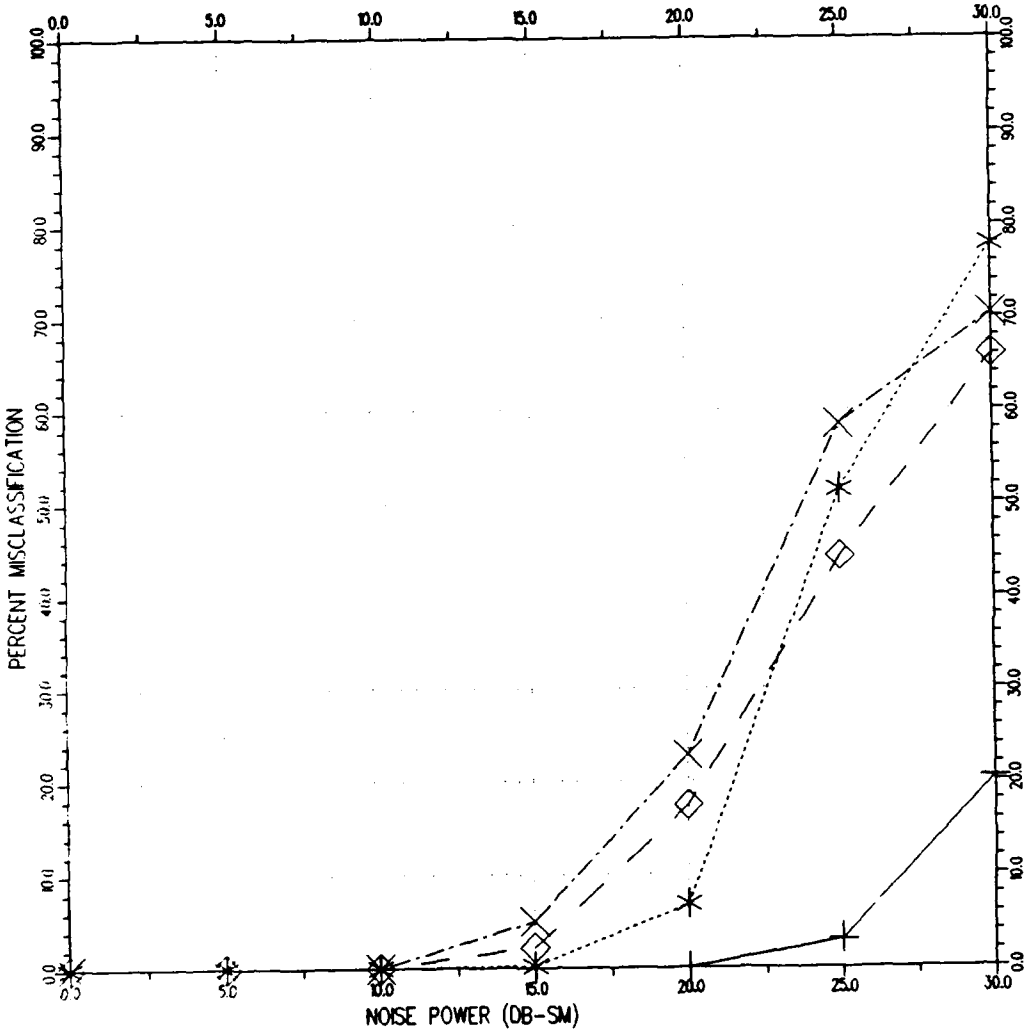

Figure 39: Channel study over 8 MHz band.

Parameter Under Observation: Channel
Channel Model: Varies
Azimuth angle: 0
Start Frequency: 8.0 MHz
Stop Frequency: 16.0 MHz
Number of Frequencies: 5

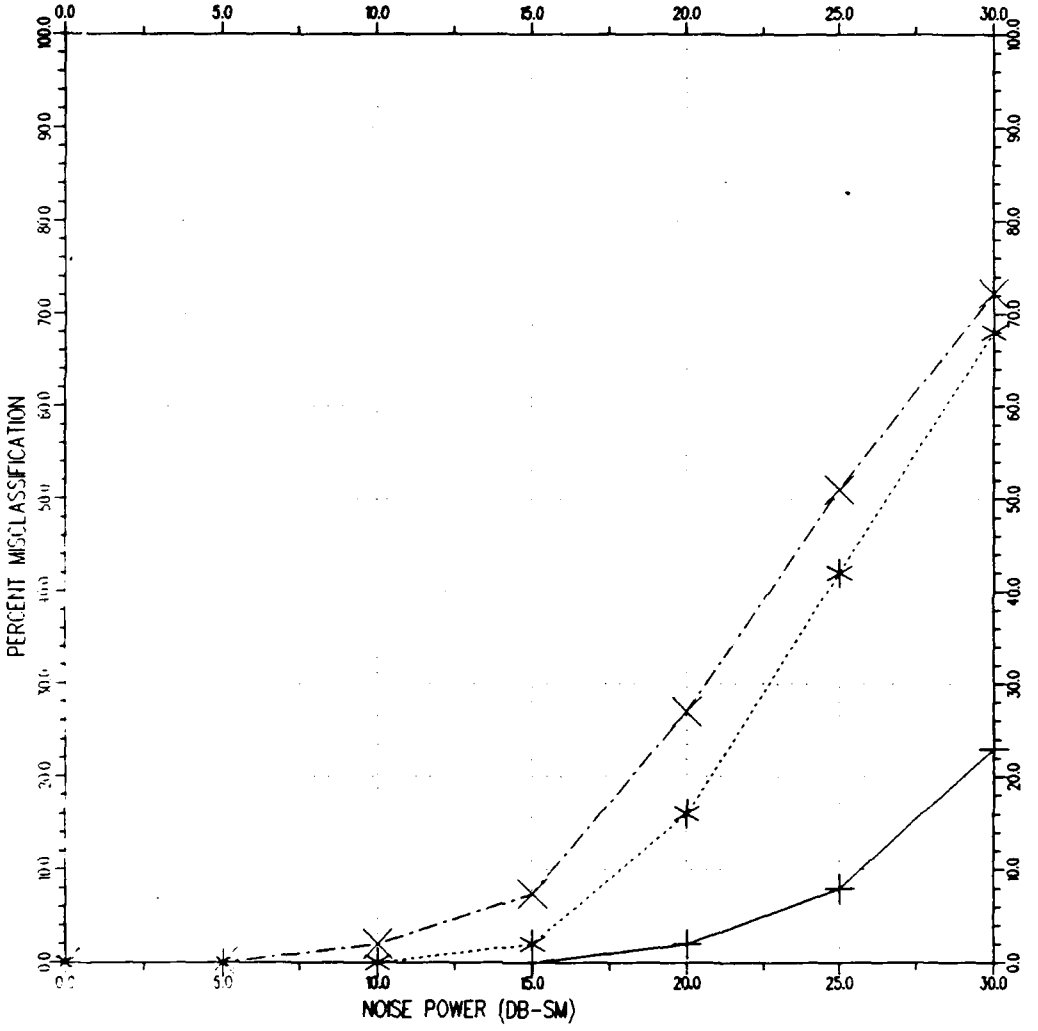

Figure 40: Channel study for 5 frequency, 8 MHz band.

Parameter Under Observation: Channel
Channel Model: Varies
Azimuth angle: 0
Start Frequency: 8.0 MHz
Stop Frequency: 16.0 MHz
Number of Frequencies: 15

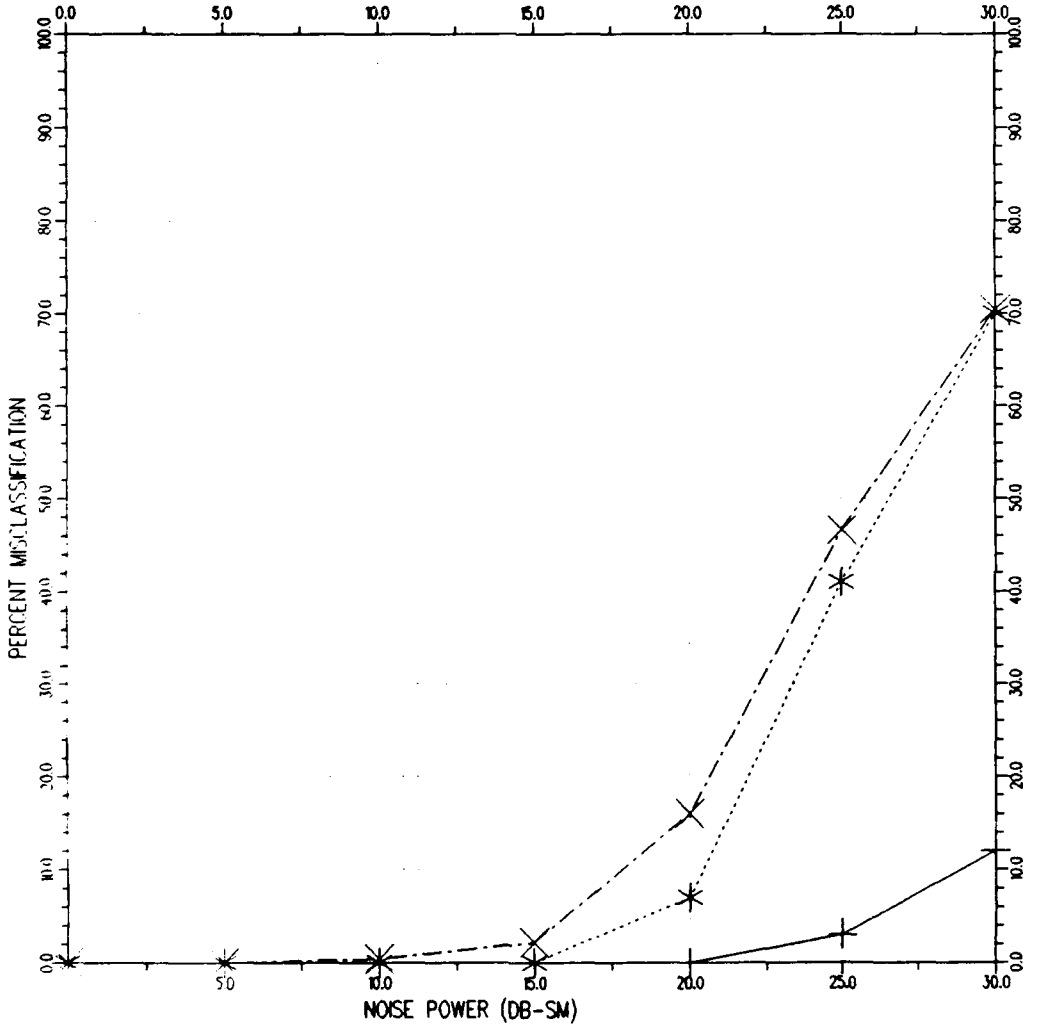

Figure 41: Channel study for 15 frequency, 8 MHz band.

Parameter Under Observation: Channel
Channel Model: Varies
Azimuth angle: 0
Start Frequency: 8.0 MHz
Stop Frequency: 10.0 MHz
Number of Frequencies: 3

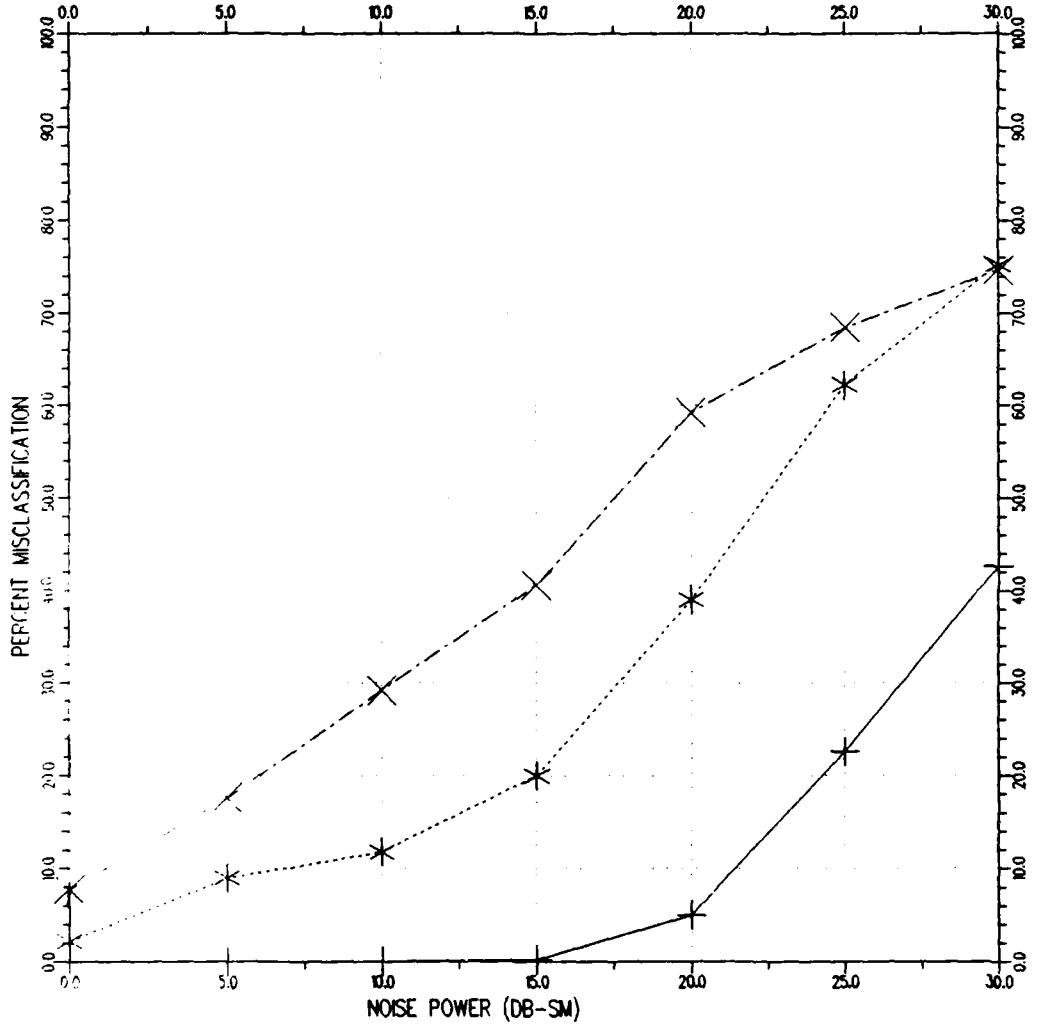

Figure 42: Channel study for 3 frequency, 2 MHz band.

Parameter Under Observation: Channel
Channel Model: Key
Azimuth angle: 0
Start Frequency: 8.0 MHz
Stop Frequency: 10.0 MHz
Number of Frequencies: 5

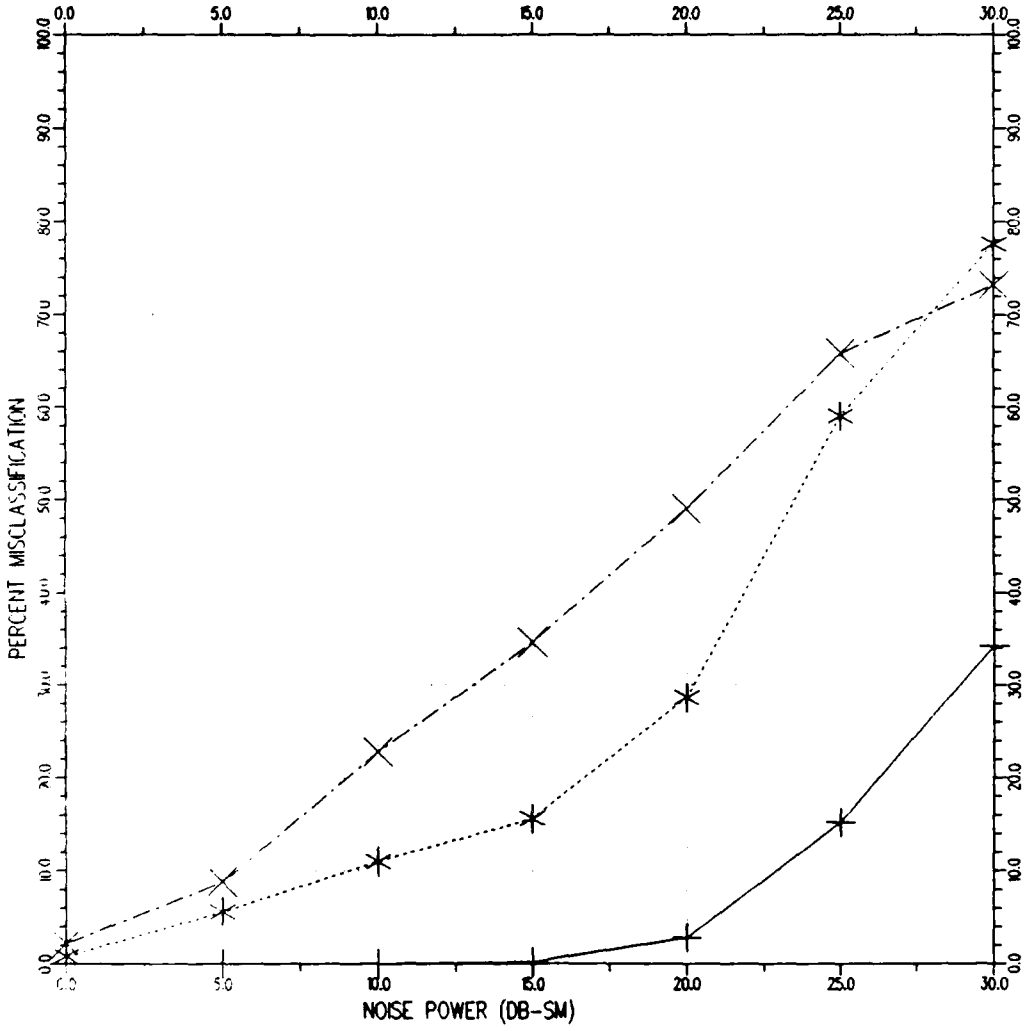

Figure 43: Channel study for 5 frequency, 2 MHz band.

Parameter Under Observation: Channel
Channel Model: Key
Azimuth angle: 0
Start Frequency: 8.0 MHz
Stop Frequency: 10.0 MHz
Number of Frequencies: 10

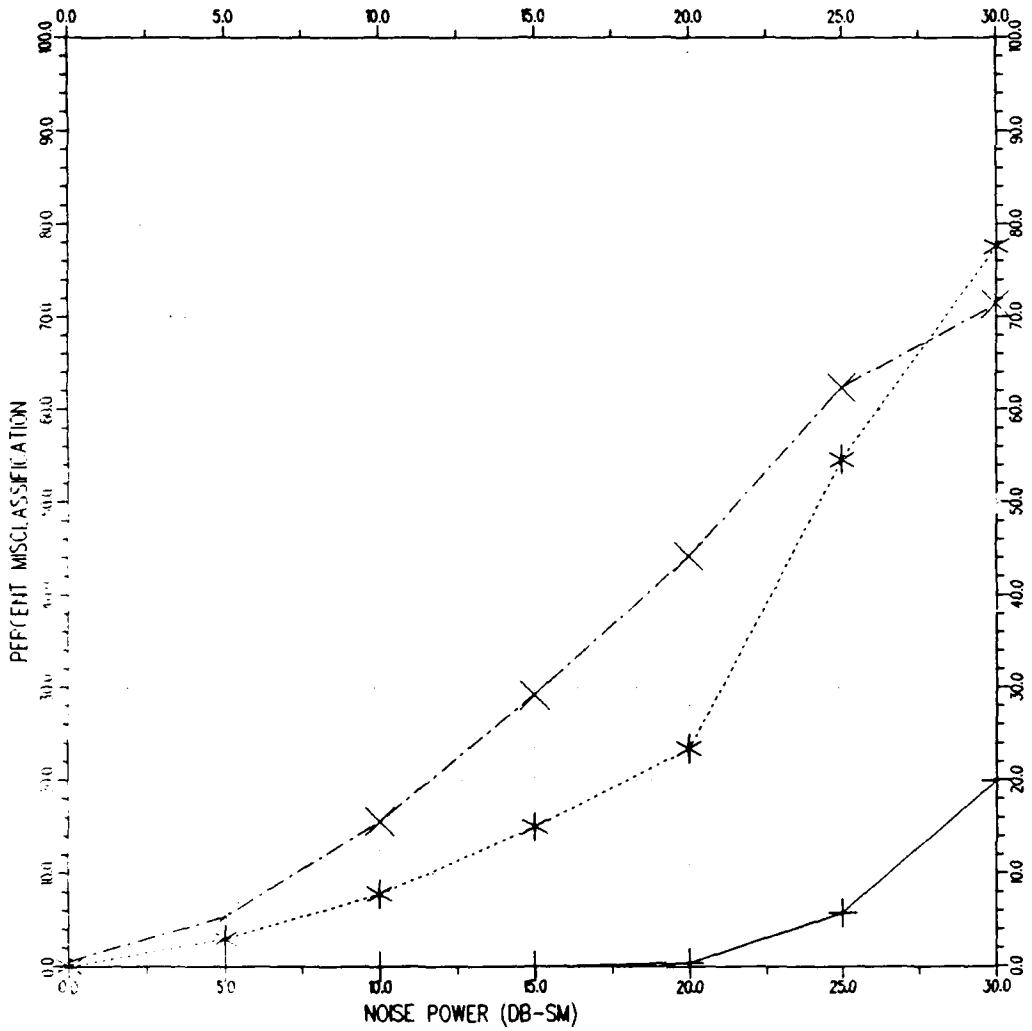

Figure 44: Channel study for 10 frequency, 2 MHz band.

Parameter Under Observation: Channel
Channel Model: Key
Azimuth angle: 45
Start Frequency: 20.0 MHz
Stop Frequency: 24.0 MHz
Number of Frequencies: 10

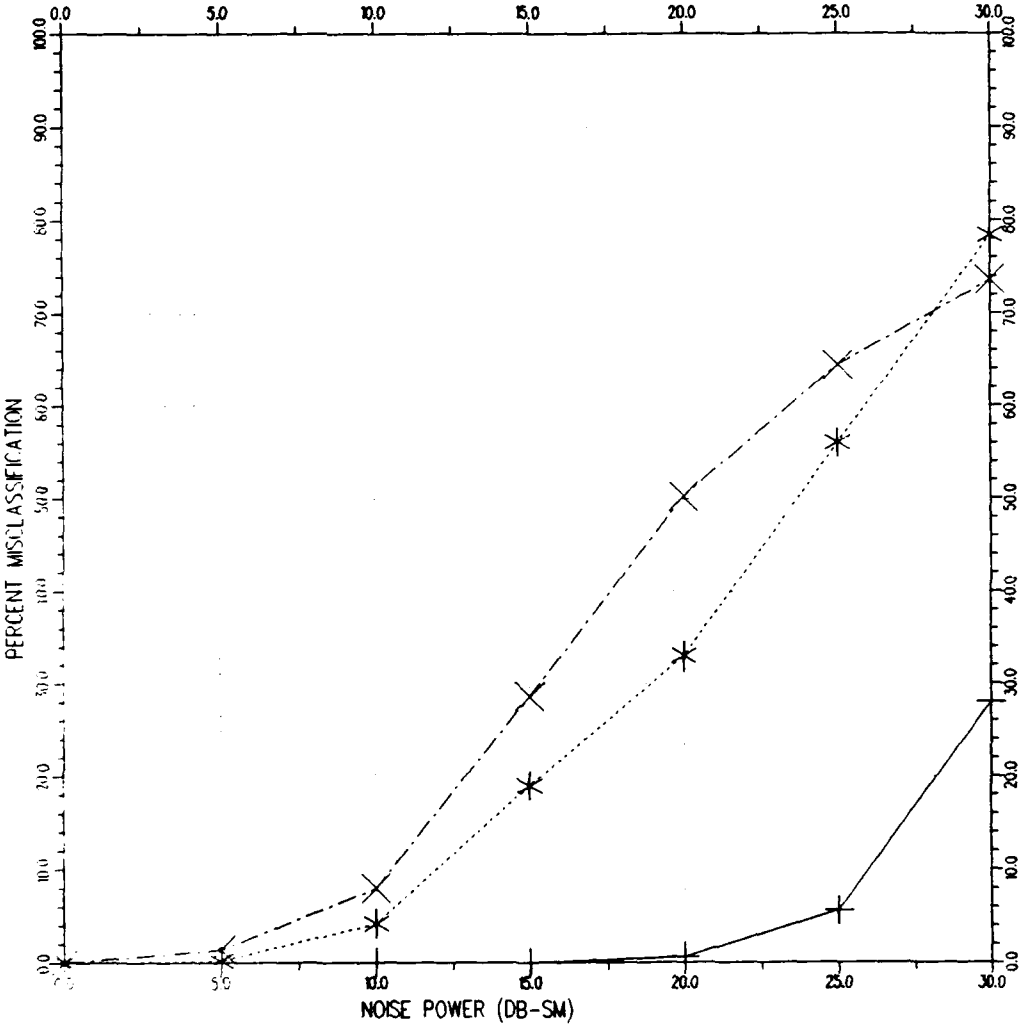

Figure 45: Channel study for upper 4 MHz band

Parameter Under Observation: Channel
Channel Model: Key
Azimuth angle: 45
Start Frequency: 20.0 MHz
Stop Frequency: 28.0 MHz
Number of Frequencies: 10

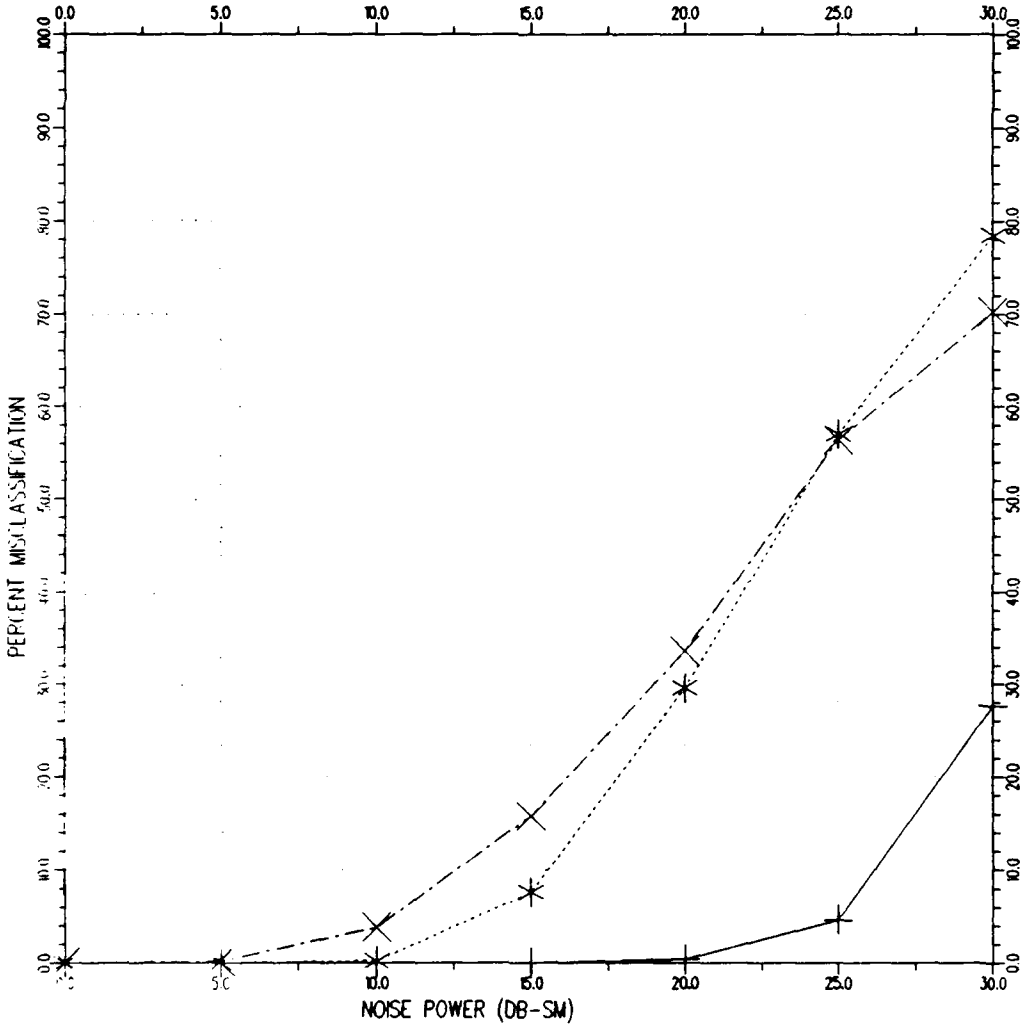

Figure 46: Channel study for upper 8 MHz band.

CHAPTER VI

RELATIVE PHASE CHANNEL MODEL

6.1 Feature Implementation

The development of the W feature in Section 3.5 was intended to provide information related to the intrinsic phase of the target at times when the accurate estimation of absolute path length is difficult to achieve. It has previously been shown that given certain channel conditions one may create $(N-1)$ target features from the difference of the intrinsic phases at adjacent frequencies. These $(N-1)$ features, coupled with N estimates of the RCS of the target at each frequency, provide a total $(2N-1)$ features of the target which may be used for classification purposes. The $(N-1)$ W features contain additional information about the target provided they are not too severely affected by noise. If used correctly in a classification algorithm along with the amplitude features, these W features should improve classification performance over that of using the amplitude features only.

A variation of the nearest-neighbor algorithm was developed to incorporate the W features in the classification process. Previous experience has shown the nearest-neighbor algorithms can provide powerful classification performance results [2], and therefore have been used as the starting point. In addition, the use of a distance metric makes intuitive sense in a problem of this nature. Consider two catalog targets ($k = 1, 2$) whose backscatter amplitudes ($\sqrt{RCS}$) measured at f_1, f_2, and f_3 are plotted in 3 dimensional space as in Figure 47. These two targets

have two corresponding intrinsic W values each given by Eq. (6.1) and Eq. (6.2) which may be plotted in 2-dimensional space as shown in Figure 48.

$$W_k(f_1) = \theta_k(f_2) - \frac{f_2}{f_1}\theta_k(f_1), \qquad k = 1,2 \tag{6.1}$$

$$W_k(f_2) = \theta_k(f_3) - \frac{f_3}{f_2}\theta_k(f_2), \qquad k = 1,2 \tag{6.2}$$

where $\theta_k(f_i)$ = intrinsic phase of target K at frequency f_i.

Next consider estimating the corrupted amplitude and corrupted W values of an unknown target u at the corresponding frequencies f_1, f_2, and f_3 and plotting the estimates in Figure 47 and Figure 48 as shown. Use of a Euclidian distance metric provides four distinct measures as given in Eq. (6.3), Eq. (6.4), Eq. (6.5), and Eq. (6.6).

$$d^A_{u,1} = \left[\sum_{i=1}^{3}(A_1(f_i) - A_u(f_i))^2\right]^{\frac{1}{2}} \tag{6.3}$$

$$d^A_{u,2} = \left[\sum_{i=1}^{3}(A_2(f_i) - A_u(f_i))^2\right]^{\frac{1}{2}} \tag{6.4}$$

$$d^W_{u,1} = \left[\sum_{i=1}^{2}(W_1(f_i) - W_u(f_i))^2\right]^{\frac{1}{2}} \tag{6.5}$$

$$d^W_{u,2} = \left[\sum_{i=1}^{2}(W_2(f_i) - W_u(f_i))^2\right]^{\frac{1}{2}} \tag{6.6}$$

A final distance between the unknown target and the two catalog targets may then be constructed as:

$$d^{A+W}_{u,1} = d^A_{u,1} + \rho Q d^W_{u,1} \qquad \text{(meters)} \tag{6.7}$$

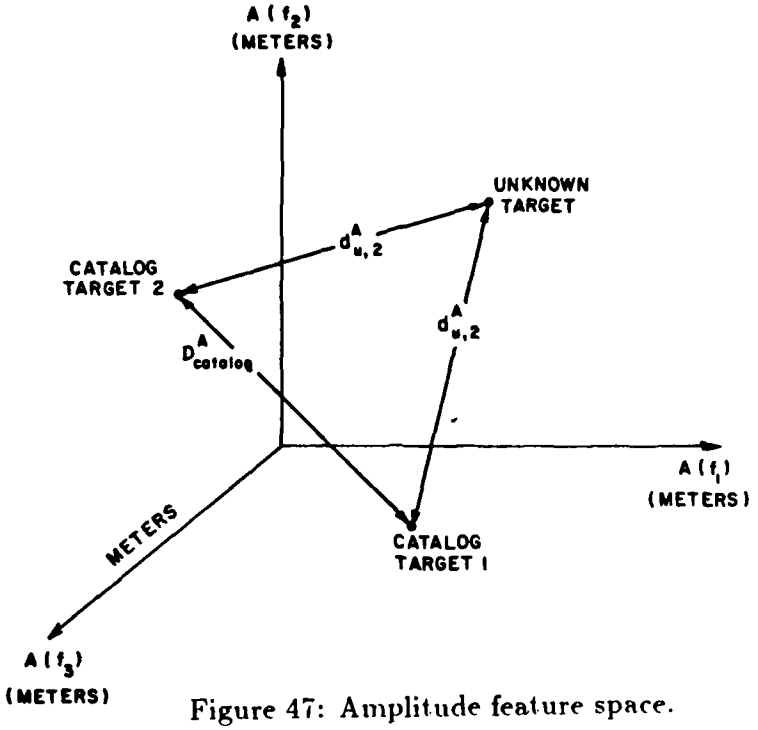

Figure 47: Amplitude feature space.

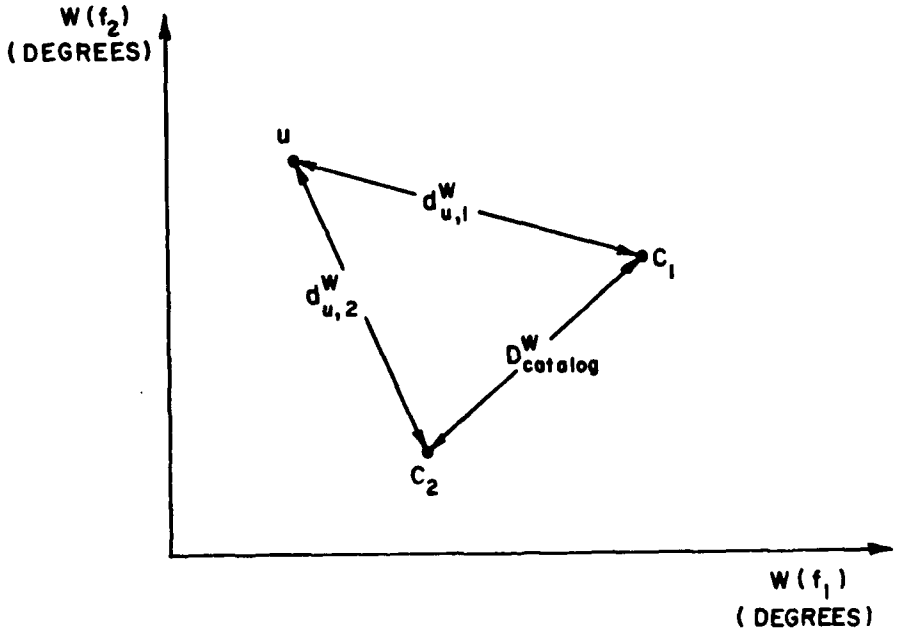

Figure 48: Phase feature space.

$$d_{u,2}^{A+W} = d_{u,2}^{A} + \rho Q d_{u,2}^{W} \qquad \text{(meters)} \tag{6.8}$$

where the ρ term provides a weighting of the W metric, while the Q term provides a unit conversion from an angle measure to a length measure.

The Q term, labeled the catalog normalization factor, is a measure of the separation of the targets in the catalog set. In Figure 47 , the average separation of the two catalog targets in terms of amplitude features may be calculated by Eq. (6.9).

$$D_C^A = \left[\sum_{i=1}^{3} (A_2(f_i) - A_1(f_i))^2\right]^{\frac{1}{2}} \qquad \text{(meters)} \tag{6.9}$$

Likewise, the average separation of the catalog targets in terms of W features may be calculated by Eq. (6.10).

$$D_C^W = \left[\sum_{i=1}^{2} (W_2(f_i) - W_1(f_i))^2\right]^{\frac{1}{2}} \qquad \text{(degrees)} \tag{6.10}$$

The ratio of these two terms, as given by Eq. (6.11), provides the catalog normalization factor.

$$Q_C = \frac{D_C^A}{D_C^W} \tag{6.11}$$

The catalog normalization factor may be viewed in the following manner. Figures 47 and 48 show the same two catalog targets in terms of two different metrics separated by two different average distances as calculated in Eq. (6.9) and Eq. (6.10). By multiplying the W features of the catalog set by Q (rescaling the phase feature space), one can find the new average separation of the catalog targets in terms of the W features as:

$$\tilde{D}_C^W = \left[\sum_{i=1}^{2} (QW_2(f_i) - QW_1(f_i))^2\right]^{\frac{1}{2}} \tag{6.12}$$

$$\bar{D}_C^W = \left[Q^2 \sum_{i=1}^{2} (W_2(f_i) - W_1(f_i))^2 \right]^{\frac{1}{2}} \tag{6.13}$$

$$\bar{D}_C^W = Q \cdot D_C^W \tag{6.14}$$

$$\bar{D}_C^W = D_C^A \tag{6.15}$$

Therefore multiplying the catalog W features by Q has the effect of converting the W feature space to an amplitude feature space by using average target separation as the conversion factor. Likewise, the rescaling of $d_{u,k}^W$ by Q as shown in Eq. (6.7) and Eq. (6.8) has the same resulting effect.

The value of ρ, the W feature weight, reflects the emphasis placed on the W features in the classification process. For ρ=0, the W features are ignored, and the classification decision is solely determined by the amplitude distance. For $\rho > 1$, the normalized W features are more heavily weighted than the amplitude features.

In order to determine a proper value of ρ, one must consider the radar system from which the estimates of amplitude and phase are made. In general, the degree of corruption of the W features, with respect to the amplitude features, will determine the emphasis or de-emphasis of the normalized W-distance measure.

6.2 Channel Simulation

The relative phase channel model was simulated as follows. The W values of the catalog set were first created using the complex backscattered coefficients previously loaded in the catalog set. The normalization factor of the catalog set was then created by:

$$Q_{catalog} = \frac{\sum_{b=1}^{4} \sum_{a=b+1}^{5} \left[\sum_{i=1}^{N} (A_a(f_i) - A_b(f_i))^2 \right]^{\frac{1}{2}}}{\sum_{b=1}^{4} \sum_{a=b+1}^{5} \left[\sum_{i=1}^{N-1} (W_a(f_i) - W_b(f_i))^2 \right]^{\frac{1}{2}}} \tag{6.16}$$

where $A_a(f_i)$, $A_b(f_i)$ are the backscatter amplitudes of catalog targets a and b, and $W_a(f_i)$, $W_b(f_i)$ are the W values of catalog targets a and b. A corrupt test set vector was formed through the addition of coherent zero mean Gaussian noise to a high accuracy test set vector as described earlier. The $(N-1)$ noisy W features were then created from these coherent backscatter amplitudes by:

$$\tilde{W}_u(f_i) = \tan^{-1}\left(\frac{\tilde{X}_T(f_{i+1})}{\tilde{R}_T(f_{i+1})}\right) - \frac{\lambda_i}{\lambda_{i+1}}\tan^{-1}\left(\frac{\tilde{X}_T(f_i)}{\tilde{R}_T(f_i)}\right) \qquad i = 1, N-1 \quad (6.17)$$

where

$$\tilde{X}_T(f_i) = X_T(f_i) + N', \text{ and}$$
$$\tilde{R}_T(f_i) = R_T(f_i) + N'',$$

given $R_T(f_i)$, $X_T(f_i)$ are the high accuracy complex backscatter coefficients of test target T at frequenct f_i (or f_{i+1}), and N', N'' are i.i.d. Gaussian noise samples. Note that the distribution if $\tilde{W}_u(f_i)$ is going to be dependent on $A_T(f_i)$ and the distribution of $\tilde{A}_u(f_i)$. This may be visualized in Figure 49. This graphic description of the addition of coherent noise to a large and small target shows the strong dependence of standard deviation of $\tilde{W}_u(f_i)$ on the uncorrupted amplitude $A_T(f_i)$ of the data point. Therefore targets with large RCS values are biased toward having W features that are less corrupted for a given noise power.

An understanding of the relationships between the distributions of $\tilde{W}_u(f_i)$ and $\tilde{A}_u(f_i)$ for given values of $A_T(f_i)$ and levels of noise power is important in order to determine sensible values of ρ. To accomplish this, a study was conducted by first selecting targets with a wide range of backscatter amplitudes. The standard deviation of the W features were estimated as described in Degroot [10] by:

$$\sigma_{\tilde{W}(f_i)} = \left[\frac{1}{99}\sum_{r=1}^{100}\left(\min\left(W_T(f_i) - \tilde{W}_T^r(f_i)\right)\right)^2\right]^{\frac{1}{2}} \quad (6.18)$$

where $W_T(f_i)$ is the high accuracy W feature and $W_T^r(f_i)$ is the rth independent corrupt W feature. The min statement specifies the minimum angle between the values to eliminate branch cut effects. In a similar manner, the standard deviation of the corrupted amplitude features was calculated by Eq. (6.19).

$$\sigma_{\tilde{A}(f_i)} = \frac{1}{99}\left[\sum_{r=1}^{100}(A_k(f_i) - \tilde{A}_T^r(f_i))^2\right]^{\frac{1}{2}} \tag{6.19}$$

Estimates of $\sigma_{\tilde{W}(f_i)}$ versus $A(f_i)$ at noise power levels of 10 dB-sm and 20 dB-sm are shown in Figure 50. Note that $\sigma_{\tilde{W}(f_i)}$ is highly dependent on both $A(f_i)$ and the noise power. As a result, one may desire to weight the distance between an unknown W feature at frequency f_n and the catalog W feature at f_n dependent on the amplitude feature $\tilde{A}_u$ at that frequency. The standard deviation of the amplitude feature ($\sigma_{\tilde{A}_{(f_i)}}$) was found to be almost independent of $A(f_i)$ and only dependent on noise power. Estimated values were $\sigma_{\tilde{A}_{(f_i)}} \approx 0.3$ sm and 1.0 sm at noise power values of 10 dBsm and 20 dBsm, respectively. The previous study led to the development of two W feature distance measurements. The standard amplitude distance measurement given by:

$$d_{u,k}^A = \left[\sum_{i=1}^{N}\left(A_k(f_i) - \tilde{A}_u(f_i)\right)^2\right]^{\frac{1}{2}} \tag{6.20}$$

was used to measure the distance between catalog target k and unknown target u in terms of amplitude features. One W distance measurement was given by:

$${}_1d_{u,k}^W = \left[\sum_{i=1}^{N-1}\left(W_k(f_i) - \tilde{W}_u(f_i)\right)^2\right]^{\frac{1}{2}} \tag{6.21}$$

where $W_k(f_i)$ and $\tilde{W}_u(f_i)$ represent the catalog and corrupted W features respectively. A second W distance measurement was given by:

$${}_2d_{u,k}^W = \left[\sum_{i=1}^{N-1} R(\tilde{A}(f_i))\left(W_k(f_i) - \tilde{W}_u(f_i)\right)^2\right]^{\frac{1}{2}} \tag{6.22}$$

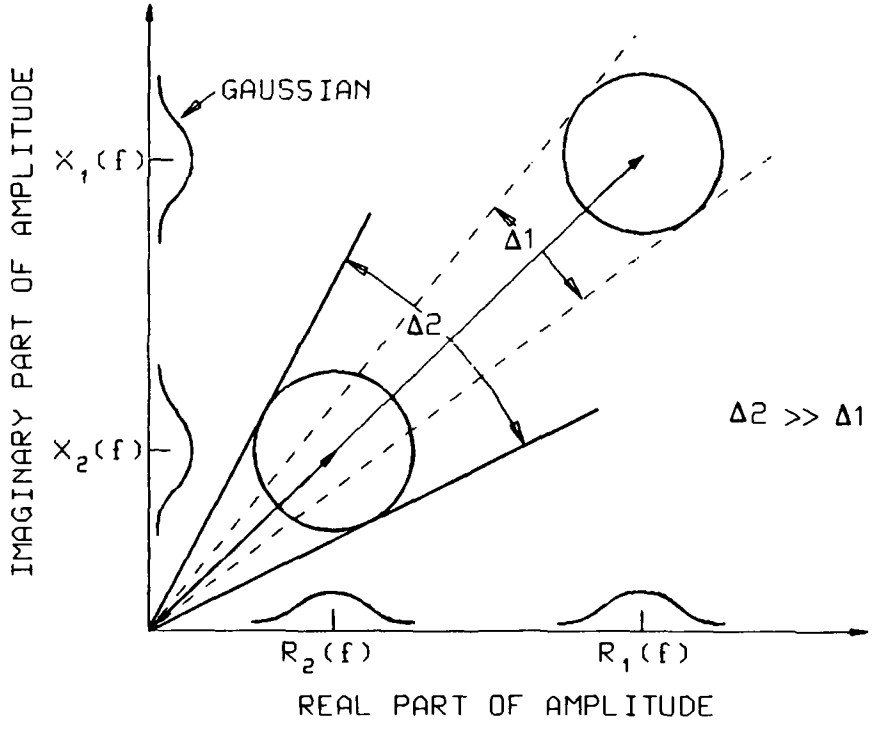

Figure 49: Graphic description of feature distributions.

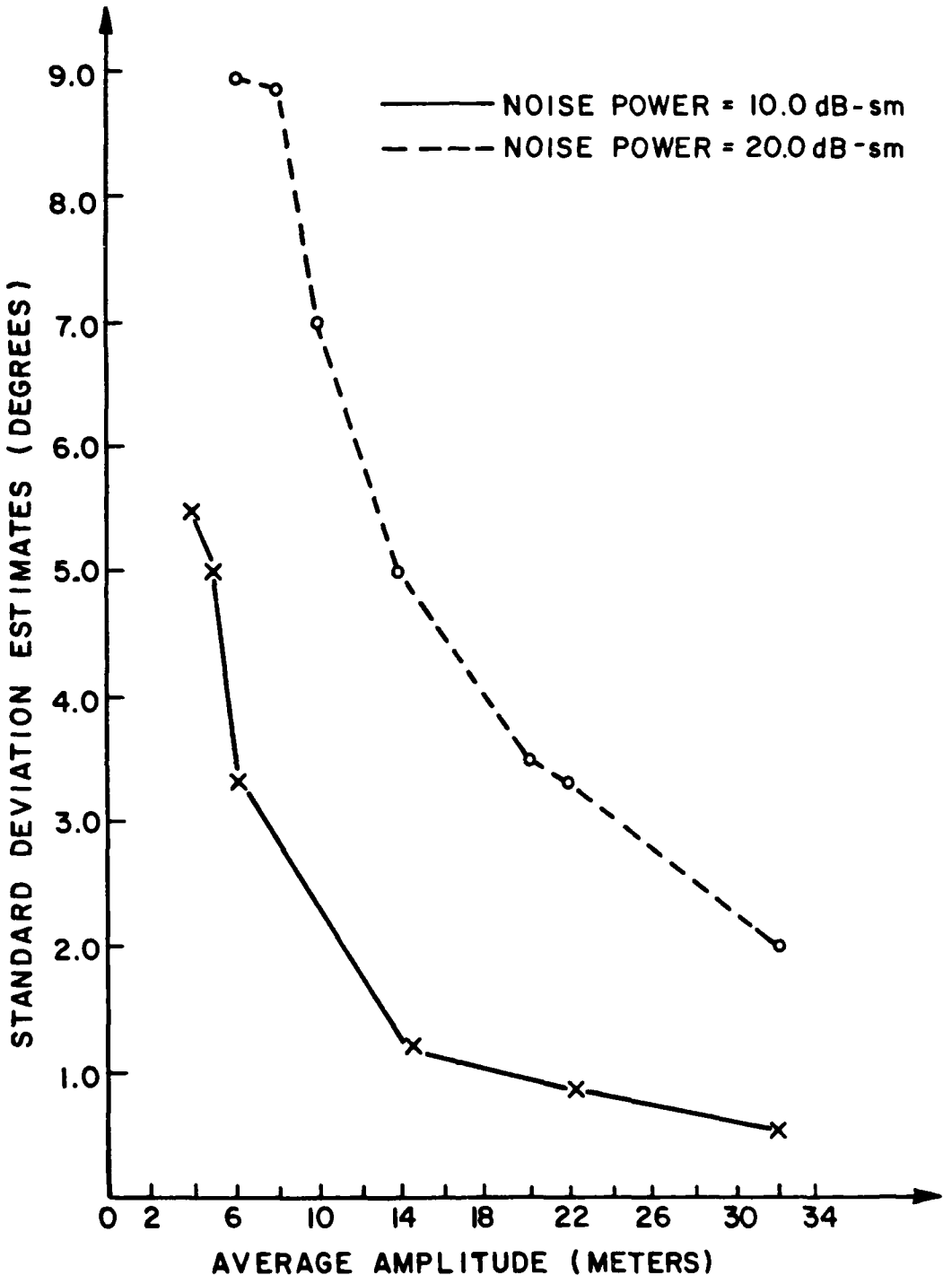

Figure 50: Estimated $\sigma_{\tilde{W}(f_i)}$ versus $A(f_i)$.

where $R(\tilde{A}(f_i))$ is a function of the corrupted amplitude of the test vector. $R(\tilde{A}(f_i))$ is a weight which approaches one for large values of $\tilde{A}(f_i)$ ($\sigma_{\tilde{A}(f_i)}$ small) and approaches 0 for small values of $\tilde{A}(f_i)$ ($\sigma_{\tilde{A}(f_i)}$ large). Note that the amplitudes of the corrupted vector must be used and not the amplitudes of the catalog presently being tested agianst. Use of the uncorrupted catalog amplitudes would bias ${}_2d^W_{u,k}$ to be small for small targets and large for large targets, therefore biasing the classification decision.

6.3 Experimental Results

Classification runs were made using Eq. (6.21) for ${}_1d^W_{u,k}$ to determine the effects of ρ on the classification algorithm. Figures 51, 52, and 53 show the results of nine tests run over three separate frequency bands. Figure 51 demonstrates an average improvement of 6 dB-sm of noise power immunity using the weight of $\rho = 1.0$ over the small 2 MHz band. However, Figures 52 and 53 demonstrate a loss in performance as the ${}_1d^W_{u,k}$ distance weight is increased. These results indicate that the ${}_1d^W_{u,k}$ distance measure is less than optimal since it weights all W features equally, irregardless of the amount of corruption of the W feature.

A second set of tests were performed to investigate possible functions for $R(\tilde{A}(f_i))$ given in Eq. (6.22). In this set of tests the weighting was set at $\rho = 0.5$. The two functons chosen for $R(\tilde{A}(f_i))$ were:

$$R(\tilde{A}(f_i)) = \frac{\tilde{A}(f_i)}{36.0}, \tag{6.23}$$

and

$$R(\tilde{A}(f_i)) = \left(\frac{\tilde{A}(f_i)}{36.0}\right)^2, \tag{6.24}$$

since a value of $A(f_i) = 36$ meters corresponds to a RCS of approximately 1300 square meters, or 31 dB-sm, corresponding approximately to the largest RCS value in the 5 target library at HF frequencies.

Figure 54 demonstrates improvement in classification performance for the relative phase channel over the non-coherent channel, however the increase in performance is less than that shown in Figure 51. Figures 55 and 56 show little or no improvement in classification performance of the relative phase channel over the non-coherent channel when utilizing the ${}_2d_{u,k}$ measure. Therefore our choices of $R(\tilde{A}(f_i))$ are far from ideal.

Overall this study has indicated that for small frequency bands, the relative phase channel described may improve performance over the non-coherent channel if the relative phase estimates are used as described. However, at larger frequency bands, the use of relative phase information proposed appears only to deteriorate performance. This may be due to several factors. First, the development of the use of the relative phase features has been based on intuitive judgement, and not proven estimation theory. Therefore the use of the phase features while making logical sense, may be far from the optimum use of relative phase as a classification feature.

An alternate method of utilizing relative phase information involves estimation of the unknown targets phase. Given a set of coherent bsckscatter amplitudes one may use the Cross Correlation Algorithm to provide a maximum likelihood estimate of the unknown target phase, thereby minimizing the conditional risk for a uniform cost function. The phase estimate may then be used to aid in classifying the target. Research has shown that use of the Cross Correlation Algorithm will consistently improve classification performance over use of amplitude only estimates [8].

It is critical to note these results are highly dependent on the noise model used in the study. Given a different noise model where the noise corrupting the amplitude and phase features is independent, different results would be expected.

Parameter Under Observation: ρ
Channel Model: Relative Phase Channel
Azimuth angle: 45
Start Frequency: 8.0 MHz
Stop Frequency: 10.0 MHz
Number of Frequencies: 10
W Distance Measure: ${}_1d_{u,k}$
ρ : Key

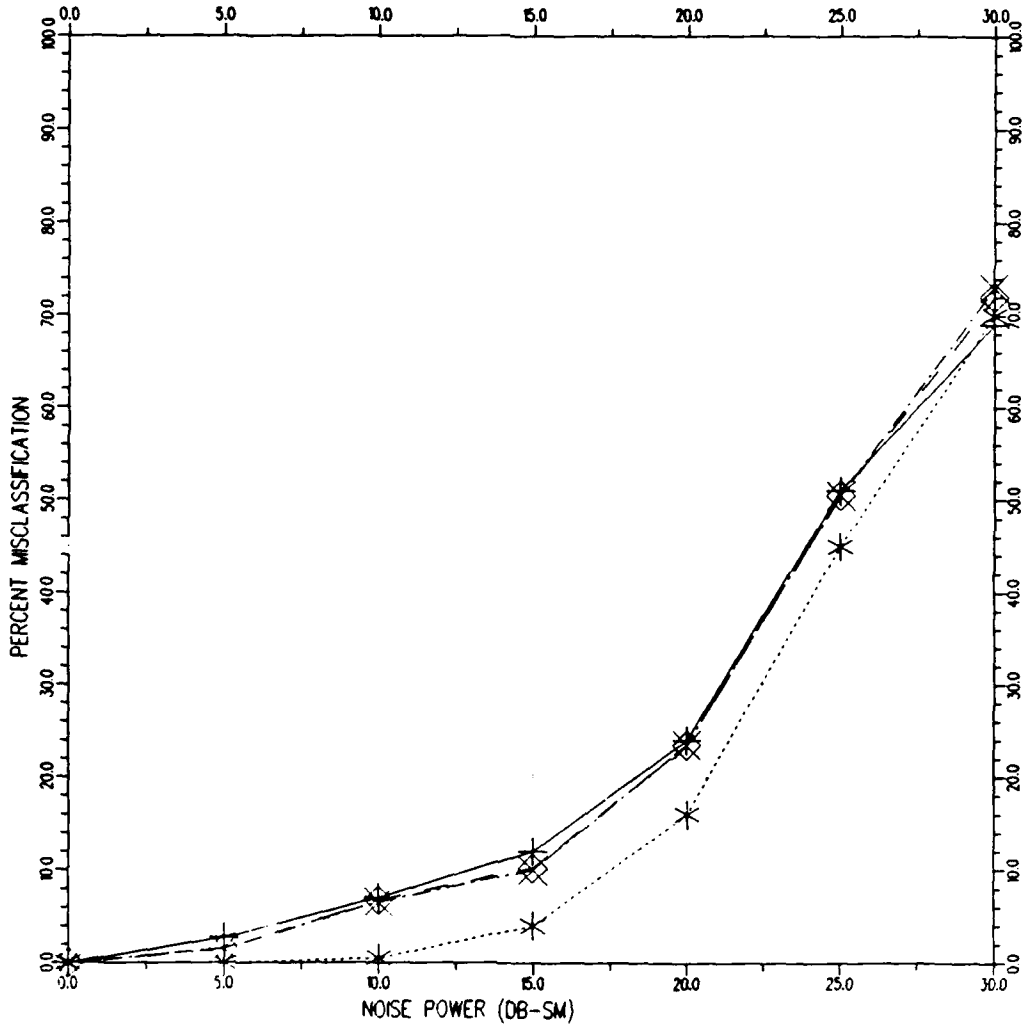

_____ Non-Coherent Channel
- - - - $\rho = 1.0$
— - — $\rho = 0.1$
— — — $\rho = 0.05$

Figure 51: W feature 2 MHz band weighting study.

Parameter Under Observation: ρ
Channel Model: Relative Phase Channel
Azimuth angle: 45
Start Frequency: 20.0 MHz
Stop Frequency: 24.0 MHz
Number of Frequencies: 10
W Distance Measure: ${}_1d_{u,k}$
ρ : Key

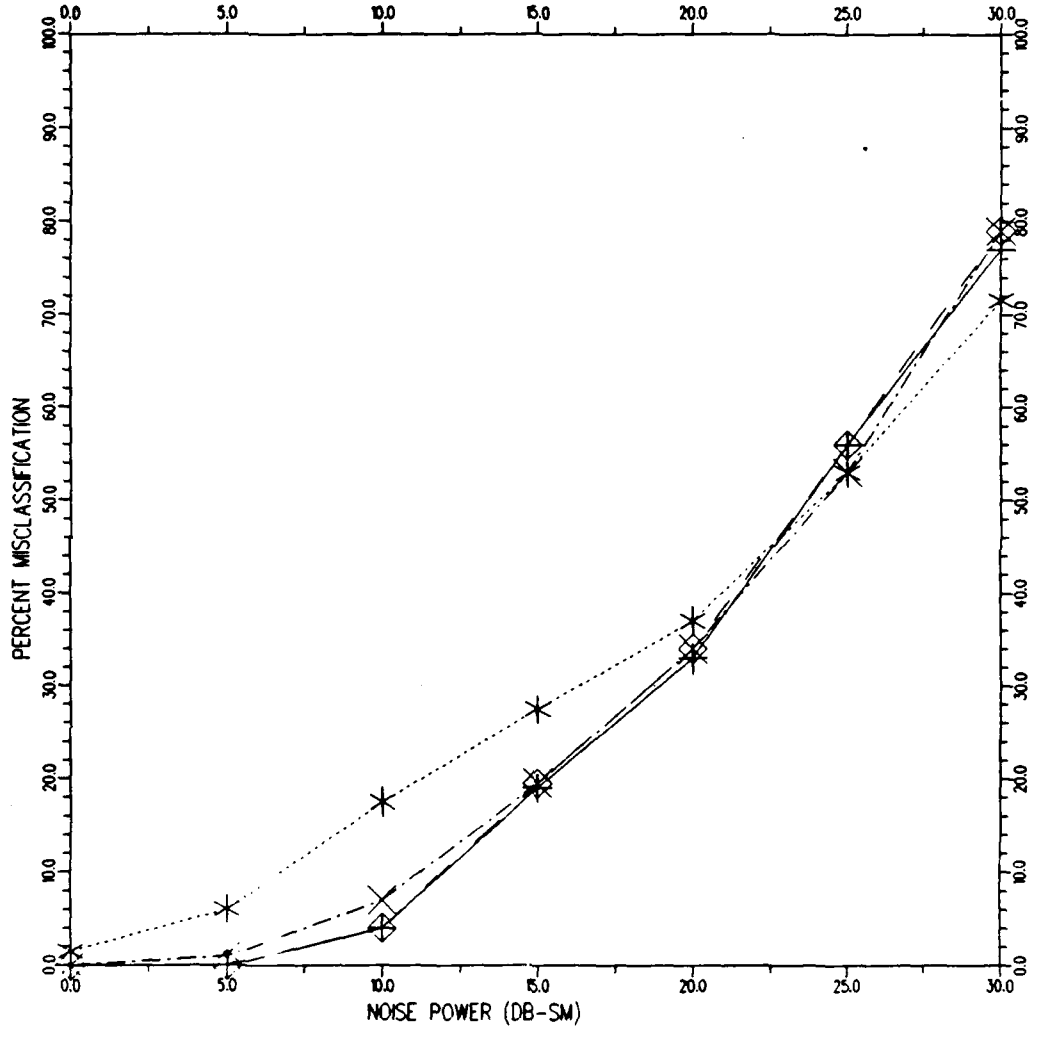

Non-Coherent Channel
$\rho = 1.0$
$\rho = 0.1$
$\rho = 0.05$

Figure 52: W feature high 4 MHz band weighting study.

Parameter Under Observation: ρ
Channel Model: Relative Phase Channel
Azimuth angle: 30
Start Frequency: 8.0 MHz
Stop Frequency: 10.0 MHz
Number of Frequencies: 5
W Distance Measure: ${}_1d_{u,k}$
ρ : Key

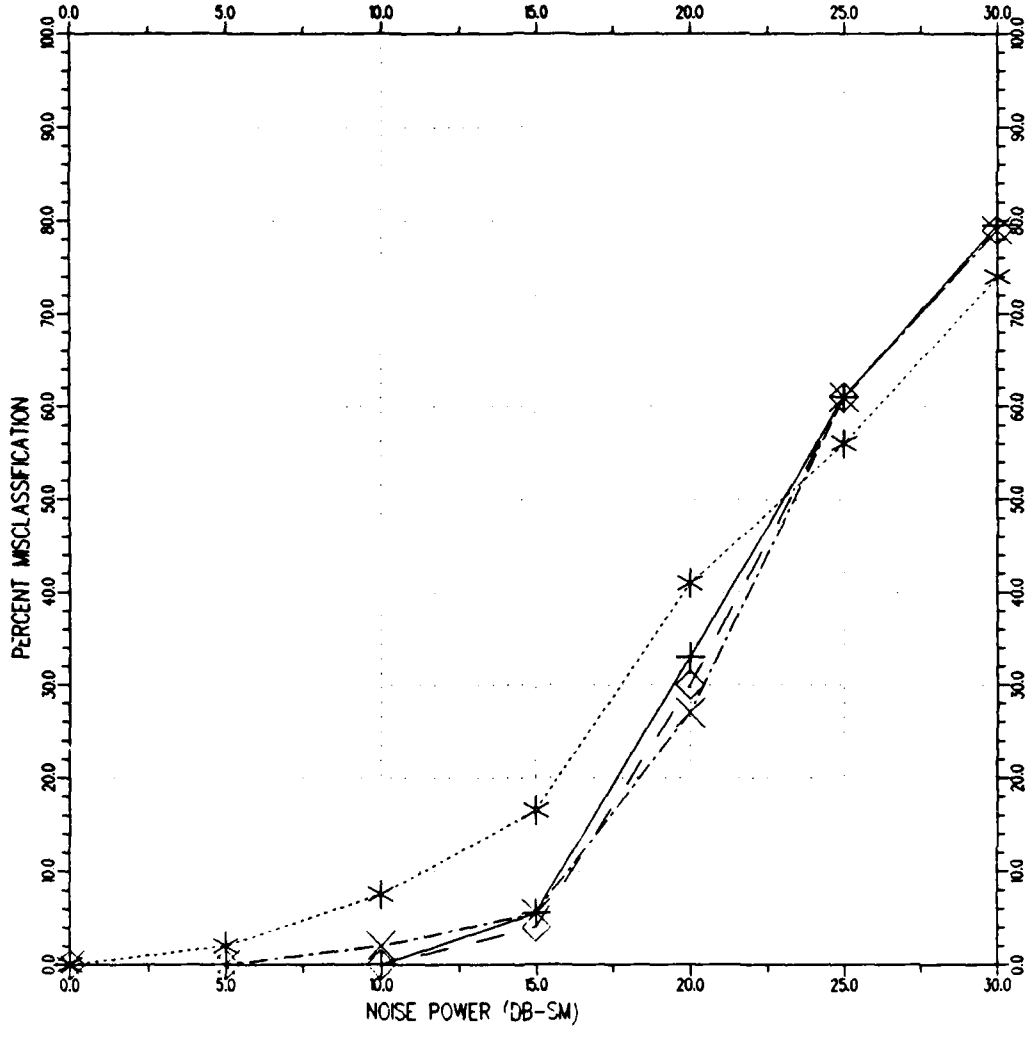

Figure 53: W feature low 4 MHz band weighting study.

Parameter Under Observation: Individual Distance Weightings
Channel Model: Relative Phase Channel
Azimuth angle: 45
Start Frequency: 8.0 MHz
Stop Frequency: 10.0 MHz
Number of Frequencies: 10
W Distance Measure: $_2d_{u,k}$
ρ : 0.5

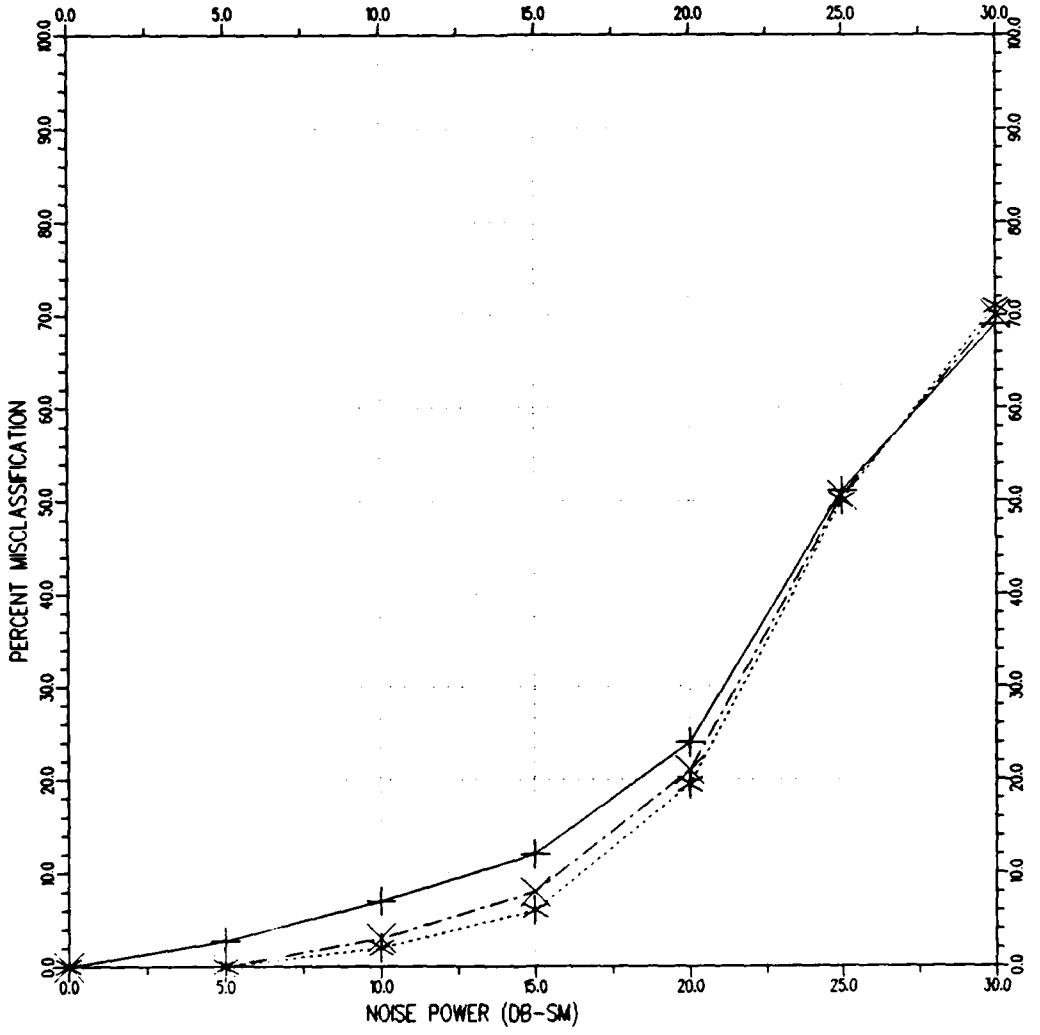

_____ Non-Coherent Channel
- - - - $R(A(f_i)) = \frac{A(f_i)}{36}$
— - — $R(A(f_i)) = (\frac{A(f_i)}{36})^2$

Figure 54: W feature 2 MHz band distance weight study.

Parameter Under Observation: Individual Distance Weightings
Channel Model: Relative Phase Channel
Azimuth angle: 45
Start Frequency: 20.0 MHz
Stop Frequency: 24.0 MHz
Number of Frequencies: 10
W Distance Measure: ${}_2d_{u,k}$
ρ : 0.5

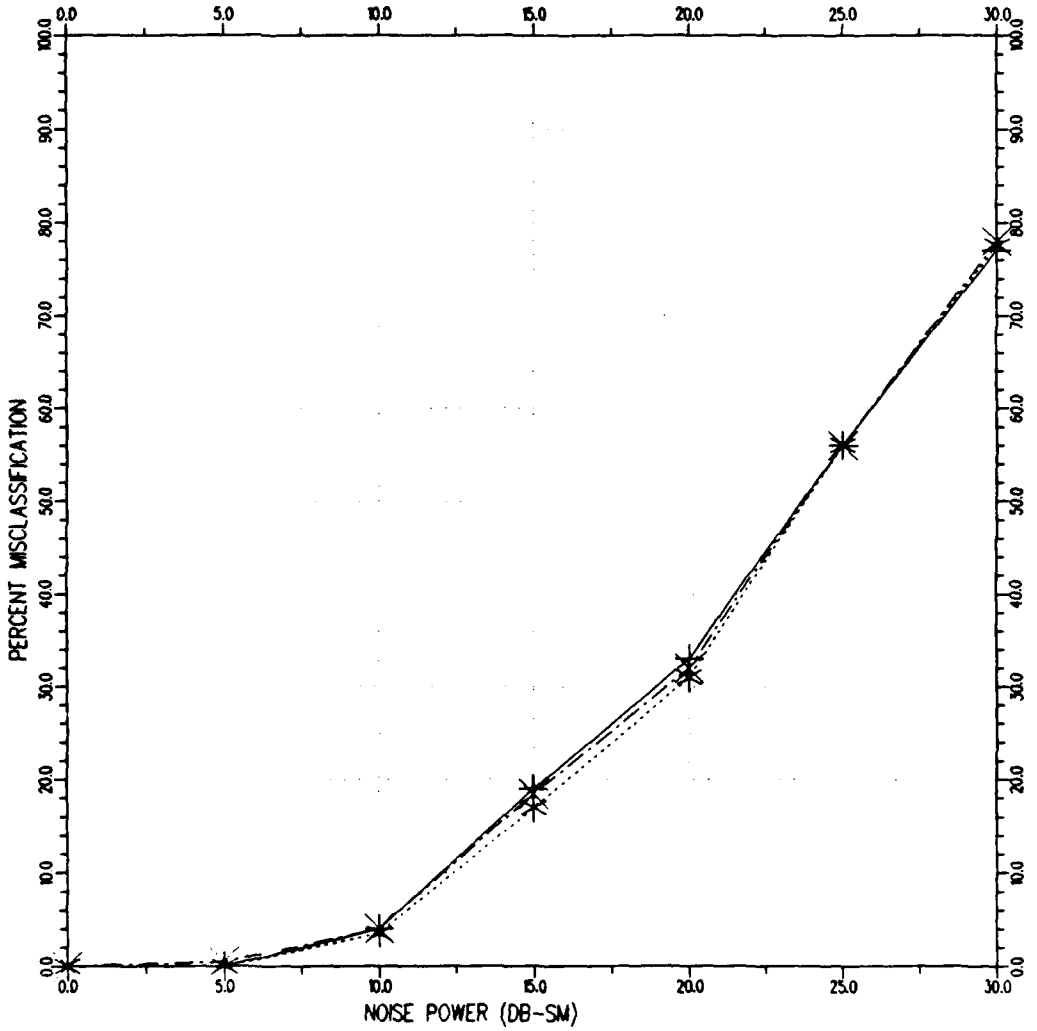

_____ Non-Coherent Channel
- - - - $R(A(f_i)) = \frac{A(f_i)}{36}$
— - — $R(A(f_i)) = (\frac{A(f_i)}{36})^2$

Figure 55: W feature high 4 MHz band distance weight study.

Parameter Under Observation: Individual Distance Weightings
Channel Model: Relative Phase Channel
Azimuth angle: 30
Start Frequency: 6.0 MHz
Stop Frequency: 12.0 MHz
Number of Frequencies: 15
W Distance Measure: ${}_2d_{u,k}$
ρ : 0.5

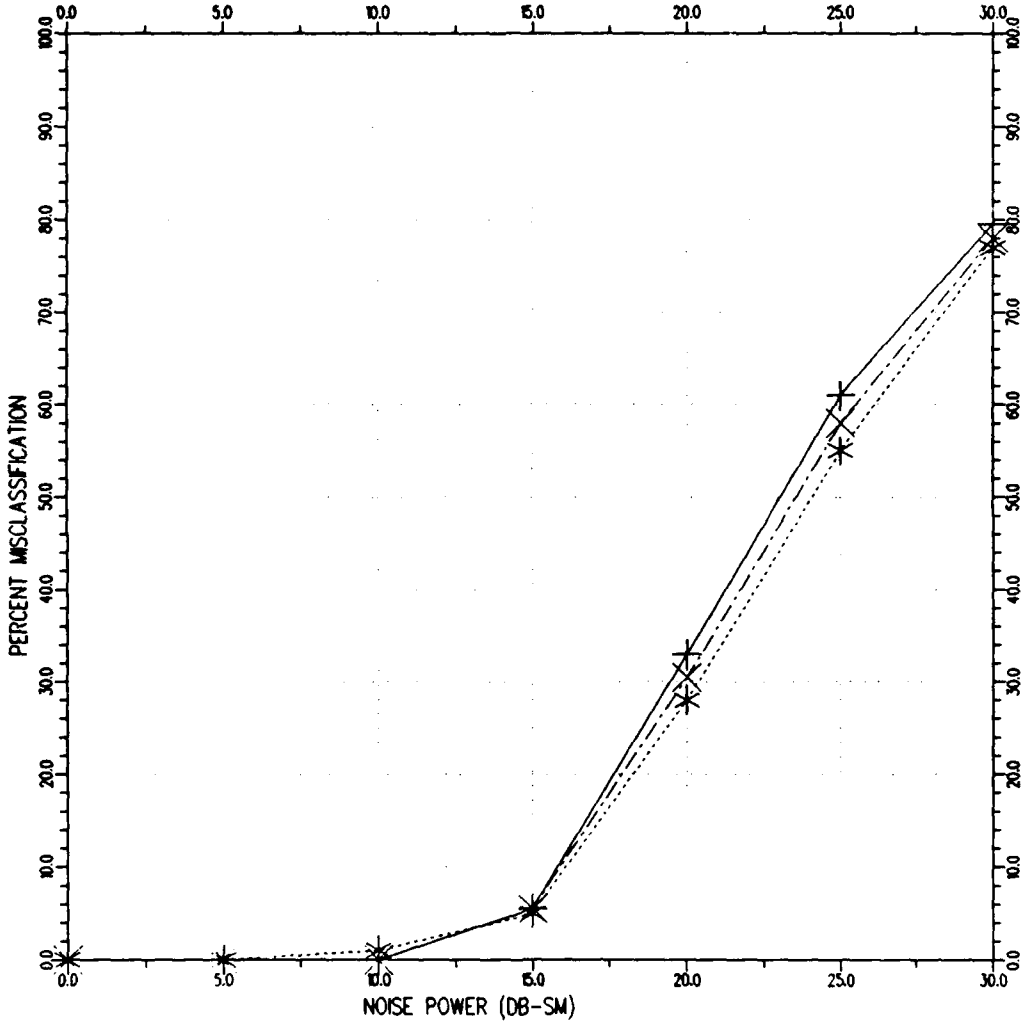

_____ Non-Coherent Channel
- - - - - $R(A(f_i)) = \frac{A(f_i)}{36}$
— - — $R(A(f_i)) = (\frac{A(f_i)}{36})^2$

Figure 56: W feature low 4 MHz band distance weight study.

CHAPTER VII

FADING CHANNEL MODEL STUDY

7.1 Implementation

Multipath propagation is a common occurence in ionospherically propagated signals. In the radar problem, multipath phenomena generally results in the received signal being the result of the two or more signals adding in and out of phase at the receive antenna. One signal, which travels the expected path, may be considered deterministic in nature. The other signals, which travel undesired paths, may best be described as a stochastic process since the paths they take through the ionosphere may be considered less stable. As a result, the propagation path may best be described as a fading channel [27].

A fading model representing the estimation of features from multipath propagated signals as shown in Eq. (7.1) was implemented in the RSSE program [28].

$$A_u^F(f_i)e^{j\theta_u^F(f_i)} = \alpha A_T(f_i)e^{j\theta_T(f_i)} + (1-\alpha^2)^{\frac{1}{2}} A_T(f_i)Z(f_i)e^{j\theta_z(i)} \qquad i = 1, N \quad (7.1)$$

where $\alpha A_T(f_i)e^{j\theta_T(f_i)}$ is the deterministic component, $(1-\alpha^2)^{\frac{1}{2}} A_T(f_i)Z(f_i)e^{j\theta Z(i)}$ denotes the faded component, and α is the weight of the deterministic component. The parameter $A_T(f_i)e^{j\theta(f_i)}$ is the high accuracy complex backscatter component of target T at frequency f_i, $Z(i)$ is the random amplitude of faded component taken from a correlated or uncorrelated random process, and $\theta^Z(i)$ is the random phase of faded component taken from a correlated or uncorrelated random process.

Construction of the simulated feature vector is shown in Figure 57. The complex backscattered data are simply scaled by the chosen variable α, where $0 < \alpha < 1$, to construct the deterministic component. Construction of the faded components are more complex. The magnitude of the high accuracy backscattered data is first scaled by $(1 - \alpha^2)^{\frac{1}{2}}$ to ensure the vector resulting from the sum of the deterministic and faded components has a total power equal to the test set vector used. Next, the random samples $Z(i)$ are constructed by first generating samples from a white zero-mean Gaussian random process with a variance (σ^2) of one. These samples are then passed through a filter with an impulse response $h(i)$ where i =0 to $N - 1$. The output process has an autocorrelation function given by:

$$R_Z(k) = \sum_{i=0}^{N-1} h(i)h(k+i), \qquad -N+1 \leq k \leq N-1 \tag{7.2}$$

as described in [9].

The total power in the process $\{ Z(i) \}$ is then given by:

$$R_Z(0) = \sum_{i=0}^{N-1} (h(i))^2 \tag{7.3}$$

Therefore, by selecting filter values $h(i)$ such that the total power of the process $\{ Z(i) \}$ is one, the resulting power of the faded channel vector will be equivalent to the power of the test vector used. The filter values used were constructed from the filter function by:

$$h(i) = \frac{\epsilon^{-\Psi i}}{\left[\sum_{i=1}^{N} \epsilon^{-2\Psi i}\right]^{\frac{1}{2}}} \qquad i = 0, ..., N-1 \tag{7.4}$$

where $h(i)$ is the filter function, and Ψ is the correlation coefficient selected by user the so that $R_Z(0)$ equals 1 independent of the value N selected. By increasing Ψ from zero ($\{ Z(i) \}$ highly correlated) to infinity ($\{ Z(i) \}$ uncorrelated) the

operator simulates various degrees of correlation between the faded components of a given measurement vector.

The faded components are then weighted by the samples from the random process $\{ Z(i) \}$. Phase is assigned to each random faded amplitude by taking samples from an i.i.d. process whose random variables are uniformly distributed over the interval $-\pi$ to $+\pi$. The resulting complex deterministic components and complex faded components are then summed, producing the faded channel vector. Additive white Gaussian noise is then added coherently to the faded channel vector as described earlier. The simulated vector represents the output of a faded channel with additive Gaussian noise. By applying the techniques described in sections 4.3.1 through 4.3.3 to the faded channel vector, variations of the faded channel model such as loss of phase information or the addition of an unknown multiplicitive component may be synthesized. As a result, three faded channel models with characteristics analogous to those described in 4.3.1 through 4.3.3 and titled channel 1F, channel 2F, and channel 3F respectively were investigated.

Three studies were conducted utilizing the faded channel model. First the relationship between the deterministic component weight (α) and the classification performance for the three channels was investigated. Next the correlation coefficient Ψ was varied while maintaining a constant deterministic component weight. Finally, direct comparison between the three faded channel models was conducted.

7.2 Deterministic Weighting Study

Figure 58 shows the the degradation of classification of channel F1 as α is decreased. Note that significant degradation of performance is only found at α=0.5. Figure 59 shows a significant degradation of classification performance at $\alpha = 0.75$ and $\alpha = 0.5$ for channel F2. Classification using channel F3 demonstrates an

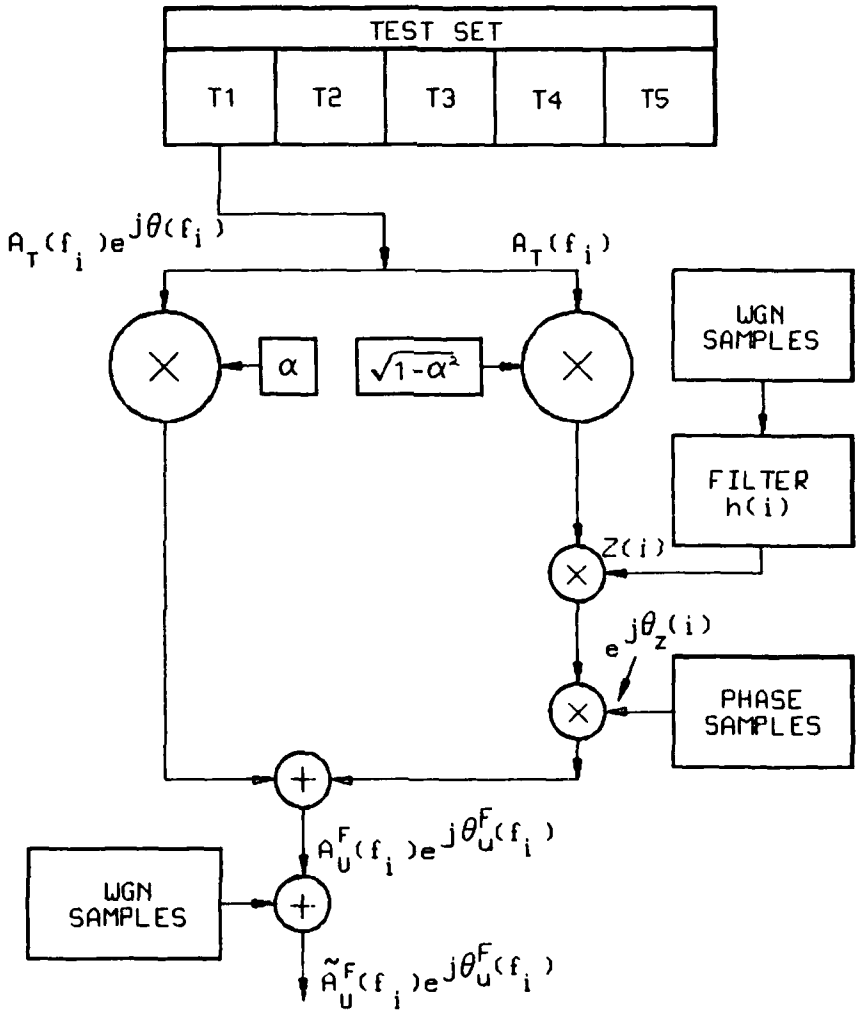

Figure 57: Faded channel implementation block diagram.

approximate 10 percent degradation in performance as α is decreased from 1.0 to 0.9, and from 0.9 to 0.75, as indicated in Figure 60. Thus, these figures indicate that the performance of channel F2 may be severely degraded by a low deterministic weight.

Figures 61, 62, and 63 are similar to the previous three figures with the exception of a smaller frequency band of 2 MHz. More significant degradation of performance for channel F1 is noted at α=0.75 and α=0.5 as noted in Figure 61, which was expected with the smaller frequency band. Figure 62 demonstrates a decrease in performance of 25 % for a given noise power as α is varied from 1.0 to 0.9. Likewise, Figure 63 shows the same large decrease in the ability using channel F3 as the deterministic weight is decreased.

Overall, the performance tends to degrade by a much larger amount for the same changes in α at the 2 MHz band. Therefore the deterministic weight becomes an increasingly important characteristic of the faded channel when the frequency band decreases.

A third set of Figures (64, 65, and 66) were constructed using one-half the number of data points over the same 8.0 MHz to 10.0 MHz band. Further decreases in classification performance with decreased deterministic weighting are expressed for all three channels as expected.

Parameter Under Observation: Deterministic Weight
Channel Model: Coherent Faded Channel
Azimuth angle: 0
Start Frequency: 8.0 MHz
Stop Frequency: 12.0 MHz
Number of Frequencies: 10
Deterministic Weight: Key
Correlation Coefficient: 0.5

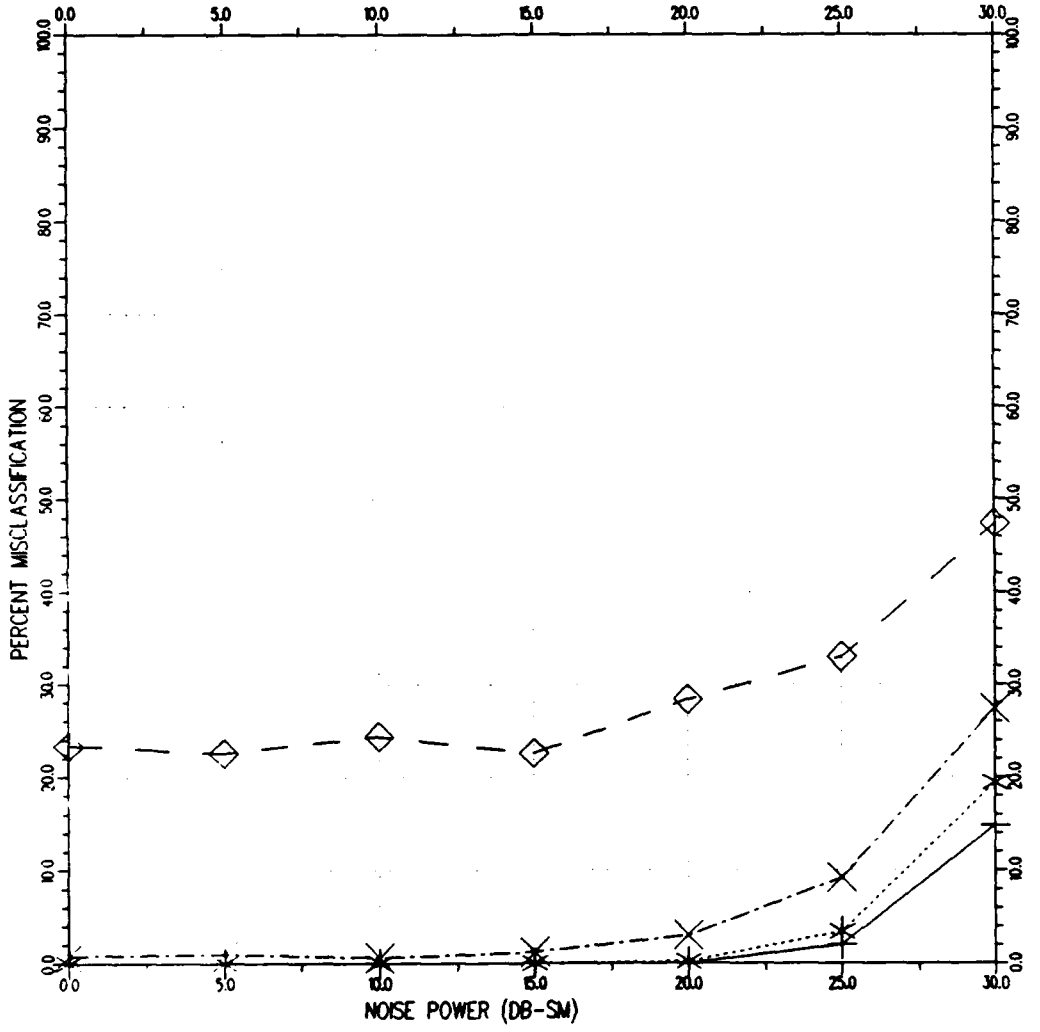

Figure 58: Weighting study for coherent 4 MHz band faded channel.

Parameter Under Observation: Deterministic Weight
Channel Model: Non-Coherent Faded Channel
Azimuth angle: 0
Start Frequency: 8.0 MHz
Stop Frequency: 12.0 MHz
Number of Frequencies: 10
Deterministic Weight: Key
Correlation Coefficient: 0.5

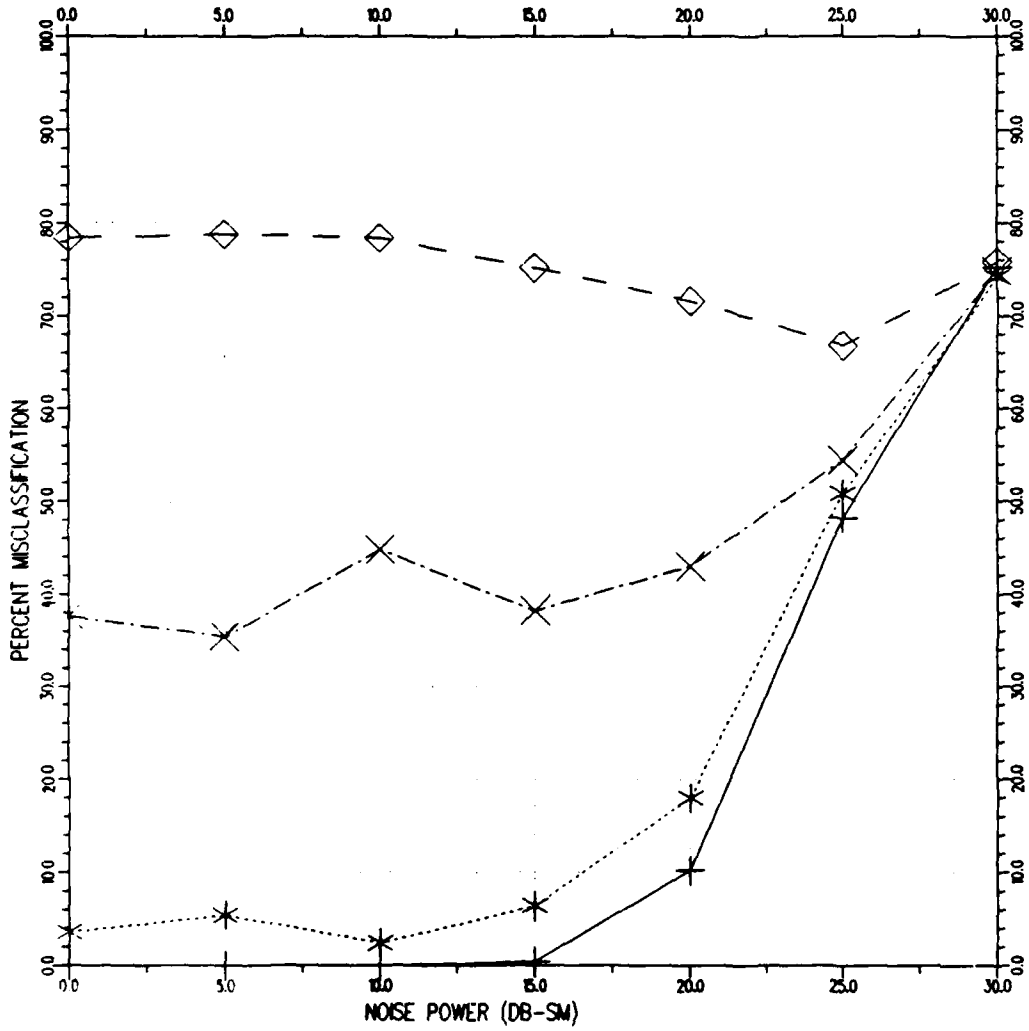

Figure 59: Weighting study for non-coherent 4 MHz band faded channel

Parameter Under Observation: Deterministic Weight
Channel Model: Multiplicitive Component Faded Channel
Azimuth angle: 0
Start Frequency: 8.0 MHz
Stop Frequency: 12.0 MHz
Number of Frequencies: 10
Deterministic Weight: Key
Correlation Coefficient: 0.5

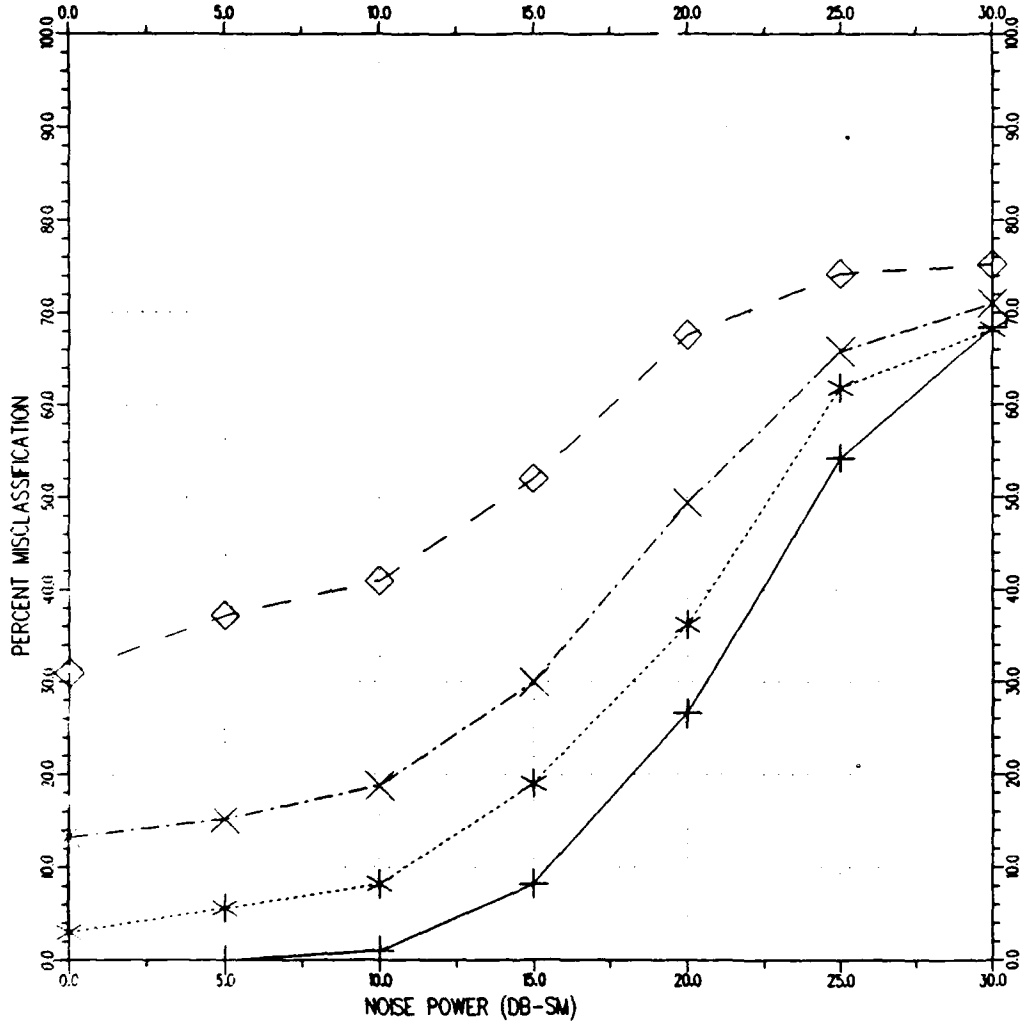

Figure 60: Weighting study for multiplicitive 4 MHz band faded channel.

Parameter Under Observation: Deterministic Weight
Channel Model: Coherent Faded Channel
Azimuth angle: 45
Start Frequency: 8.0 MHz
Stop Frequency: 10.0 MHz
Number of Frequencies: 10
Deterministic Weight: Key
Correlation Coefficient: 0.5

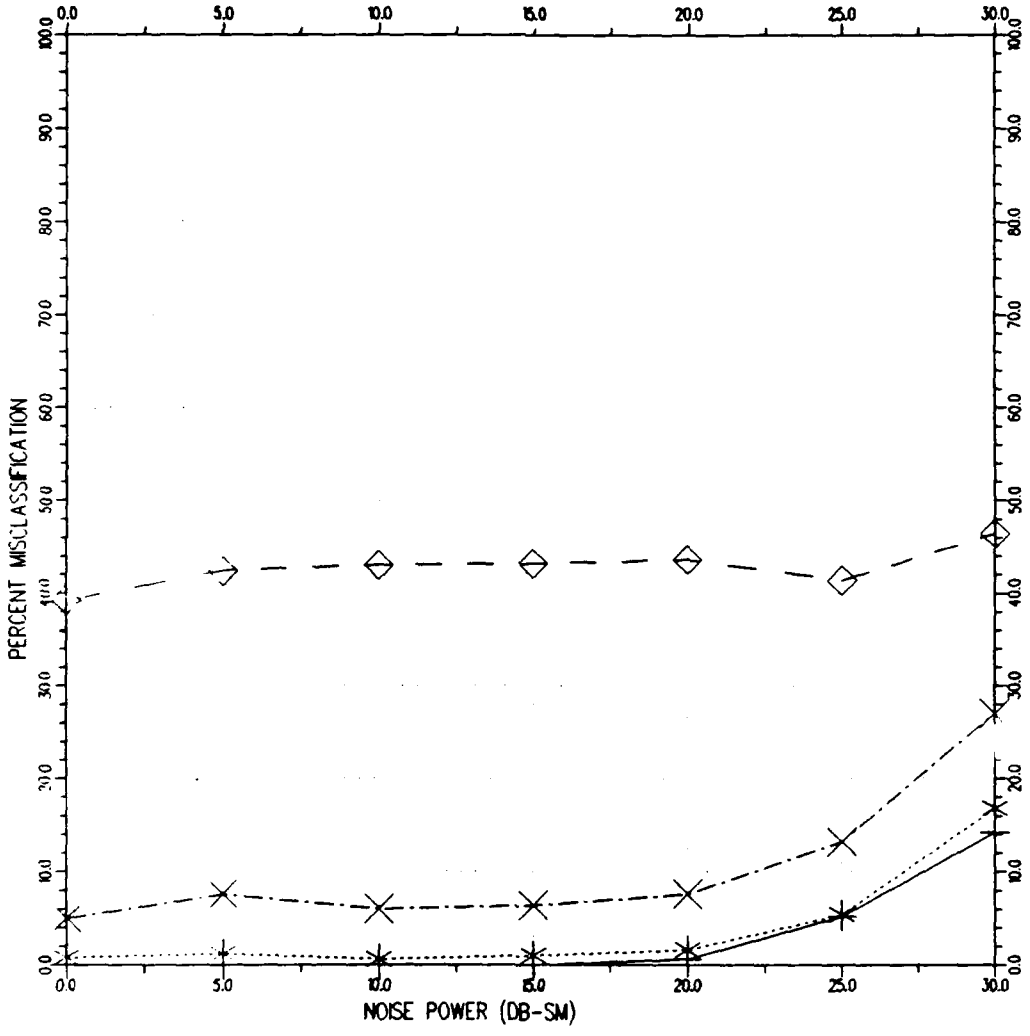

Figure 61: Weighting study for coherent 10 feature - 2 MHz band faded channel.

Parameter Under Observation: Deterministic Weight
Channel Model: Non-Coherent Faded Channel
Azimuth angle: 45
Start Frequency: 8.0 MHz
Stop Frequency: 10.0 MHz
Number of Frequencies: 10
Deterministic Weight: Key
Correlation Coefficient: 0.5

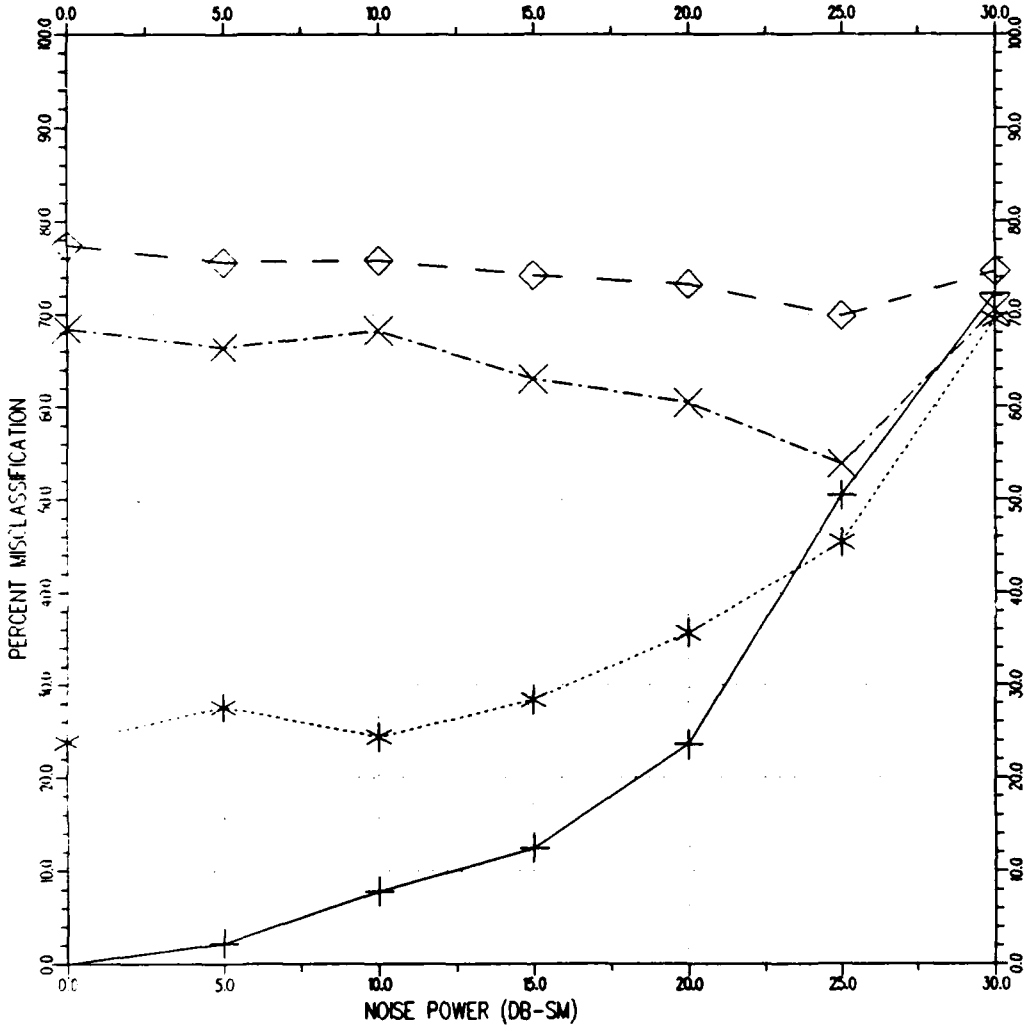

Figure 62: Weighting study for non-coherent 10 feature - 2 MHz band faded channel.

Parameter Under Observation: Deterministic Weight
Channel Model: Multiplicitive Component Faded Channel
Azimuth angle: 45
Start Frequency: 8.0 MHz
Stop Frequency: 10.0 MHz
Number of Frequencies: 10
Deterministic Weight: Key
Correlation Coefficient: 0.5

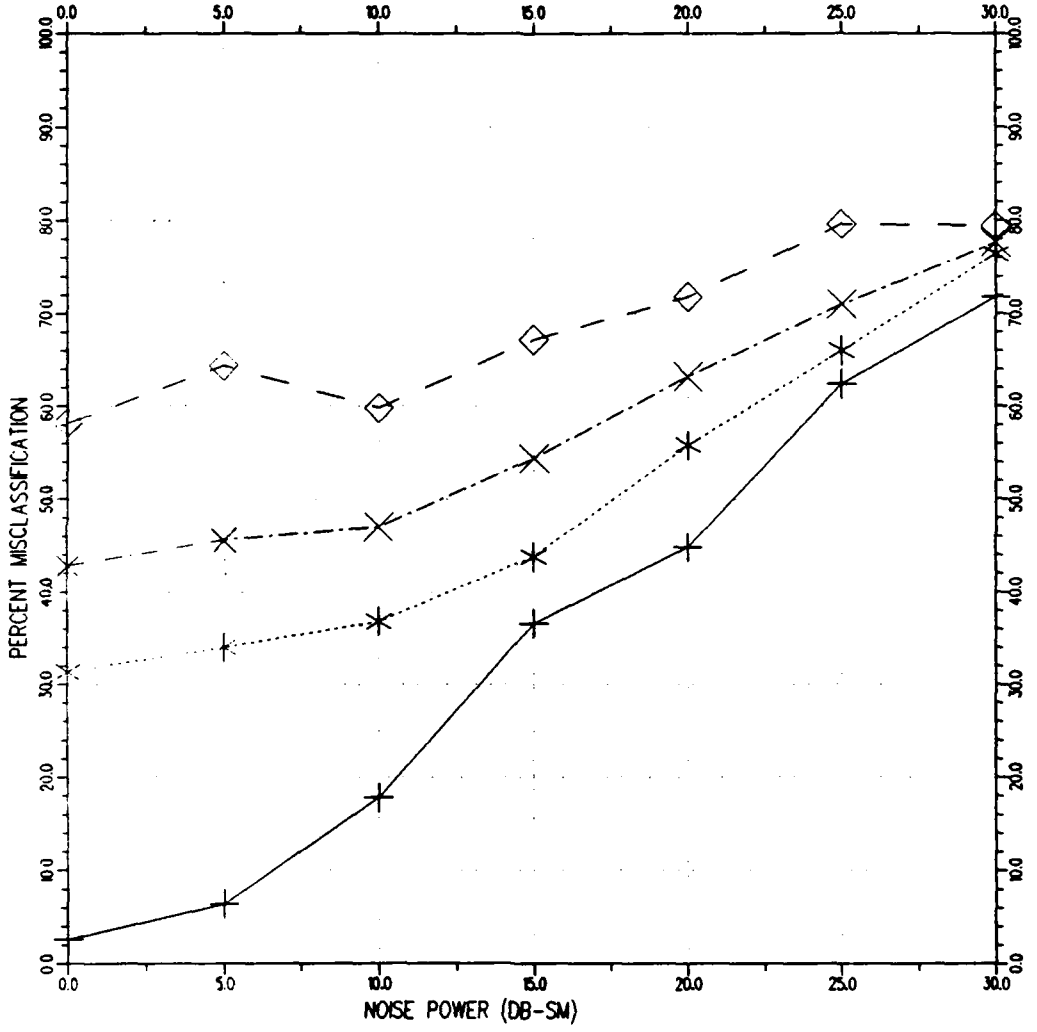

——— $\alpha = 1.0$
- - - - $\alpha = 0.9$
— - — $\alpha = 0.75$
— — — $\alpha = 0.5$

Figure 63: Weighting study for multiplicitive 10 feature – 2 MHz band faded channel.

Parameter Under Observation: Deterministic Weight
Channel Model: Coherent Faded Channel
Azimuth angle: 45
Start Frequency: 8.0 MHz
Stop Frequency: 10.0 MHz
Number of Frequencies: 5
Deterministic Weight: Key
Correlation Coefficient: 0.5

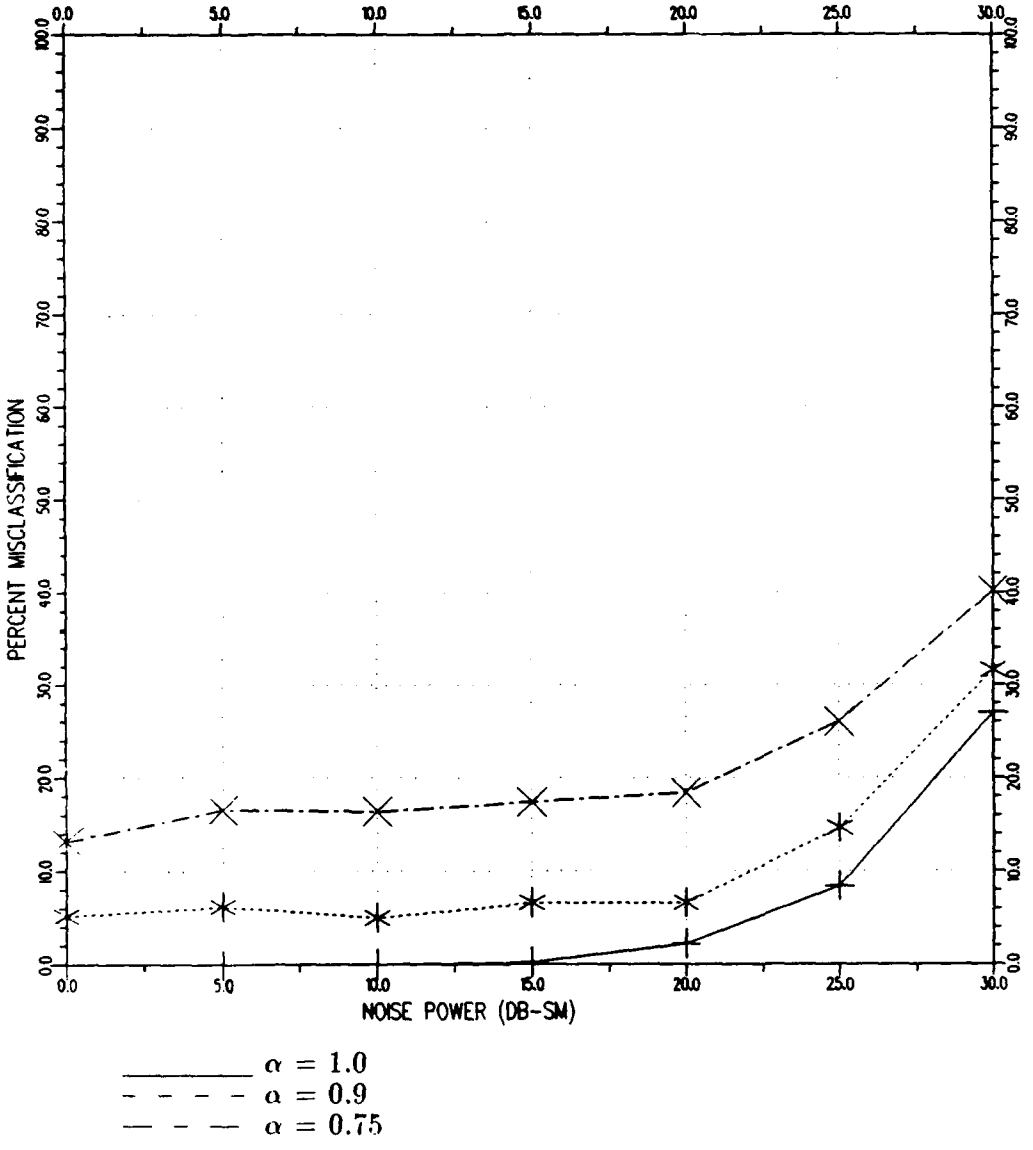

Figure 64: Weighting study for coherent 5 feature – 2 MHz band faded channel.

Parameter Under Observation: Deterministic Weight
Channel Model: Non-Coherent Faded Channel
Azimuth angle: 45
Start Frequency: 8.0 MHz
Stop Frequency: 10.0 MHz
Number of Frequencies: 5
Deterministic Weight: Key
Correlation Coefficient: 0.5

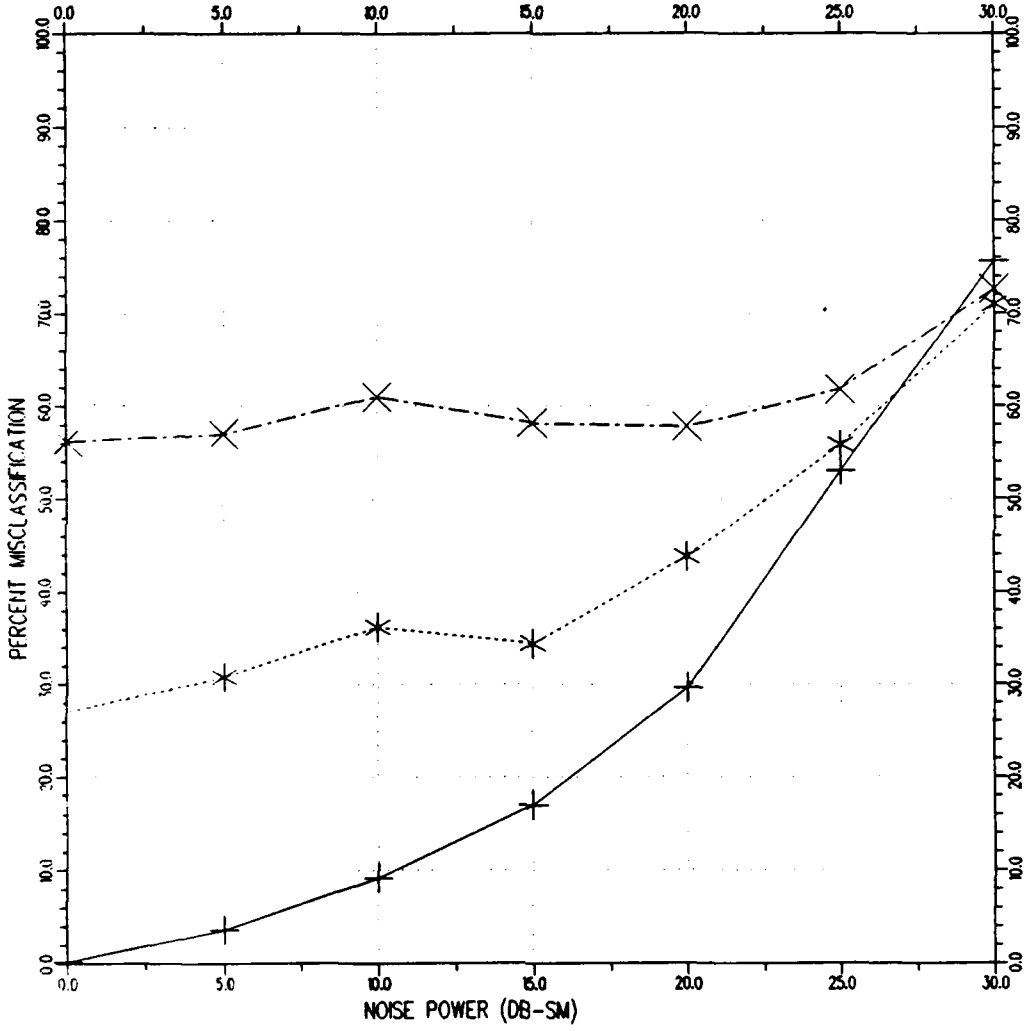

Figure 65: Weighting study for non-coherent 5 feature – 2 MHz band faded channel.

Parameter Under Observation: Deterministic Weight
Channel Model: Multiplicitive Component Faded Channel
Azimuth angle: 45
Start Frequency: 8.0 MHz
Stop Frequency: 10.0 MHz
Number of Frequencies: 5
Deterministic Weight: Key
Correlation Coefficient: 0.5

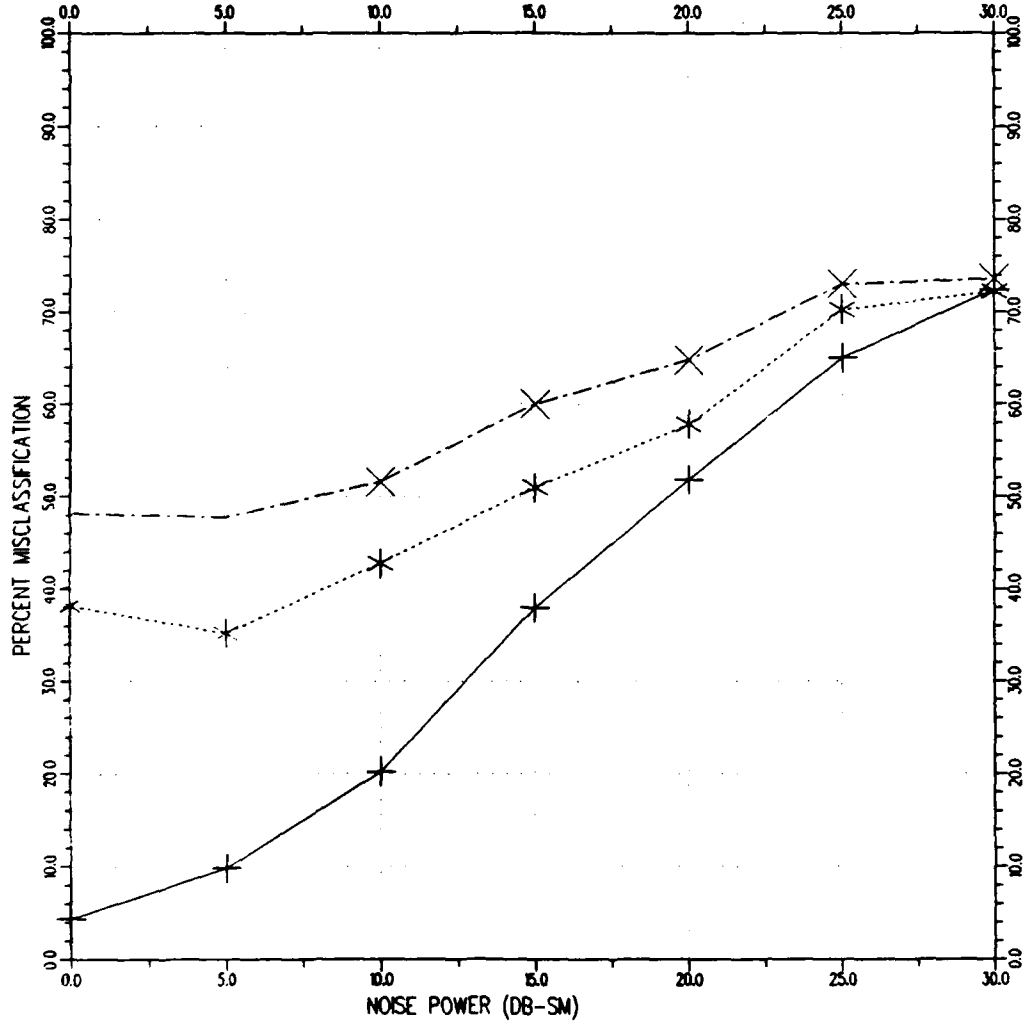

——— $\alpha = 1.0$
– – – – $\alpha = 0.9$
— – — $\alpha = 0.75$

Figure 66: Weighting study for multiplicitive 5 feature - 2 MHz band faded channel.

7.3 Correlation Study

Figures 67, 68, and 69 demonstrate the effect of the correlation of the faded components on the performance of the three faded channels over a 2 MHz frequency band. In this band, channel F1 does not demonstrate a decrease in classification performance with increasing correlation. Channel F2 exhibits a 4% decrease in performance when faded components become highly correlated as shown in Figure 68. Channel F3 again shows major improvement as a classification feature when the correlation increases as displayed in Figure 69.

Figure 70 demonstrates the decrease in classification performance of channel F1 resulting from an increased correlation of the faded components. In Figure 71, channel F2 exhibits a significant change in classification performance at Ψ=0.1, however the overall performance is quite poor in all cases due to the low weighting ($\alpha = 0.75$) of the deterministic component. Figure 72 shows the increase in classification performance of channel 3 as the faded components become more correlated. The significant gain of 3 to 5 dB-sm in noise power immunity indicates the correlation coefficient may be an important parameter in a faded channel which exhibits an unknown multiplicitive component.

Figures 67 through 72 indicate several relations between classification performance and correlation of faded components. Channel F1, which utilizes intrinsic phase information tends to show a slight decrease in performance with an increase in correlation. This may possibly due to the corrupted amplitude of the target appearing consistently smaller (or larger) at each frequency due to the correlation of the $Z(i)$ samples. As a result, the target may appear to be closer to a smaller (or larger) target in terms of the Nearest Neighbor Algorithm, and therefore be misclassified.

The tendency of channel F2 to increase performance as the faded components become uncorrelated backs up the previously developed theory. However, since channel F2 removes all phase information and passes only the noisy absolute amplitude backscatter components to the classifier, one may expect to see a greater decrease in performance with increasing correlation than channel 1. There is no strong indication of this behavior, however.

Channel F3 which adds the unknown multiplicitive component which must be removed as described in section 4.3.3 demonstrates a significant increase in performance with an increase in the correlation of the faded components. As reasoned earlier, highly correlated faded components tend to make the target look larger (or smaller) across the band. As a result, the average RCS of the unknown target will tend to be larger (or smaller). The process of normalizing the corrupt backscatter amplitudes to remove the unknown multiplicitive component also tends to remove the *average* contribution of the faded component. As a result, the normalized amplitude feature is more dependent on the deterministic component of the faded channel, resulting in better classification performance.

Parameter Under Observation: Correlation
Channel Model: Coherent Faded Channel
Azimuth angle: 45
Start Frequency: 8.0 MHz
Stop Frequency: 10.0 MHz
Number of Frequencies: 10
Deterministic Weight: 0.9
Correlation Coefficient: Key

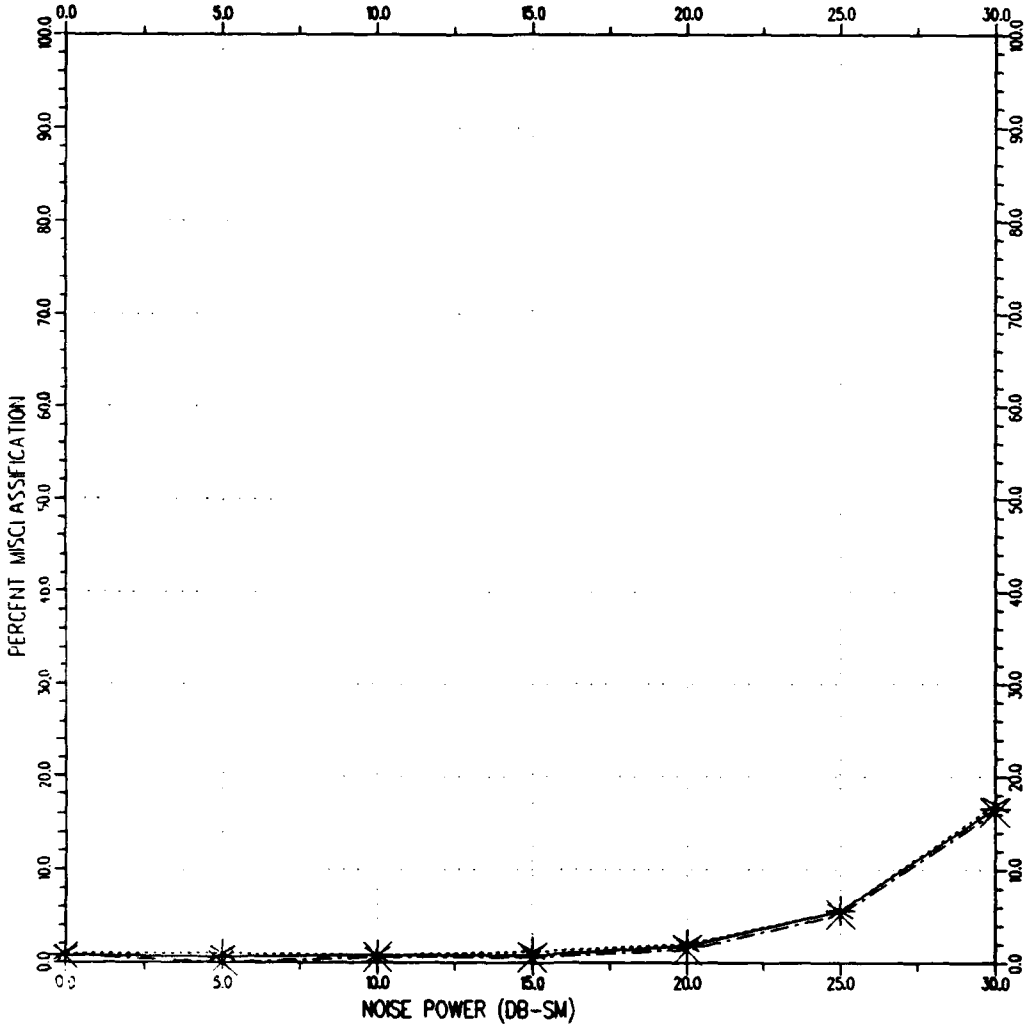

Figure 67: Correlation study for coherent 2 MHz band faded channel.

Parameter Under Observation: Correlation
Channel Model: Non-Coherent Faded Channel
Azimuth angle: 45
Start Frequency: 8.0 MHz
Stop Frequency: 10.0 MHz
Number of Frequencies: 10
Deterministic Weight: 0.9
Correlation Coefficient: Key

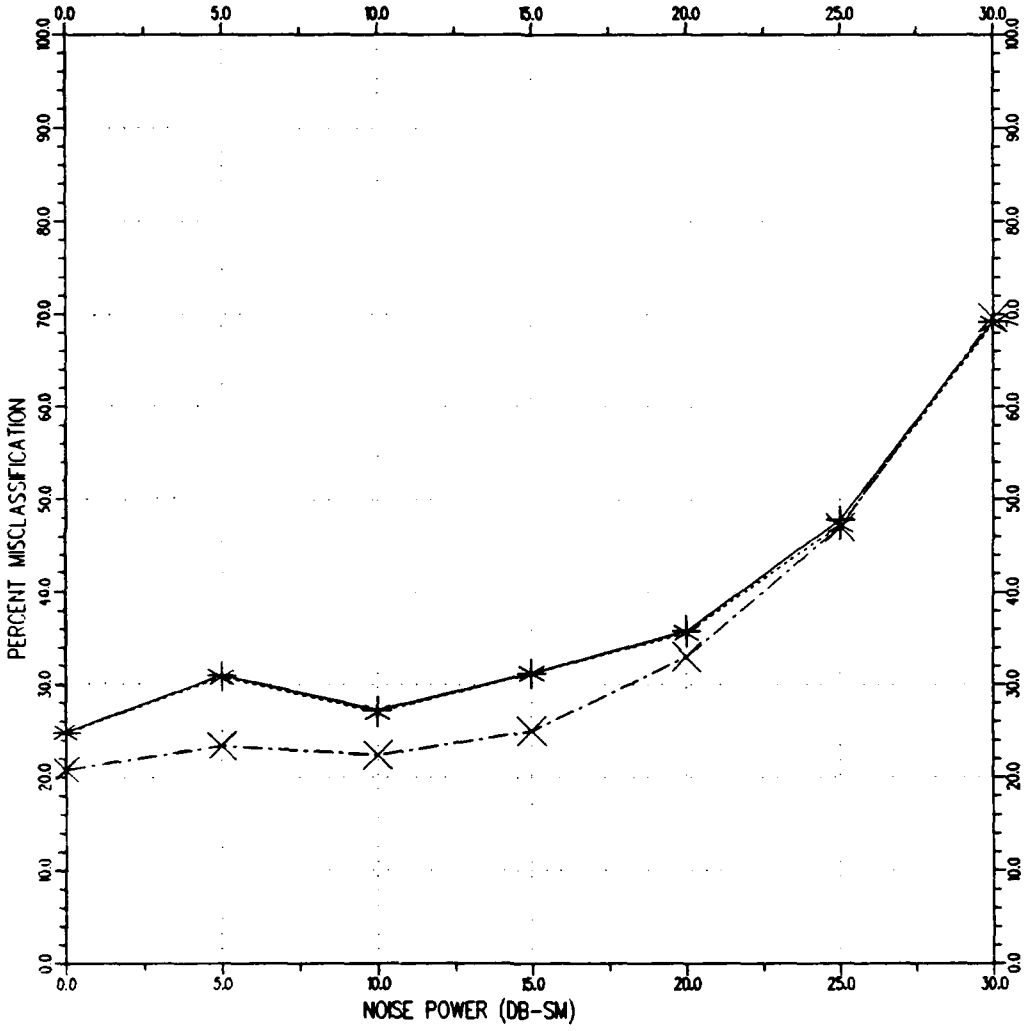

$\Psi = 0.001$
$\Psi = 0.05$
$\Psi = \infty$

Figure 68: Correlation study for non-coherent 2 MHz band faded channel.

Parameter Under Observation: Correlation
Channel Model: Multiplicitive Component Faded Channel
Azimuth angle: 45
Start Frequency: 8.0 MHz
Stop Frequency: 10.0 MHz
Number of Frequencies: 10
Deterministic Weight: 0.9
Correlation Coefficient: Key

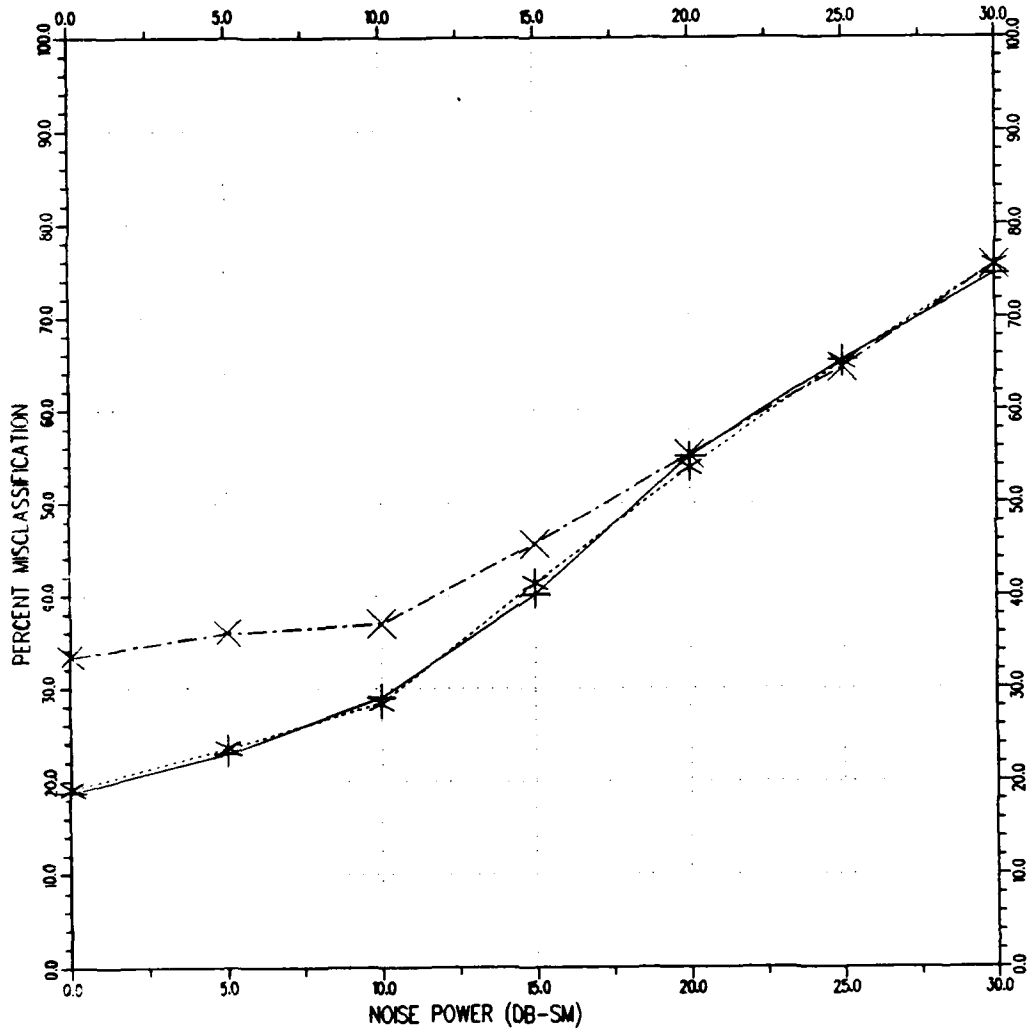

——— $\Psi = 0.001$
– – – – $\Psi = 0.05$
— – — $\Psi = \infty$

Figure 69: Correlation study for multiplicitive 2 MHz band faded channel.

Parameter Under Observation: Correlation
Channel Model: Coherent Faded Channel
Azimuth angle: 0
Start Frequency: 8.0 MHz
Stop Frequency: 12.0 MHz
Number of Frequencies: 10
Deterministic Weight: 0.75
Correlation Coefficient: Key

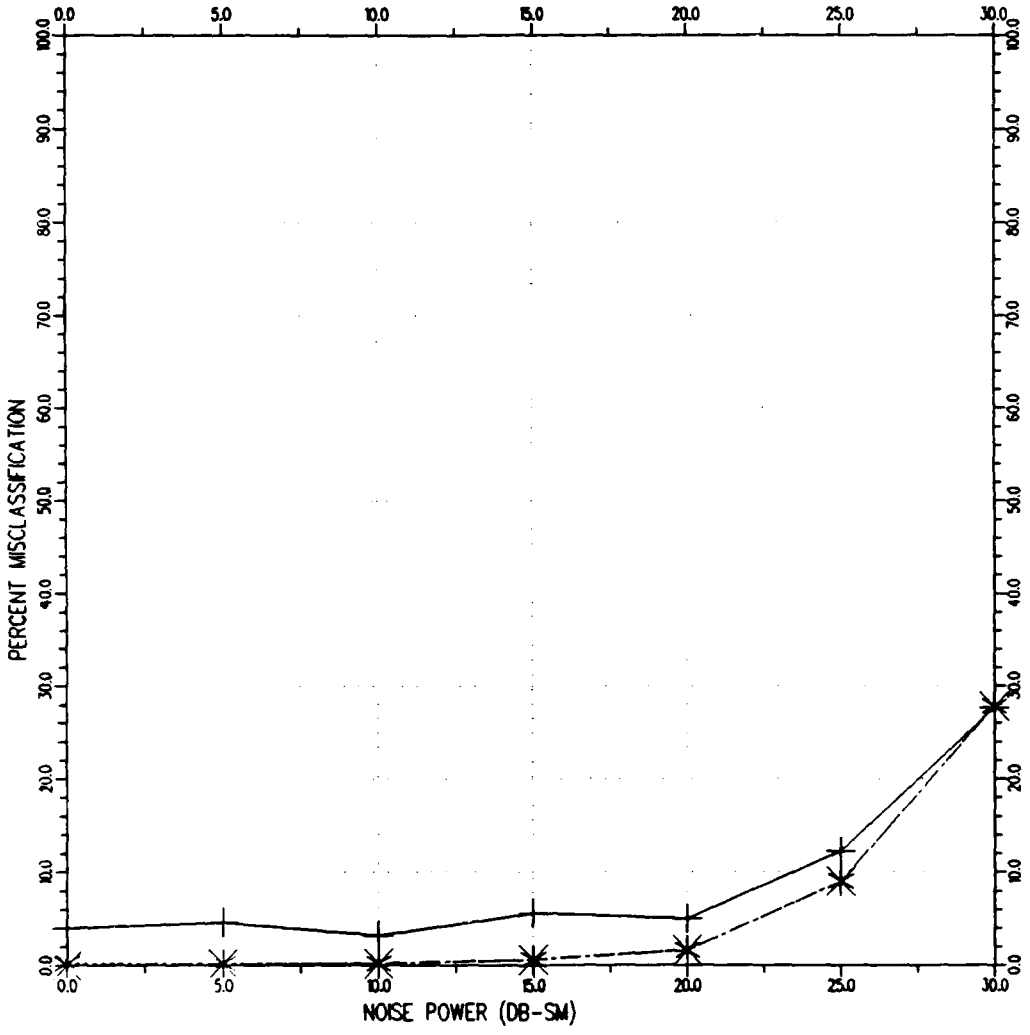

$\Psi = 0.1$
$\Psi = 2$
$\Psi = \infty$

Figure 70: Correlation study for coherent 4 MHz band faded channel.

Parameter Under Observation: Correlation
Channel Model: Non-Coherent Faded Channel
Azimuth angle: 0
Start Frequency: 8.0 MHz
Stop Frequency: 12.0 MHz
Number of Frequencies: 10
Deterministic Weight: 0.75
Correlation Coefficient: Key

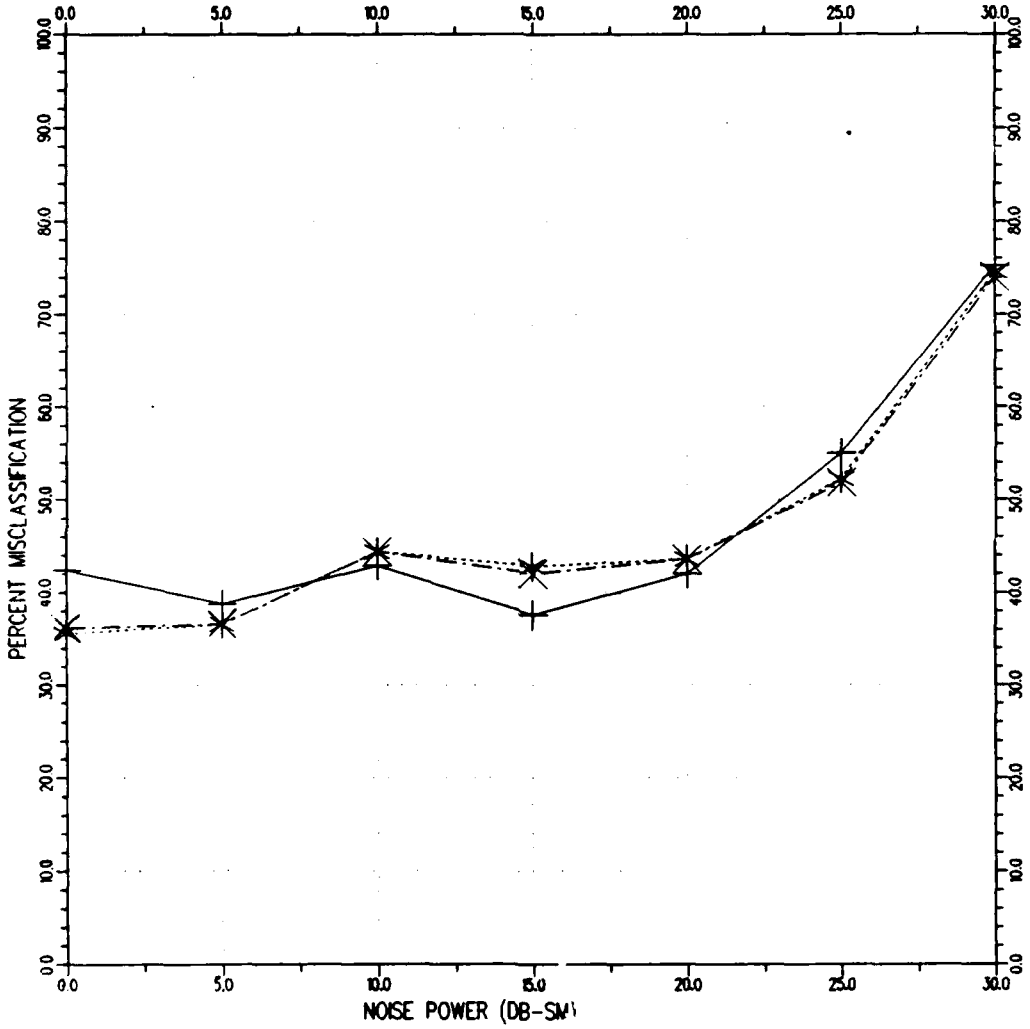

Figure 71: Correlation study for non-coherent 4 MHz band faded channel.

Parameter Under Observation: Correlation
Channel Model: Multiplicitive Component Faded Channel
Azimuth angle: 0
Start Frequency: 8.0 MHz
Stop Frequency: 12.0 MHz
Number of Frequencies: 10
Deterministic Weight: 0.75
Correlation Coefficient: Key

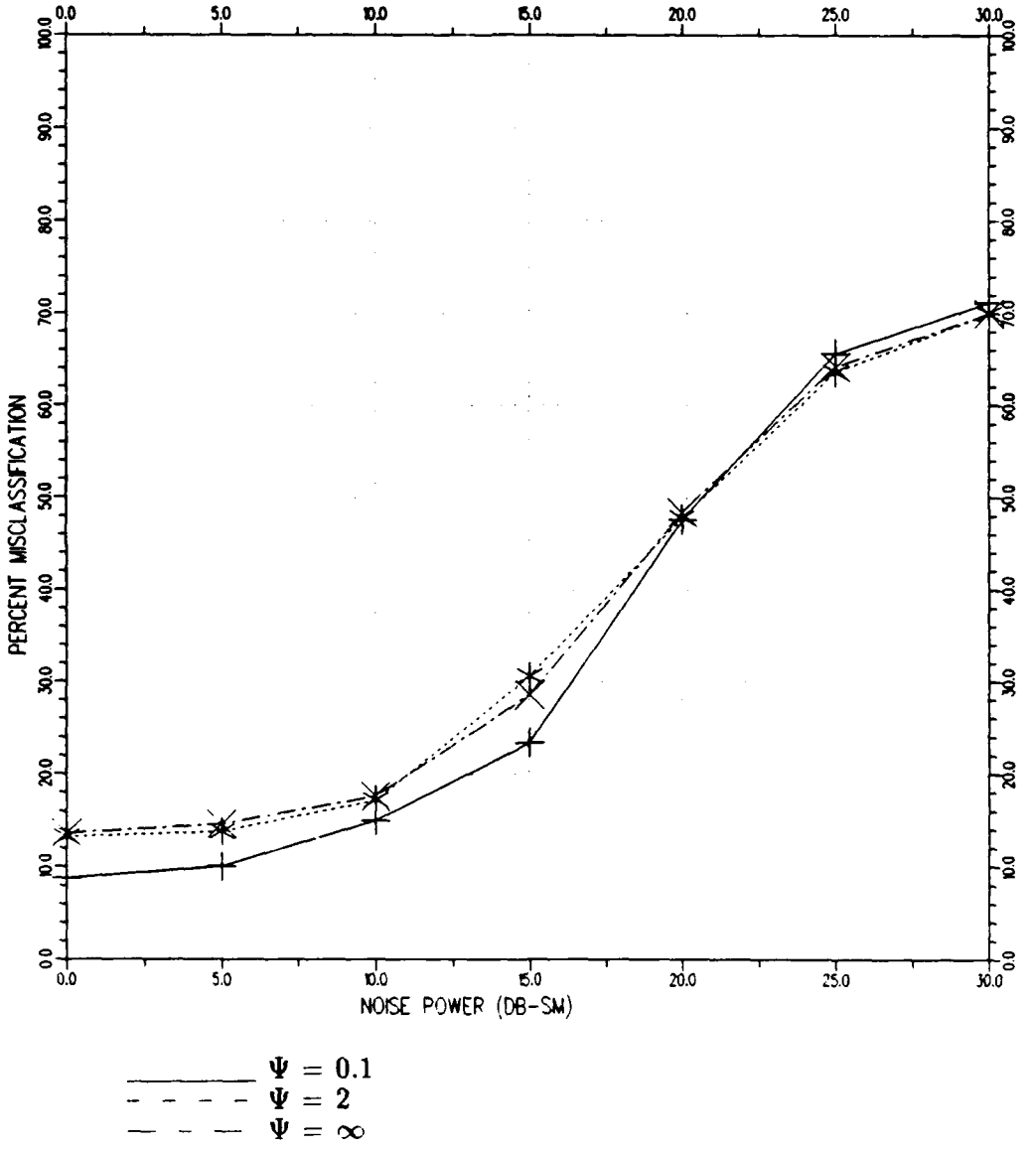

Figure 72: Correlation study for multiplicitive 4 MHz band faded channel.

7.4 Comparison of Faded Channels Performance

A final study was conducted to directly compare the performance of the three channels for different correlation coefficients, deterministic weights, frequency bands, and feature number combinations. Figures 73, 74, and 75 directly compare the three feature types using a 2 MHz band for different values of α. Although performance is relatively poor for both channels F1 and F2, channel F2 significantly outperforms channel F1 for $\alpha = 0.75$ and $\alpha = 0.5$ (Figures 74 and 75 respectively). Channel F1 significantly outperforms the other two for all values of α as shown.

A comparison of the three feature types for various values of Ψ is given in Figures 76, 77, and 78. Figures 76 and 77 demonstrate that for a small Ψ (highly correlated faded components), channel F3 may actually outperform channel F2. The figures also demonstrate the strong performance of channel F1 irregardless of the correlation between faded components.

Figures 79 and 80 compare the three faded channels for two different values of α. Both figures demonstrate the superiority of channel F3 over channel F2 in terms of classification performance. In fact, the performance of channel F3 approaches that of channel F1 for low noise power in Figure 80.

Figures 81, 82, and 83 demonstrate that the resulting performance from using channel F3 features may be significantly greater than using channel F2 features irregardless of the correlation of the faded components. These figures also reinforce the strong performance of channels utilizing phase information. It is important to note, however, that classification performance of a channel with an unknown multiplicitive component (channel F3) may approach the performance of a channel which maintains absolute amplitude as well as target phase information (channel F1). As the faded components become increasingly uncorrelated in Figures 81

and 83 respectively, the performance of channel F3 degrades, but still provides relatively good classification performance at low noise powers.

Direct comparison of the three faded channels in term of classification performance resulted in several interesting results. Most importantly, the superior performance of channel F1 indicates that phase information concerning the target is maintained even for relatively small deterministic weights ($\alpha = 0.5, 0.75$). Therefore, a system which can accurately estimate intrinsic target phase is still desired even if the propagation path is subject to a degree of multipath interference. Second, the study indicates that under certain frequency band, deterministic weight, and correlation conditions, the removal of the unknown multiplicitive component from the output of channel F3 provides a set of features whose classification performance rivals that of channel F1, and is better than the performance of channel F2. Frequency bands of 4 MHz, deterministic weights of 0.75, and highly correlated faded components tend to accentuate the normalized features compared to other conditions.

It is important to note that given a propagation path modeled by these conditions, which are far from *ideal* in the RTI sense, classification may be performed using only relative RCS values. Furthermore, having the ability to estimate absolute RCS would not provide an increase in performance. In fact, the use of the corrupted amplitude estimates without normalization would seriously degrade classification performance (Figure 81). In this case, even the ability to estimate target phase would only decrease the misclassification percentage by four or five percent at low noise power levels.

Overall, the study has indicated that if one is given a multipath propagated signal, there is little need of a calibrated reference to estimate absolute RCS. Rather, a stationary uncalibrated reference may be utilized to estimate relative

RCS of the target to be used for classification purposes.

Parameter Under Observation: Channel
Channel Model: Key
Azimuth angle: 45
Start Frequency: 8.0 MHz
Stop Frequency: 10.0 MHz
Number of Frequencies: 10
Deterministic Weight: 0.9
Correlation Coefficient: 0.5

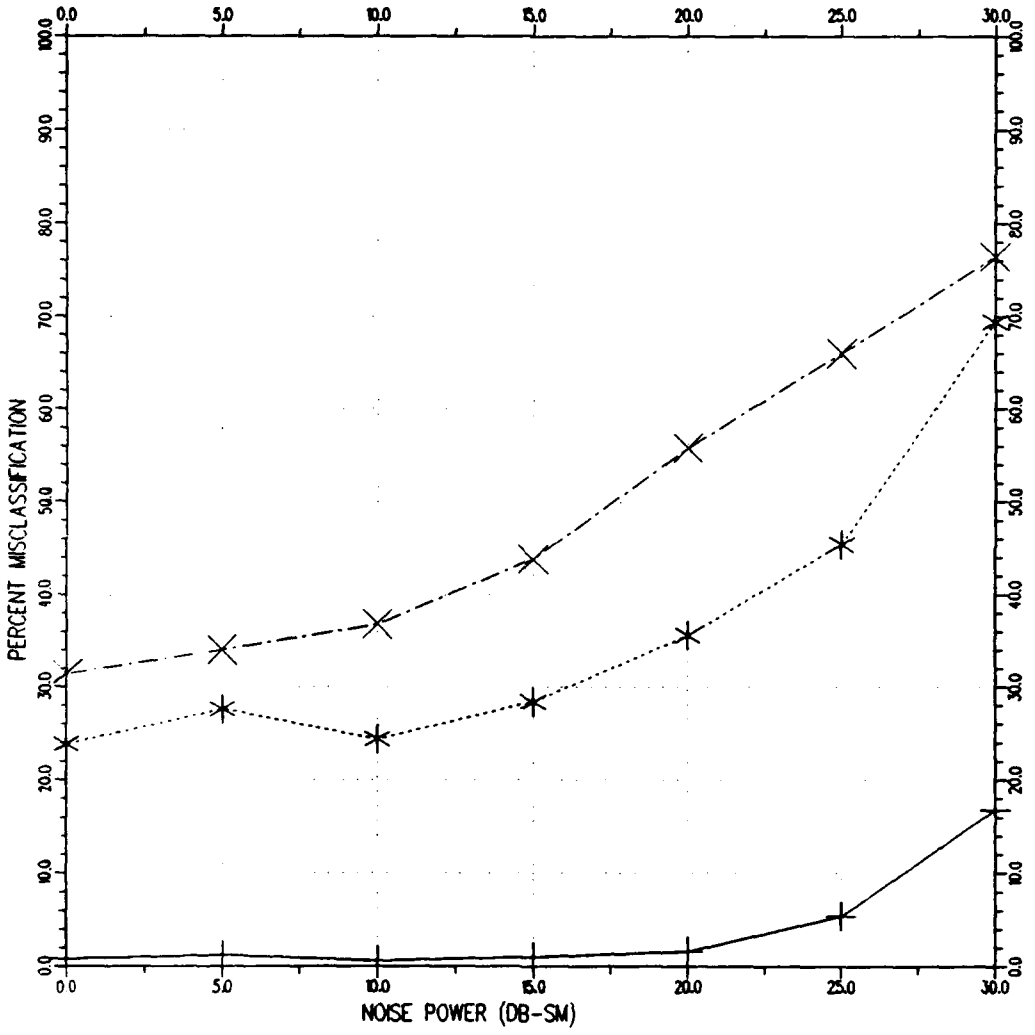

Coherent Faded Channel
Non-Coherent Faded Channel
Multiplicitive Component Faded Channel

Figure 73: Highly deterministic 2 MHz band channel study.

Parameter Under Observation: Channel
Channel Model: Key
Azimuth angle: 45
Start Frequency: 8.0 MHz
Stop Frequency: 10.0 MHz
Number of Frequencies: 10
Deterministic Weight: 0.75
Correlation Coefficient: 0.5

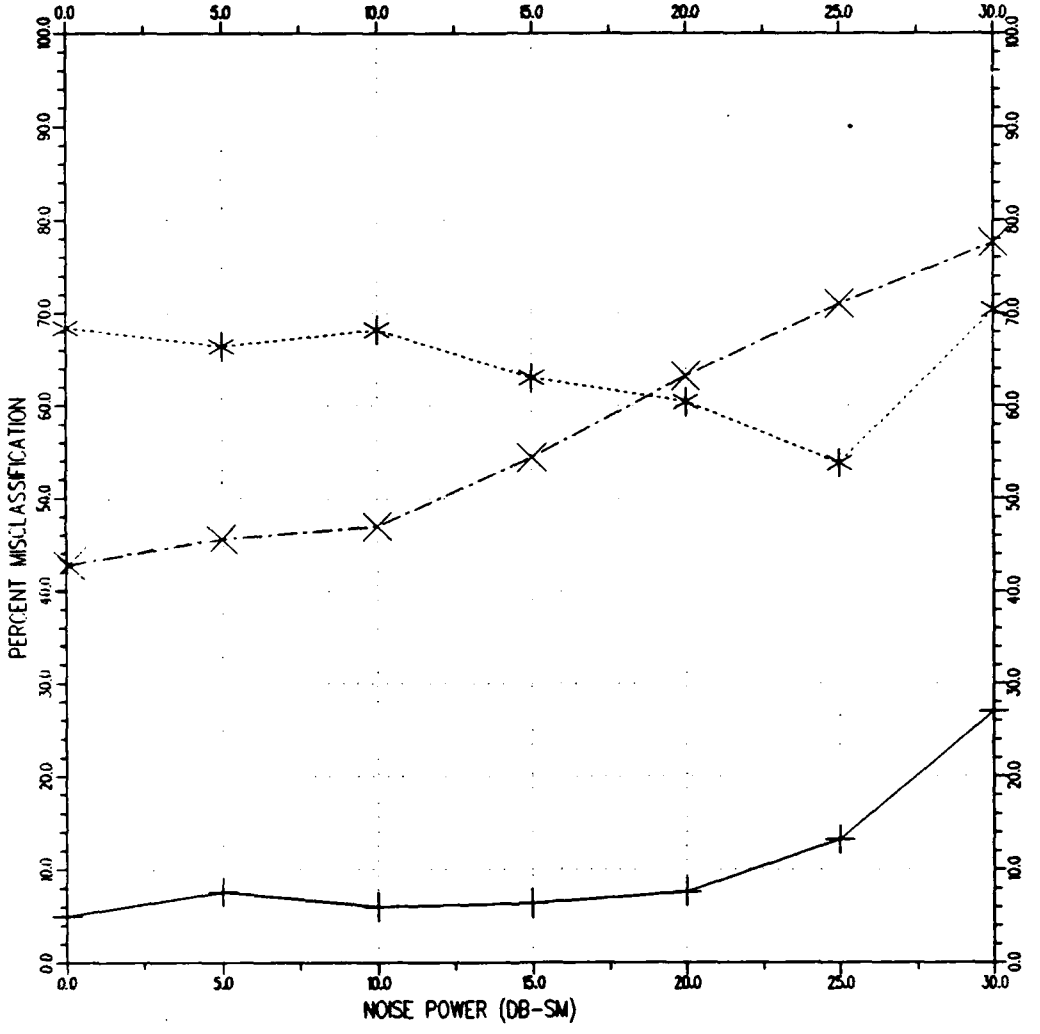

Figure 74: Partially faded 2 MHz band channel study.

Parameter Under Observation: Channel
Channel Model: Key
Azimuth angle: 45
Start Frequency: 8.0 MHz
Stop Frequency: 10.0 MHz
Number of Frequencies: 10
Deterministic Weight: 0.5
Correlation Coefficient: 0.5

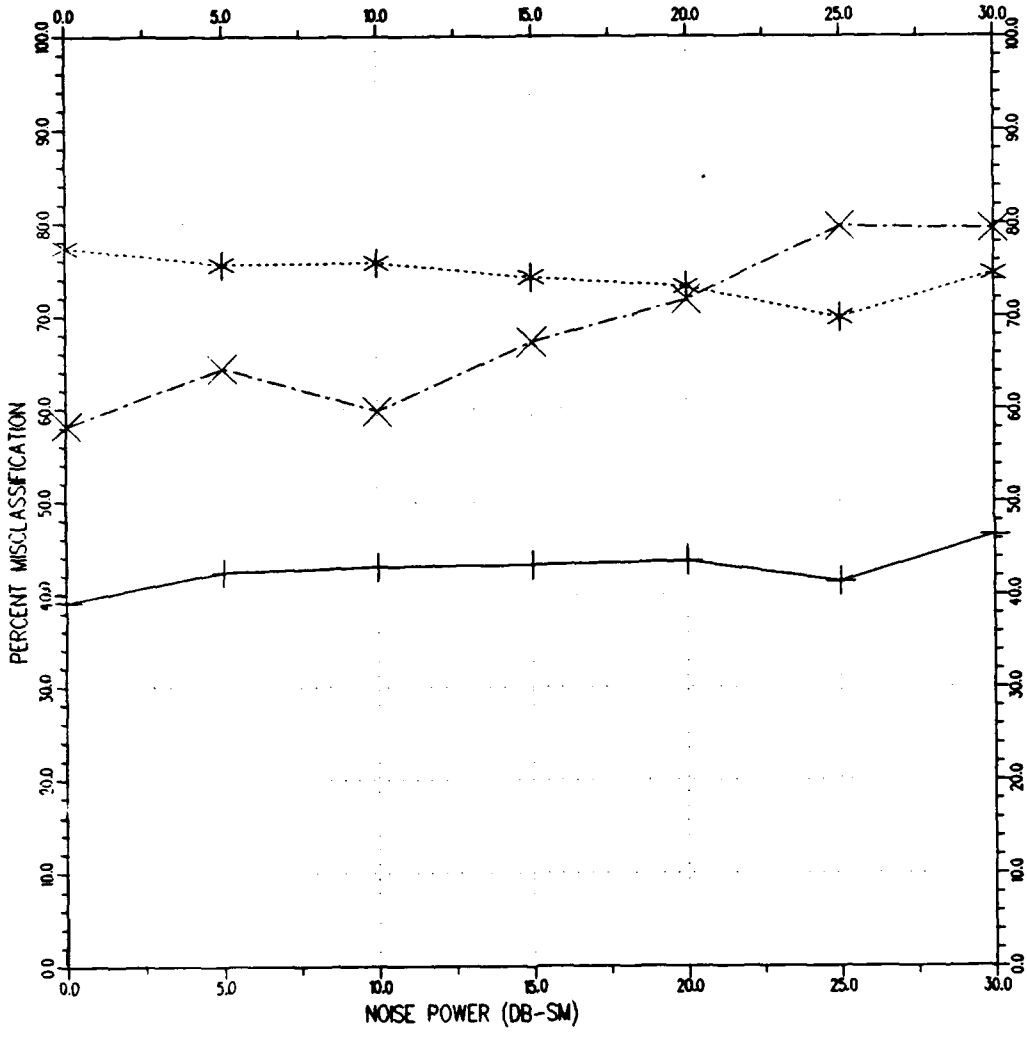

Coherent Faded Channel
Non-Coherent Faded Channel
Multiplicitive Component Faded Channel

Figure 75: Highly faded 2 MHz band channel study.

Parameter Under Observation: Channel
Channel Model: Key
Azimuth angle: 45
Start Frequency: 8.0 MHz
Stop Frequency: MHz
Number of Frequencies: 10
Deterministic Weight: 0.9
Correlation Coefficient: 0.001

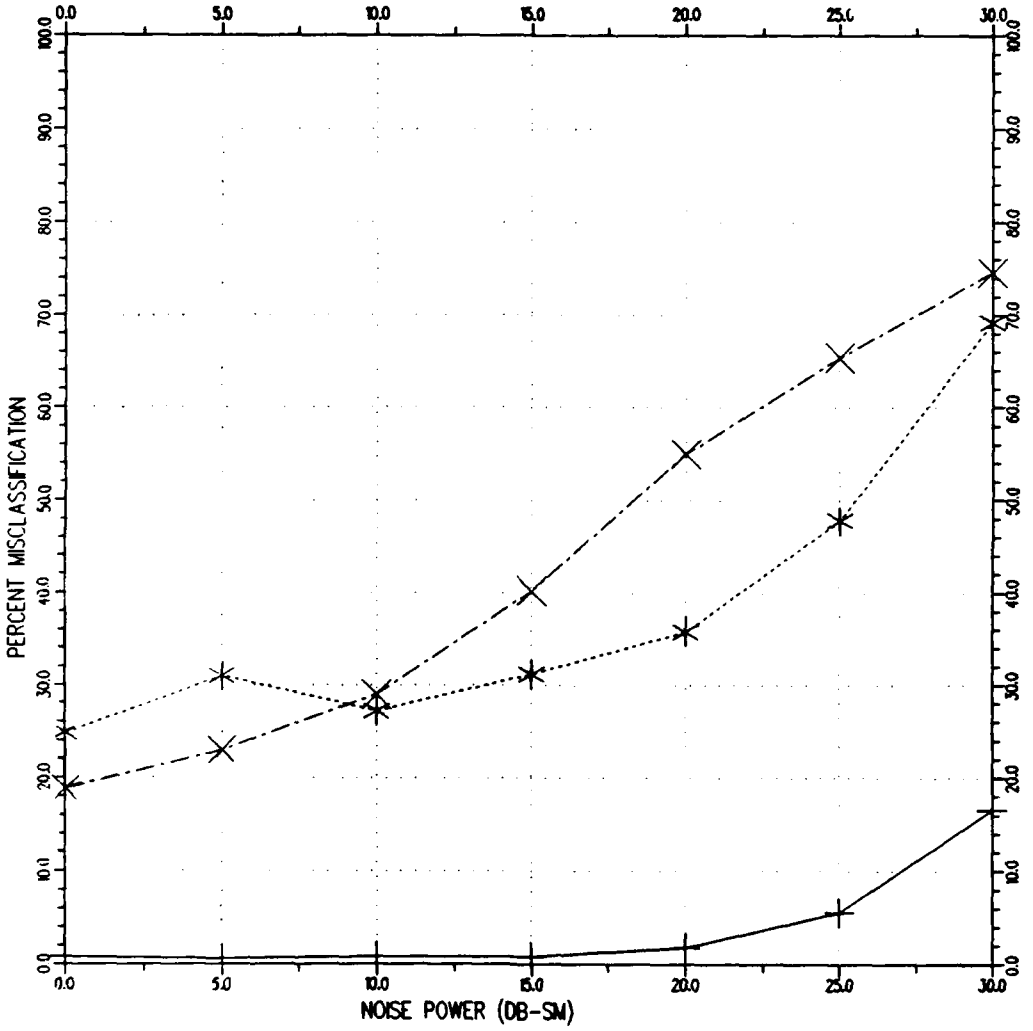

Coherent Faded Channel
Non-Coherent Faded Channel
Multiplicitive Component Faded Channel

Figure 76: Highly correlated 2 MHz band channel study.

Parameter Under Observation: Channel
Channel Model: Key
Azimuth angle: 45
Start Frequency: 8.0 MHz
Stop Frequency: 10.0 MHz
Number of Frequencies: 10
Deterministic Weight: 0.9
Correlation Coefficient: 0.05

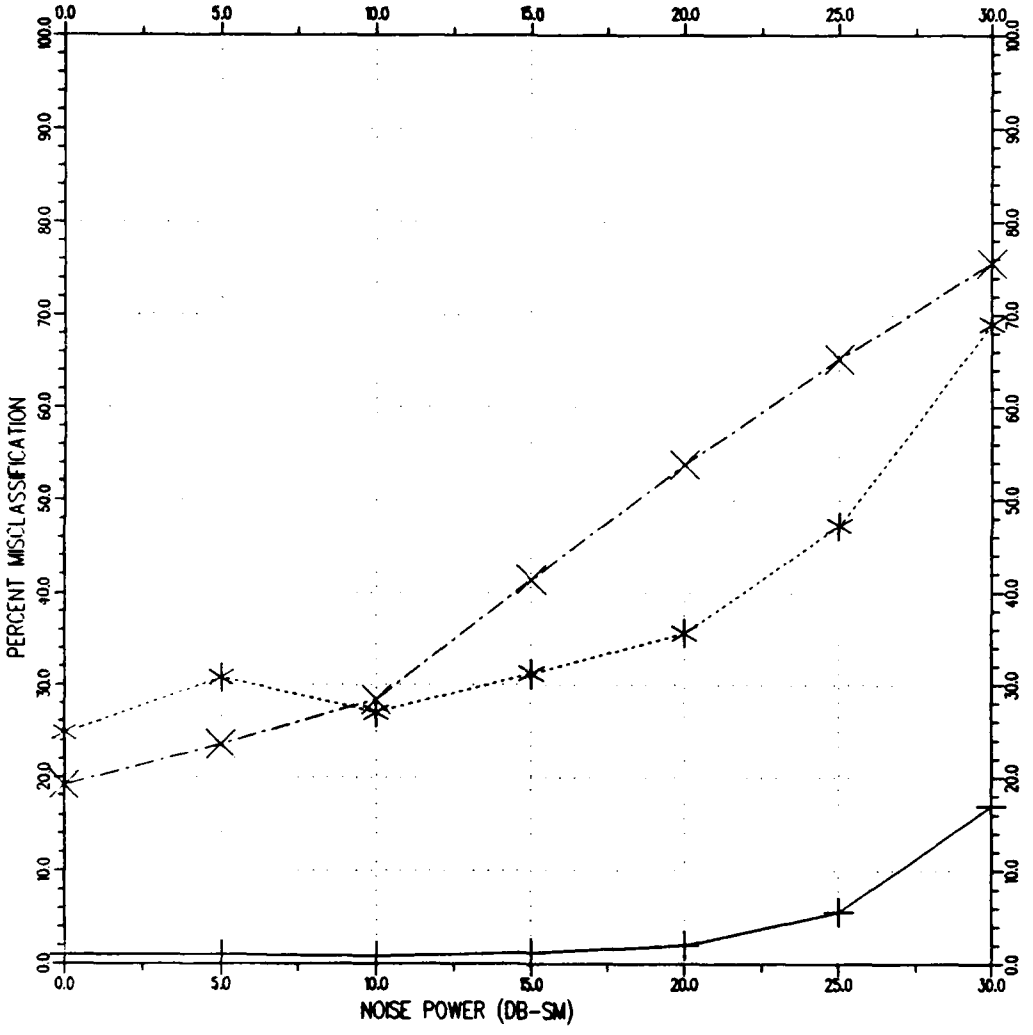

Figure 77: Correlated 2 MHz band channel study.

Parameter Under Observation: Channel
Channel Model: Key
Azimuth angle: 45
Start Frequency: 8.0 MHz
Stop Frequency: 10.0 MHz
Number of Frequencies: 10
Deterministic Weight: 0.9
Correlation Coefficient: ∞

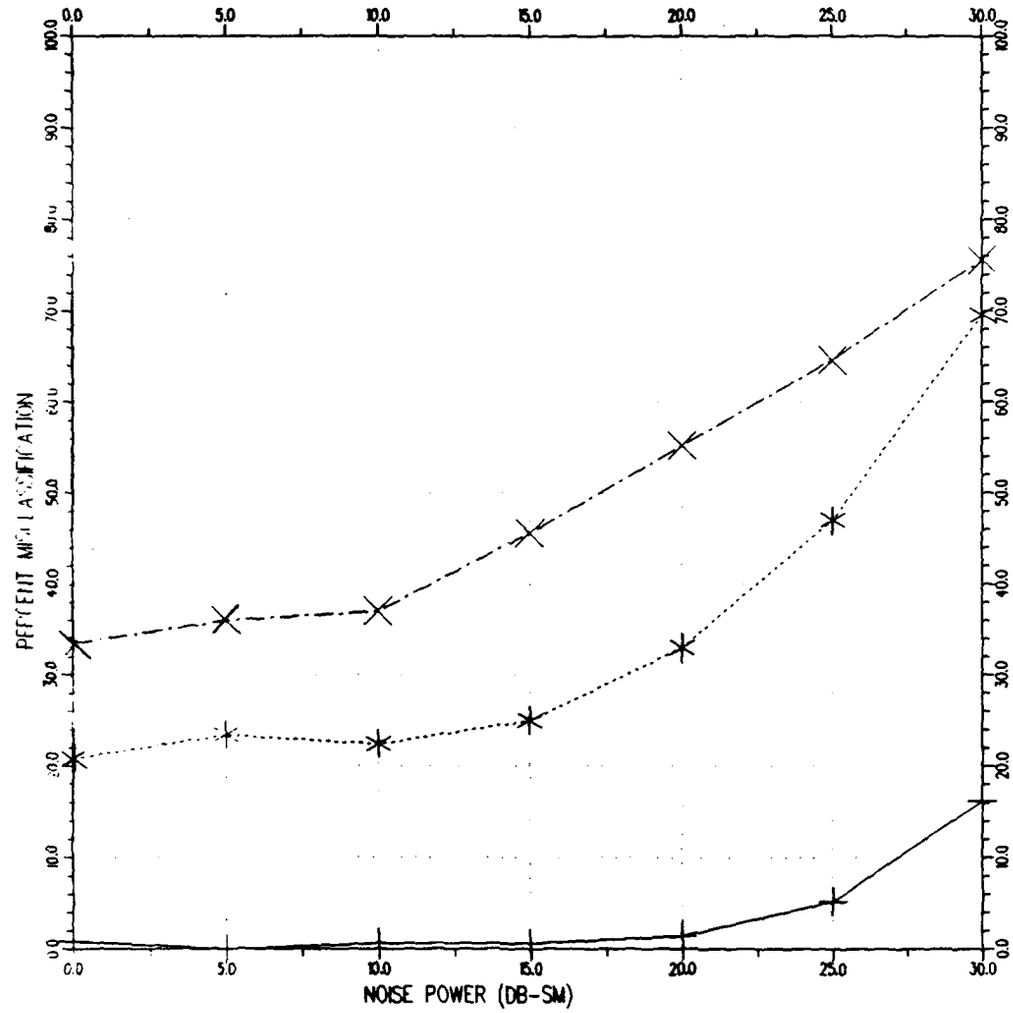

Coherent Faded Channel
Non-Coherent Faded Channel
Multiplicitive Component Faded Channel

Figure 78: Uncorrelated 2 MHz band channel study.

Parameter Under Observation: Channel
Channel Model: Key
Azimuth angle: 0
Start Frequency: 8.0 MHz
Stop Frequency: 12.0 MHz
Number of Frequencies: 10
Deterministic Weight: 0.75
Correlation Coefficient: 0.5

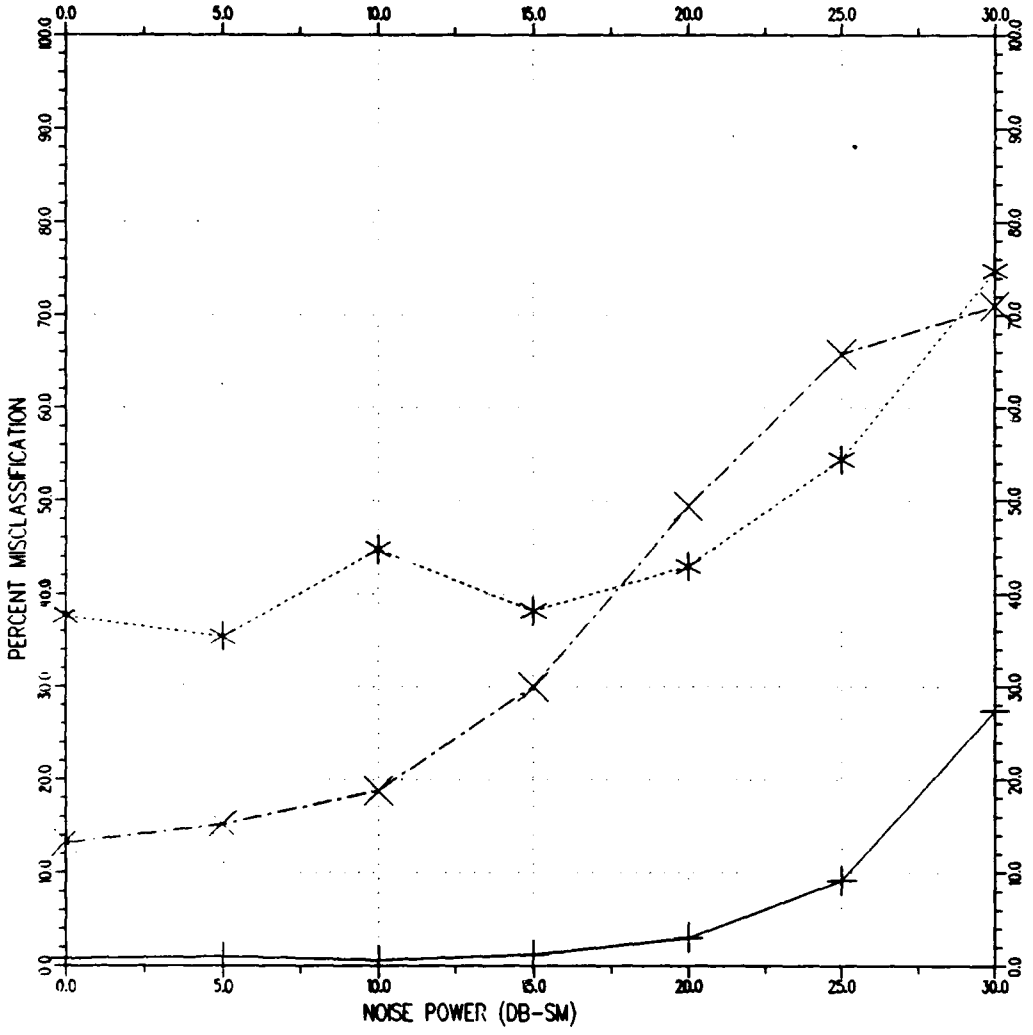

Figure 79: Partially faded 4 MHz band channel study.

Parameter Under Observation: Channel
Channel Model: Key
Azimuth angle: 0
Start Frequency: 8.0 MHz
Stop Frequency: 12.0 MHz
Number of Frequencies: 10
Deterministic Weight: 0.5
Correlation Coefficient: 0.5

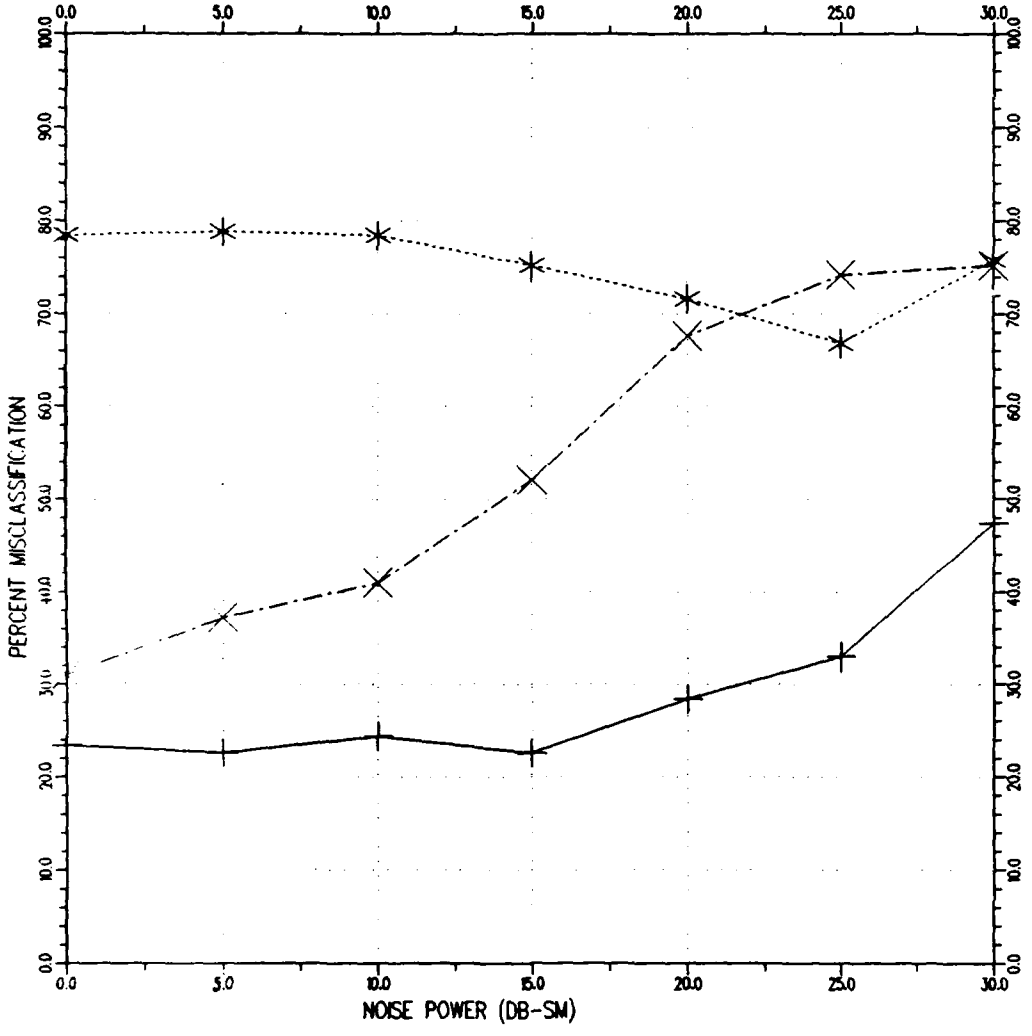

Figure 80: Highly faded 4 MHz band channel study.

Parameter Under Observation: Channel
Channel Model: Key
Azimuth angle: 0
Start Frequency: 8.0 MHz
Stop Frequency: 12.0 MHz
Number of Frequencies: 10
Deterministic Weight: 0.75
Correlation Coefficient: 0.1

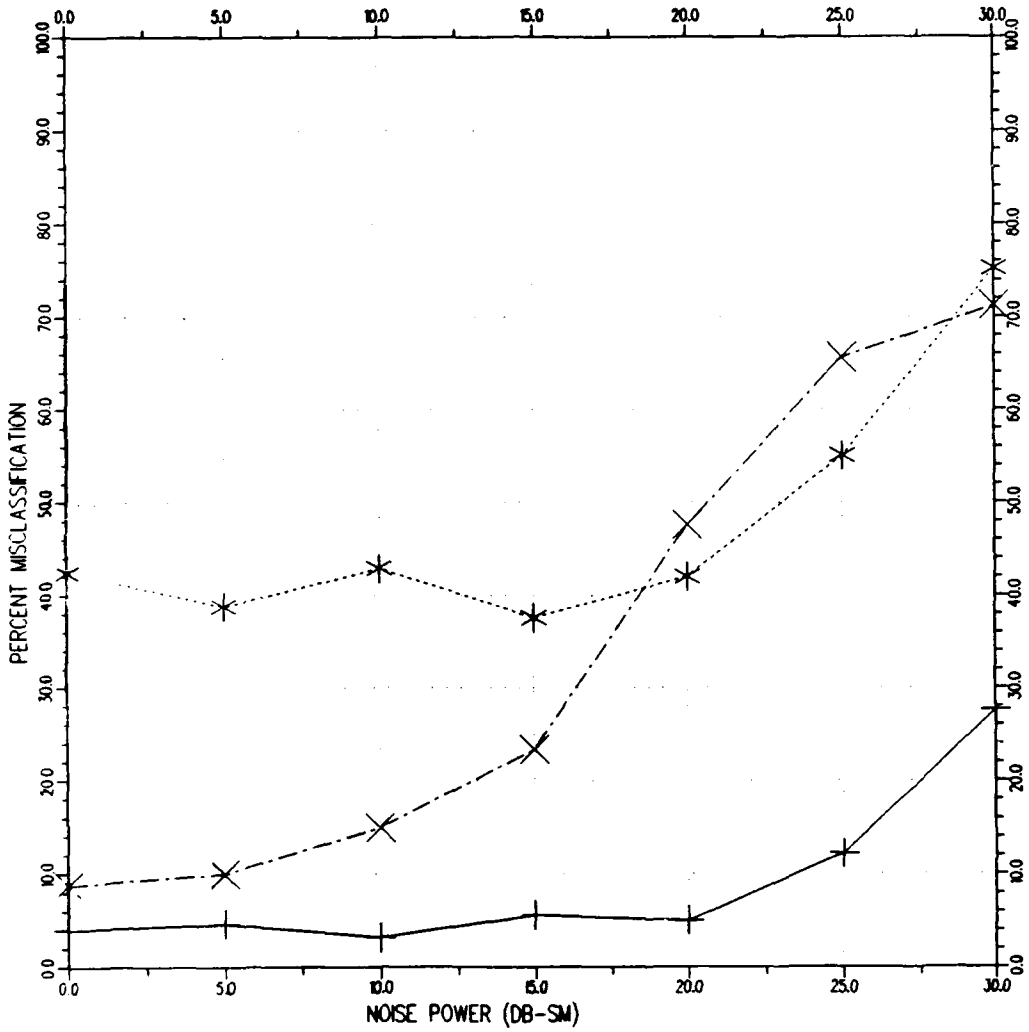

Figure 81: Correlated 4 MHz band channel study.

Parameter Under Observation: Channel
Channel Model: Key
Azimuth angle: 0
Start Frequency: 8.0 MHz
Stop Frequency: 12.0 MHz
Number of Frequencies: 10
Deterministic Weight: 0.75
Correlation Coefficient: 2

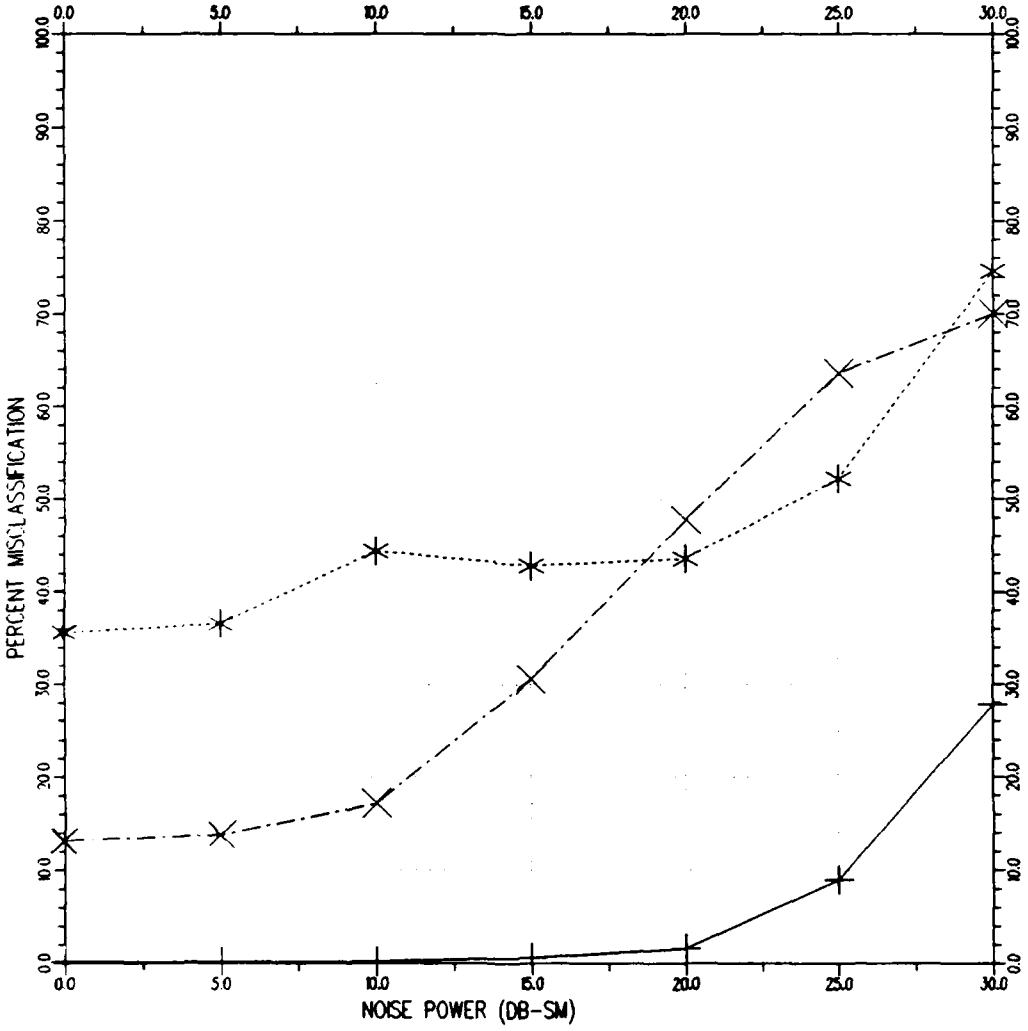

Figure 82: Slighly correlated 4 MHz band channel study.

Parameter Under Observation: Channel
Channel Model: Key
Azimuth angle: 0
Start Frequency: 8.0 MHz
Stop Frequency: 12.0 MHz
Number of Frequencies: 10
Deterministic Weight: 0.75
Correlation Coefficient: ∞

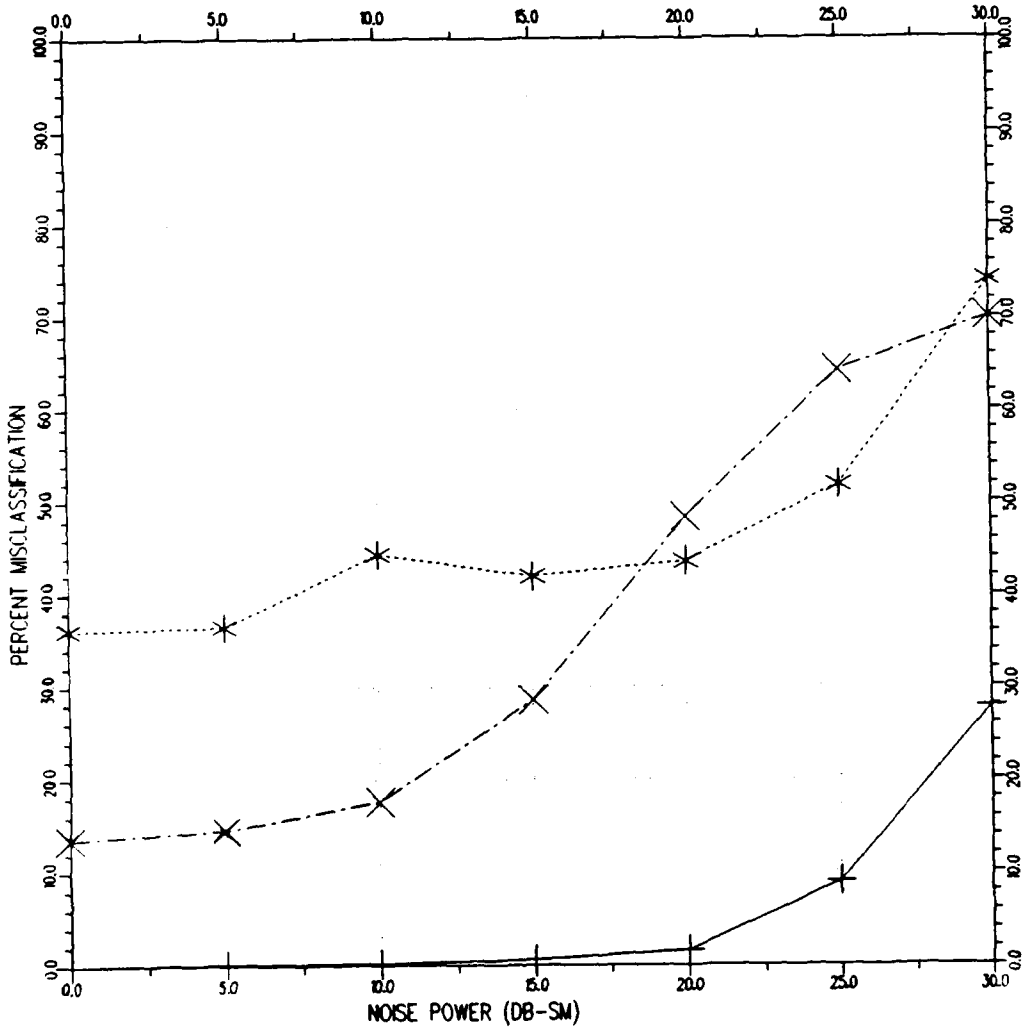

Figure 83: Uncorrelated 4 MHz band channel study.

CHAPTER VIII

CONCLUSIONS

A study of existing HF radar systems with respect to use as a measurement facility has been conducted. Examination of a HF skywave radar system has led to the incorporation of two classes of channel models, the Gaussian and fading channel models. Further variations of the channels within each class simulated the possible restrictions which the external environment and propagation path might place on the measurement system in terms of the estimation of various target features. As a result, relationship between the various channels and classification *performance in terms of various radar system parameters were found.*

The simulation studies have demonstrated that classification performance is largely dependent on the size of the frequency band for all channel models implemented. Moreover, the results have indicated that when the frequency band is extremely limited ($\leq$ 2 MHz), classification performance may be improved by increasing the number of frequencies at which target features are estimated. Therfore, if one is restricted to a small frequency band, performance may be increased at the cost of additional processing time.

The fading channel models simulated the effect of multipath propagation on the RTI system. Results indicated that without phase information, the estimation of absolute RCS feature may not lead to additional classification performance over the estimation of relative RCS features. Therfore, there would be no advantage in

having a calibrated reference which would allow the estimation of absolute RCS.

A variety of channels have been simulated. In order to further evaluate classification performance, data from existing HF radar systems is desired. Given a large set of Doppler spectral estimates containing familiar aircraft, several techniques may be investigated to estimate various features of the targets. A comparison of these estimates would provide insight into the statistical properties of real estimates. In addition, a comparison of these estimates with those simulated from the ElectroScience Laboratory data base would provide a measure of how accurately the backscatter coefficients measured on the compact range represent those measured in real HF radar system.

REFERENCES

[1] A.A. Ksienski, Y.T. Lin, and L.J. White, "Low Frequency Approach to Target Identification," *Proceedings of the IEEE*, Vol. 63, pp. 1651–1660, December 1975.

[2] A.J. Kamis, "Radar Target Identification Techniques Applied to a Polarization Diverse Aircraft Data Base," M.S. Thesis, The Ohio State University, ElectroScience Laboratory, Autumn 1986.

[3] E.K. Walton and J.D. Young, "The Ohio State University Compact Radar Cross-section Measurement Range," *IEEE Trans. on Antennas and Propagation*, Vol. AP-32, No. 11, pp. 1218–1223, November 1985.

[4] J.S. Chen, "Automatic Target Classification Using HF Multifrequency Radars," Ph.D. Dissertation, The Ohio State University ElectroScience Laboratory, Columbus, Ohio, 1983.

[5] D.E. Barrick, "Accuracy of Parameter Extraction from Sample-Averaged Sea-Echo Doppler Spectra," *IEEE Trans. on Antennas and Propagation*, Vol. AP-28, No. 1, January 1980.

[6] K.A. Norton, "The Calculation of Ground-Wave Field Intensity Over a Finitely Conducting Spherical Earth," *Proceedings of the I.R.E.*, pp. 623–639, December 1941.

[7] H.N. Mullaney and F. Cullen, "Project TOPSEA Technical Discussion," Rome Air-Development Center TR-76-233, Vol. 1, Griffiss AFB, NY, July 1976.

[8] N.F. Chamberlain, "Surface Ship Classification Using Multipolarization, Multifrequency Sky-Wave Resonance Radar," Technical Report 714190-9, The Ohio State University ElectroScience Laboratory, Columbus, Ohio, 1984.

[9] A.V. Oppenheim and R.W. Schafer, *Digital Signal Processing*, Prentice-Hall, 1975.

[10] M.H. DeGroot, *Probability and Statistics*, Addison-Wesley, 1975.

[11] M.I. Skolnik, *Introduction to Radar Systems*, McGraw-Hill, New York, 1980.

[12] J.M. Headrick and M.I. Skolnik, "Over-the-Horizon-Radar in the HF Band," *Proceedings of the IEEE*, Vol. 62, pp. 664-673, No. 6, June 1974.

[13] D.E. Barrick and J.B. Snider, "The Statistics of H.F. Sea-Echo Doppler Spectra, *IEEE Trans. on Antennas and Propagation*, Vol. AP-25, January 1977.

[14] K. Davies, "Ionospheric Radio Propagation," National Bureau of Standards Monograph 80, Washington, D.C., 1965.

[15] D.B. Trizna, "Estimation of the Sea Surface Radar Cross Section at HF from Second-Order Doppler Spectrum Characterstics," Naval Research Laboratory, Report 8579, May 1982.

[16] W.B. Goggins, P. Blacksmith, and G.J. Sletten, "Phase Signature Radars," *IEEE Trans. on Antennas and Propagation*, Vol. AP-22, No. 6, November 1974.

[17] D.F. Kimball, "Enhanced Techniques For Broadband Radar Backscatter Measurement," Technical Report 714190-4, The Ohio State University ElectroScience Laboratory, Columbus, Ohio, December 1983.

[18] A. Kamis, F. Garber, and E. Walton, "Radar Target Identification Studies–Software Development and Documentation," Technical Report 716559-1, The Ohio State University ElectroScience Laboratory, Columbus, Ohio, September 1985.

[19] C.E. Shannon, "Communication in the Presence of Noise," *Proceedings IRE*, Vol. 37, No. 1, pp. 10–21, January 1949.

[20] J.W. Maresca, Jr., and J.R. Barnum, "Theoretical Limitation of the Sea on the Detection of Low Doppler Targets by Over-the-Horizon Radar," *IEEE Trans. on Antennas and Propagation*, Vol. AP-30, No. 5, September, 1982.

[21] T.M. Georges, J.W. Maresca, Jr., J.P. Riley, and C.T. Carlson, "Real-Time Sea-State Surveilance with Skywave Radar," *IEEE Journal of Oceanic Engineering*, Vol. OE-8, No. 2, April 1983.

[22] T.M. Georges and J.W. Maresca, Jr., "The Effects of Space and Time Resolution on the Quality of Sea-Echo Doppler Spectra Measured with HF Sky-Wave Radar," *Radio Science*, Vol. 14, No.3, pp. 455–469, May–June 1979.

[23] T.M. Georges, "Progress Toward a Practical Skywave Sea-State Radar," *IEEE Trans. on Antennas and Propagation*, Vol. AP-28, No. 6, November 1980.

[24] R.O. Pilon and J.M. Headrick, "Estimating the Scattering Coefficient of the Ocean Surface for High-Frequency Over-the-Horizon Radar," NRL Memorandum report 5741, Radar Techniques Branch Radar Division, March 28, 1986.

[25] G.F. Earl, and B.D. Ward, "The Frequency Management System of the Jindalee Over-the-Horizon Backscatter HF Radar," *Radio Science*, Vol. 22, No. 2, pp. 275–291, March–April 1987.

[26] F.J. Harris, "On the Use of Windows for Harmonic Analysis with the Discrete Fourier Transforms," *Proceedings of the IEEE*, vol. 66, pp51–81, January 1978.

[27] H.L. Van Trees, *Detection, Estimation, and Modulation Theory, Part I*, John Wiley & Sons, New York, 1968.